Laser frequency standards based on gas-filled hollow-core fibres

Triches, Marco

Publication date:
2016

Document Version
Publisher's PDF, also known as Version of record

DFM
Danish National Metrology Institute

Laser Frequency Standards based on Gas-Filled Hollow-Core Fibers

A dissertation presented
by
Marco Triches
to
The Department of Photonics Engineering
and
Danish Fundamental Metrology

in partial fulfillment of the requirements
for the degree of
Doctor of Philosophy
in the subject of
Electronics, Communication and Space Science

Technical University of Denmark
Kogens Lyngby, Denmark
June 2016

Danish Fundamental Metrology
Matematiktorvet, 307
2800 Kongens Lyngby, Denmark
Phone +45 4593 1144
info@dfm.dk
www.dfm.dk

Technical University of Denmark
Department of Photonics Engineering
Ørsteds Plads, building 343
2800 Kongens Lyngby, Denmark
Phone +45 4525 6352
info@fotonik.dtu.dk
www.fotonik.dtu.dk

This thesis is dedicated to my "extended" family: my mother, Mirella, for the hard time she had since I left Italy, my father, Danilo, for the unaware training I received along my childhood building unlikely things. To my little brother Andrea and my little aunt Sandra, for the unconditional support. Finally, to my beloved Corinna, for enduring hardship of the worst sort by picking me among the others.

Contents

Abstract

The work presented in this thesis has been developed within the Marie-Curie Initial Training Network (ITN) called *Quantum Sensor Technologies and Applications* (QTea), funded under the EU-FP7 program (contract-N MCITN-317485). The ITN QTea project is aimed at preparing a cohort of early-stage researchers for the emerging challenges in quantum technology. The scientific scope of the network is focused on the physics of modern quantum sensors for gravitational probing, rotation sensing, field probes, magnetic surface microscopy, atomic clocks and precision spectroscopy. This work naturally falls within precision spectroscopy with the scope of developing a fiber-based, portable optical frequency standard in the telecommunication band.

Nowadays, portable optical frequency standards are important not only in metrology and telecommunication industry but also for remote sensing applications. Since the advent of frequency combs, an optical frequency reference may be used to stabilize the comb in order to achieve an optical clock, which has better specifications than standard Rb and Cs atomic clocks. The realization of such an optical frequency reference is based on the laser frequency stabilization technology, which has been widely investigated in the past decades, using many different molecular and atomic transitions as optical reference. One of the recommended references in the telecommunication region of the light spectrum is given by a specific absorption line in $^{13}C_2H_2$ acetylene. However, many other molecular references (e.g. methane and carbon dioxide) may be interesting for remote sensing applications in the near infrared region. Typically, molecules are weakly absorbing in the telecommunication band and, hence, they require a long interaction length to be detected. For these reasons, since the advent of the photonic crystal fiber technology, many studies have been performed using various hollow-core fibers used as vapor cells. This hollow-core fiber approach is also meeting the needs of the remote sensing applications, which require size and weight reductions with respect to the conventional optical frequency reference systems based on bulky glass vapor cell and free space optics. All in all, this technology shows great potential but novel solutions in the fiber sealing/encapsulation needs to be developed in order to encounter the market demands. For example, another application

looking into the HC fiber technology is represented by high-energy pulse delivery systems. The low non-linearity of the in-air guidance mechanism offers a unique tool to propagate unperturbed pulses far from the laser source. A tight vacuum sealed encapsulation can avoid the remaining non-linearity generated by in-air Raman scattering, eliminating the remaining obstacle for the implementation of the technology in the laser machining industry.

This thesis presents the development of a compact fiber-based optical frequency standard using acetylene-filled hollow-core fibers. The study focuses both on the technical realization of a portable system and on the theoretical identification of the most important parameters for in-fiber gas spectroscopy applications. The scope of the project is to reduce the gap that prevents the state of the art technology from being commercialized. This thesis aims at: (a) characterizing of different fibers design; (b) testing the performance of the different fibers; (c) proposing a theoretical explanation for the interaction mechanism inside the gas-filled hollow-core fibers; (d) developing a dedicated solution for the fiber encapsulation; (e) characterizing the instability and reproducibility of the realized optical frequency standard prototype. Furthermore, the research in various encapsulation techniques for the hollow-core fiber ends in a collaboration with other research groups for (f) the development of a proof-of-concept in-fiber Raman sensor for aqueous solutions.

Resumé på dansk

Arbejdet præsenteret i denne afhandling er blevet udviklet inden for Marie-Curie Initial Training Network (ITN) *Quantum Sensor Technologies and Applications* (QTea), som finansieres under EU-FP7-programmet (kontrakt-N MCITN-317.485). QTea projektets formål er at forberede nyuddannede forskere til nye udfordringer inden for kvanteteknologi. Netværkets videnskabeligt formål er fokuseret påfysikken bag moderne kvantesensorer til gravitationel sondering, rotationsmåling, felt prober, magnetisk overflademikroskopi, atomure og præcisionsspektroskopi. Arbejdet i denne afhandling falder naturligt inden for præcisionsspektroskopi, hvor målet er at udvikle en fiberbaseret, transportabel optisk frekvensnormal i telekommunikationsbåndet.

Bærbare optiske frekvensnormaler er i dag vigtige ikke blot for metrologi og i telekommunikationsindustrien, men ogsåtil anvendelser inden for *remote sensing*. Med indførelsen af frekvenskamme kan en optisk frekvensreference ogsåanvendes til at stabilisere kammen og herved realisere et optisk ur, som har bedre specifikationer end standard Rb og Cs atomure. Fremstillingen af en sådan optisk frekvensreference er baseret påfrekvensstabiliseringsteknologi, som er blevet bredt undersøgt i de seneste årtier ved brug af mange forskellige molekylære og atomare overgange som optisk reference. I telekommunikationsområdet af lysspektret er en af de anbefalede referencer givet ved en specifik absorptionslinje i $^{13}C_2H_2$ acetylen. Mange andre molekylære referencer (for eksempel linjer i metan og kuldioxid) kunne blive interessante for *remote sensing* applikationer i det nærinfrarøde område. Typisk er molekyler svagt absorberende i telekommunikationsområdet og dermed kræver de en lang interaktionslængde for at blive detekteret. Siden fremkomsten af fotonisk krystalfibre er der derfor udført mange undersøgelser, hvor hulkernefibre er anvendt som gasceller. Metoden med hulkernefibre imødekommer ogsåbehovene i de *remote sensing* anvendelser, hvor der kræves reduktion i størrelse og vægt i forhold til de konventionelle optiske frekvensreferencer baseret påpladskrævende *bulk* glasceller og *free space* optik. Alt i alt viser teknologien stort potentiale, men nye løsninger i fiber forsegling / indkapsling skal udvikles for at imødekomme påmarkedskrav. Som eksempel pået andet område, hvor der ses påanvendelsen af hulkernefibre, er systemer til høj-energi

lyspulser. Den lave ulinearitet i luften i hulkernefiberens kerne bidrager til en unik metode for uforstyrret udbredelse af pulser langt fra laserkilden. En tæt vakuumforseglet indkapsling kan fjerne den tilbageværende ulinearitet i luft forårsaget af Raman spredning, hvilket eliminerer den resterende hindring for indførelse af denne teknologi i laserbearbejdning.

Denne afhandling beskriver udviklingen af en kompakt fiberbaseret optisk frekvensnormal ved hjælp acetylen-fyldte hulkernefibre. Undersøgelsen fokuserer både påden tekniske fremstilling af et transportabelt system samt påden teoretiske identifikation af de vigtigste parametre for fiberbaserede applikationer inden for gasspektroskopi. Projektets formål er at mindske det gab, som forhindrer state-of-the-art teknologien i at blive kommercialiseret. Afhandlingen sigter mod at: (a) karakterisere forskellige fiberdesign; (b) afprøve egenskaberne af de forskellige fibre; (c) foreslåen teoretisk forklaring påvekselvirkningsmekanismen inde i gasfyldte hulkernefibre; (d) at udvikle en dedikeret løsning til fiberindkapsling; (e) karakterisere ustabilitet og reproducerbarhed for den realiserede prototype påen optisk frekvensnormal. Desuden afsluttes forskningen i forskellige fiberindkapslingsteknikker med et samarbejde med andre forskergrupper om (f) udvikling af en proof-of-concept Raman sensor til vandige løsninger baseret påhulkernefibre.

Thesis advisor: Prof. Ole Bang Marco Triches

Preface

This thesis is presented as partial requirement for obtaining a Ph.D. degree from the Technical University of Denmark (DTU). The research was financed by the EU Commission within the framework of the FP7 project 'QTea', Marie-Curie Initial Training Network (contract-N MCITN-317485). The research was carried out at the Danish Fundamental Metrology (DFM A/S) and at the Department of Photonics Engineering (DTU Fotonik), in the period from February 2013 to January 2016. The Ph.D project was supervised by Professor Ole Bang, leader of the Fiber Sensor and Supercontinuum group, and co-supervised Ph.D. Jan Hald, group leader of the Nano team at the Danish Fundamental Metrology, and by Associate Professor Jesper Lægsgaard (Fiber Optics, Devices and Non-linear Effects group).

Kgs. Lyngby
29th June 2016
Marco Triches

DFM
Danish National Metrology Institute

DTU Fotonik
Department of Photonics Engineering

Thesis advisor: Prof. Ole Bang Marco Triches

List of Acronyms

Here is reported a list of the major acronyms used in this thesis, in order of appearance.

BIPM Bureau International des Poids et Mesures, *page 2*

SAS Saturated Absorption Spectroscopy, *page 4*

HC Hollow-Core, *page 4*

HC-PCF Hollow-Core Photonic Crystal Fiber, *page 5*

SM Single Mode, *page 5*

HOM High Order Mode, *page 9*

AFM Atomic Force Microscope, *page 11*

ARF Anti-Resonant Fiber, *page 12*

MFD Mode Field Diameter, *page 13*

MM Multi Mode, *page 14*

FM Fundamental Mode, *page 14*

PM Polarization Maintaining, *page 17*

WFT Windowed Fourier Transform, *page 20*

SEM Scanning Electron Microscopy, *page 20*

FWHM Full Width Half Maximum, or linewidth, *page 26*

PID ProportionalIntegralDerivative controller, *page 29*

EOM Electro-Optic Modulator, *page 30*

RF Radio Frequency, *page 30*

SNR Signal-to-Noise Ratio, *page 31*

RMS Root Mean Square, *page 31*

PSD Power Spectral Density, *page 32*

AOM Acousto-Optics Modulator, *page 38*

List of Publications and Submitted Manuscripts

This thesis is based on the following collection of papers and manuscripts. The papers are appended at the end of the thesis in **Appendix I**.

Paper I **Optical frequency standard using acetylene-filled hollow-core photonic crystal fibers**
M. Triches, M. Michieletto, J. Hald, J. K. Lyngsø, J. Lægsgaard and O. Bang.
Optics Express, Vol. 23, Issue 9, pp. 11227-11241 (2015)

Paper II **Interference Cancellation for Hollow-Core Fiber Reference Cells**
J. Seppä, M. Merimaa, A. Manninen, M. Triches, J. Hald and A. Lassila.
IEEE TRANSACTIONS ON INSTRUMENTATION AND MEASUREMENT, Vol. 64, No. 6, June 2015

Paper III **Portable optical frequency standard based on sealed gasfilled hollowcore fiber using a novel encapsulation technique**
M. Triches, A. Brusch and J. Hald.
Applied Physics B, Vol. 121, No. 3, December 2015

Paper IV **Compact, CO_2-stabilized tuneable laser at 2.05 microns**
P. G. Westergaard, J. W. Thomsen, M. R. Henriksen, M. Michieletto, M. Triches, J. K. Lyngsøand J. Hald.
Optics Express, Vol. 24, Issue 5, pp. 4872-4880 (2016)

Paper V **Fiber-Based, Injection-Molded Optofluidic Systems: Improvements in Assembly and Applications**
M. Matteucci, M. Triches, G. Nava, A. Kristensen, M. R. Pollard, K. Berg-Sørensen and R. J. Taboryski.
Micromachines, Vol. 6, Special Issue: *Optofluidics 2015*, pp. 1971-1983, December 2015

My Contribution to the Publications

Paper I I planned and performed the experiments. I reproduced some preliminary experiments performed before the starting of my Ph.D. and planned the new sequence of experiments. Except for the simulations about the optical properties of the fibers, which have been provided by Mattia Michieletto (NKT Photonics), I experimentally characterized the fibers and evaluate their performance. I proposed a simple theoretical approach which aimed to explain the interaction mechanism in presence of high order modes in the fiber, analyzed the data and wrote the paper.

Paper II I fabricated and assembled the acetylene-filled fiber-based optical frequency standard in a stand-alone packaging. I characterized the system and delivered to VTT Laboratories in Helsinki (Finland) for a comparative measurement. I contributed to the paper, providing details of the system characterization done at DFM.

Paper III I developed and tested the novel fiber encapsulation technique, starting from a preliminary prototype previously developed at DFM. I tested the optical, mechanical and vacuum properties of the assembled system and characterized the performance. I evaluate the results and developed dedicated tools to fabricate the stand-alone optical frequency standard based on this technology. I planned and performed the experiments, developing dedicated programming routines for the data acquisition. I analyzed the data and wrote the paper.

Paper IV I developed and fabricated the fiber encapsulation and I did the sealing of the device, giving my contribution also to the paper.

Paper V I proposed to use the polymer platform (originally developed for optical stretching of blood cell) to perform an in-fiber Raman spectroscopy experiment. I assembled the platform in collaboration with Marco Matteucci (DTU Nanotech). I characterized the optical properties of the system, planned and performed the Raman experiments and analyzed the data in collaboration with Mark R. Pollard (DFM). I contributed to write the paper.

List of Conference Contributions

The work described in this thesis was presented in different national/international conferences during the Ph.D. study. The presenting author is underlined.

1. **Optical frequency stabilization using gas filled hollow-core photonic crystal fibers**
   M. Triches, J. Hald, J. K. Lyngsø, J. Lægsgaard and O. Bang.
   SPIE Photonics Europe, Brussels, Belgium, 14^{th}-17^{th} April 2014
   Contribution: ORAL-INVITED

2. **An optimized hollow-core fiber-based laser spectrometer operating at 2.05 μm**
   A. Nwaboh, P.G. Westergaard, M. Triches, J. Hald, M. Michieletto, J. K. Lyngsø, O. Werhanhn, V. Ebert and J. C. Petersen
   FLAIR 2014, Florence, Italy, 5^{th}-9^{th} May 2014
   Contribution: POSTER

3. **Optical frequency stabilization using gas filled hollow-core photonic crystal fibers**
   P.G. Westergaard, M. Triches, M. Michieletto, J. K. Lyngsø, A. Brusch and J. Hald
   Atomic Clock for Industry, Neuchatel, Switzerland, 23^{rd}-26^{th} June 2014
   Contribution: POSTER

4. **Progress towards a fiber-based frequency reference in atmospheric CO_2 measurements**
   P.G. Westergaard, M. Triches, M. Michieletto, J. K. Lyngsø, J. W. Thomsen and J. Hald
   EFTF 2014, Neuchatel, Switzerland, 23rd-26th June 2014
   Contribution: POSTER

5. **Hollow-core fiber-based optical frequency standard**
   M. Triches, M. Michieletto, J. Hald, J. K. Lyngsø, J. Lægsgaard and O. Bang.
   DOPS 2014, Roskilde, Denmark, 12th-14th November 2014
   Contribution: POSTER

6. **Fiber-based portable optical frequency standard for telecommunication**
   M. Triches, A. Brusch, J. Hald,J. Lægsgaard and O. Bang.
   CLEO: Science and Innovations 2015
   San José, California, USA, 10th-15th May 2015
   Contribution: ORAL

7. **High order modes influence in laser frequency stabilization using gas-filled hollow-core fibers**
   M. Triches, J. Hald, M. Michieletto, J. K. Lyngsø, J. Lægsgaard and O. Bang.
   The European Conference on Lasers and Electro-Optics 2015
   Munich, Germany 21st-25th June 2015
   Contribution: ORAL

8. **Fiber-based portable optical frequency standard for telecommunication**
   M. Triches, J. Hald, A. Brusch, J. K. Lyngsø, J. Lægsgaard and O. Bang.
   QTeaPS: Quantum Technology sensor and application Postgraduate Symposium
   Hamburg, Germany, 29th August - 3rd September 2015
   Contribution: ORAL

9. **Applying photonic crystal fibers to improve sensitivity in Raman spectroscopy**
   M. Pollard, M. Triches, P. Westergaard, M. Lassen, J. Petersen, M. Matteucci
   DOPS 2015, Odense, Denmark, 19th-20th November 2015
   Contribution: ORAL

The only way to make a difference is to be different and do what the others aren't doing… I train twice on Christmas Day because I know the others aren't training at all, so it gives me two extra days.
L'unico modo per fare la differenza è di agire diversamente dagli altri… Io mi alleno due volte il giorno di Natale perché so che i miei avversari non si allenano affatto, questo mi da due giorni di vantaggio.

Daley Thompson

1 Introduction

This thesis is meant to be a collection of the work performed over a three-year Ph.D. project. The outcome has already been published as full papers in scientific journals. The published manuscripts are attached at the end of this thesis. Knowing the paper content in advance is not mandatory, but it might help the reader through the dissertation, so it is kindly recommended. In fact, in order to improve the readability, only the essential background is included. Most of the theoretical and experimental knowledge about the laser stabilization and frequency standards is not reported as the production of a handbook of laser frequency stabilization is beyond the scope of this dissertation.

1.1 Motivation

Since the redefinition of the standard meter in the 1960, the interest about optical frequency reference grows together with the needs of more precise and reliable measurement apparatus. Alaready at the end of the 18th century, with the first experiment reported by Michelson et al., interferometry had become the method of choice for precise measurements of length [1]. The practical problem of comparing distances measured typically in åmströng with the definition of the standard meter, based on the platinum-iridium prototype, kept at the Bureau International des Poids et Mesures (BIPM), arose the demand of a redefinition of the standard meter, based on the orange line of kripton-86.

With the advent of the laser (which incidentally occurred in the same years), the limitation of the standard based on the kripton lamp gradually became clear. Already in the 1972, the methane-stabilized laser proposed by Evenson et al. showed that the main limitation to the uncertainty of the interferometric measurement proposed was due to the asymmetry in the kripton line defining the meter [2]. This rapid progress ends up to a final re-definition of the *meter*, which took place in 1983, attributing a constant value to the speed of light in vacuum. With the actual definition, any optical transition can potentially be used to define the standard meter based on a laser-stabilized source.

The development of laser stabilization techniques based on atomic and molecular reference grows with the needs of more precise measurements for academic and industrial purposes. The performance of an optical frequency reference is defined by three basic parameters: *instability*, *uncertainty* and *reproducibility*. The *instability* is typically measured relative to the *expected* optical frequency at a given averaging time (called *fractional frequency instability*) and it quantifies the drift of the laser frequency over time. The *uncertainty* is the error associated with the measured optical frequency standard and it is typically expressed in terms of number of standard deviations (1σ, 2σ, ...). The *accuracy* can sometimes be confused with the uncertainty associated with the optical frequency reference. According to the BIPM, the accuracy describes how far the measured optical frequency of system developed is with respect to the *expected* value, usually given by the *primary* standard. The *reproducibility* of a system tells how much the system is reliable, how well it can reproduce

the given performance in different experimental condition (i.e. different detectors, different location, ...). It is also expressed relative to the *expected* optical frequency.

In metrology, the continuous improvement of the laser stabilization techniques aims to achieve better optical references, reducing both the instability and the relative uncertainty. On the other hand, the progress of the laser technology leads to novel breakthrough instrumentation. The advent of the frequency comb is only the most recent achievement [3], which combined with a stable and reliable optical frequency reference might bring to a possible redefinition of the *second* [4]. But this evolution is also important outside metrology as these improvements lead to beneficial effects for the society and for industrial applications, including IT services, commerce and transportation.

Nowadays, the telecommunication are using almost the electromagnetic spectrum to bring internet data all over the world. The dominant technology driving this service is provided by the optical fibers. Nowadays, optical fiber-based communication hold the majority of the volume of transferred data and the synchronization of the transmitter/receiver station is demanding for more stable and reliable frequency-stabilized lasers *away from the laboratories*. Remote sensing is another demanding field: monitoring air pollution and the detection of small concentration of harmful byproducts are of a great importance for overall healthfulness of the society [5].

Despite both industrial and metrological applications requiring improvement of the available optical frequency references, they are essentially pointing in two different directions. In metrology, the main goal is represented by the improvement of the absolute performance: the improvent of the atomic clocks using laser cooling techniques [6] and the realization of optical clocks usign frequency combs [3, 4, 7] and ultra-cold atoms [8] or optical lattices [9, 10] aim to improve the primary standard. The scope is to reduce the uncertainty from 10^{-15} down to 10^{-18} level [11] and beyond. Although their outstanding performance, the alternatives to the caesium standard are currently *secondary standard* realization of the second and their traceable uncertainty is still 1×10^{-15}, since they are limited by the linking to a caesium primary standard. In order to be considered as primary standards a redefinition of the *second* by the BIPM is required.

On the other hand, the major requests of industrial and remote sensing applications can be summarized with few key-words: *cost-effective*, *size and weight-reduction*, *reliability*. These applications drive the investigation on transferring consolidated frequency stabilization techniques into a compact and portable frequency standard. The study reported in this thesis is an example of this technological transfer-based research. The main topic of my Ph.D. thesis falls within the fields of precision spectroscopy and applied metrology, and it is meant to improve the portability of the optical frequency reference, addressing some of the requests of the remote sensing applications.

1.2 Laser Frequency Standard: State of the Art

Most of the laser stabilization schemes available nowadays are well known and extensively investigated in the literature: Saturated Absorption Spectroscopy (SAS) [12–15] combined with frequency modulation spectroscopy [16, 17], polarization spectroscopy [18] and two-photon spectroscopy [19]. The technology behind this study is well known: the heterodyne detection scheme combining SAS and frequency modulation spectroscopy has been introduced by Hall for the first time [20] and it has been reproduced several times the past decades [21–24]. The portability of this technology has been historically limited by the size of the vapor cells used to contain the reference gas: reducing the size reduces of the interaction length, producing a performance drop.

The first demonstration of the a hollow-core (HC) fiber guidance in air [25] open the possibility of extending the interaction length of the conventional gas cell using gas-filled HC fibers. The increased availability of HC fibers with different light guidance region allowed to realize *portable* optical frequency reference based on a gas-filled HC fiber [26–30]. Although the majority of the studies focuses their attention to a restricted number of optical references, like I_2 [31], rubidium [32] and acetylene [27, 28, 33], the HC fiber technology open the door to a number of a *weak* absorbing molecular reference (methane, CO_2), especially in the near infrared region, thanks to the almost extended interaction length provided. The possibility of using wider variety of molecular references helps to reduce the complexity of the frequency standard realization and it can provide an optical reference for a wider spectral range.

Limiting the discussion to the telecomunication band, the recommended optical transition for the secondary realization of the meter [34] can be given by ^{87}Rb (crossover hyperfine transition D2) at 780 nm, ^{85}Rb (two-photon absorption) at 778 nm and the $^{13}C_2H_2$ P(16) ($\nu_1 + \nu_3$) line at 1542.3837 nm. A telecom laser (1550 nm) can be directly tuned to the recommended acetylene transition, while a Rb-stabilization of a telecom laser can be achieved using an a frequency doubler. The needs of an optical frequency doubler and the reported loading speed of $\sim$10 cm/month [32] makes the Rb-filled HC fiber approach difficult to implement at the industrial level. With the target of a *cost-effective* optical frequency standard in the telecommunication band, I decided to limit the investigation to the recommended acetylene transition. This decision removed any issue related to fiber filling, however developing a portable and user-friendly optical frequency standard is still not free of challenges. From the fiber selection to the sealing method applied, the desirable approach is still under debate.

About the fiber selection, the state of the art investigations suggest that large core kagome fibers produce better performance than the commercially available Hollow Core Photonic Crystal Fibers (HC-PCF), both in terms of reproducibility and instability [29, 35], due to the limited transit-time broadening. On the other hand, the large core HC fibers have typically the drawback to be highly multi-moded, causing an increased instability in long term measurments [29]. Regarding the fiber encapsulation method, the fabrication processes suggested in the literature are not ready to be production-oriented and their long term performance is still not satisfactory for the commercialization.

The majority of the results published so far [26, 30, 35, 36] suggest to splice the HC fiber directly to a standard single-mode (SM) telecom fiber, using a dedicated filling technique [37]. This approach is limited by the loss of a SM-to-HC splice, typically between 2 and 3 dB [38]. If an angled splice is chosen to avoid etalon effects occurring between the silica fiber interfaces [37], the insertion loss can be even higher [39]. Therefore, despite the compactness achievable, the splicing approach is not delivering the wanted performance and the gap between the conventional free-space experiments and the HC fiber-based one requires to be reduced.

1.2.1 Acetylene-Based Standard: state of the art

In order to have clear in mind the performance achievable nowadays, the state of the art of the acetylene-based optical frequency references is reported in Table 1.2.1. The performance of the best (to my knowledge) commercially available optical frequency standard at 1542 nm is also reported [40].

Table 1.2.1: State of the art of the acetylene-based optical frequency standard. Each result is described in terms of the used experimental conditions: free-space beam propagation with conventional glass cells [24, 41], HC fiber-based with free-space coupling [29] or spliced HC fiber based [35]. The instability refers to the fractional frequency instability at 1 s. In [29, 35] when the uncertainty/reproducibility is given using the $\pm\Delta$ format, if not specified, Δ is interpreted as a maximum error: the standard deviation is calculated assuming a flat distribution ($\sigma = \Delta/\sqrt{3}$).

Solution	Uncertainty (1σ)	Instability (1s)	Reproducibility (1σ)
Neoark [40] Commercial	5.0×10^{-10}	1.0×10^{-11}	5.0×10^{-11}
Nakagawa et al. [21, 41] Free-space glass cell	5.7×10^{-10}	2.0×10^{-13}	2.0×10^{-11}
Hald et al. [24] Free-space glass cell	2.6×10^{-11}	5.0×10^{-13}	4.3×10^{-13}
Knabe et al. [29] Free-space HC-based	2.8×10^{-11}	1.2×10^{-11}	2.8×10^{-11}
Wang et al. [35] Spliced HC-based	4.4×10^{-10}	7.0×10^{-11}	5.8×10^{-11}

Excluding the commercial product, the first two academic experiments [21, 24, 41] are performed using conventional vapor cells with free-space coupling. In [29] a HC (kagome) fiber is used as a vapor cell, the fiber is put in a vacuum chamber and the light is free-space coupled. In [35] a HC (kagome) fiber is spliced to solid core fibers in a *portable*-like configuration. It is easy to see that the best published results of an optical frequency standard in a *portable* configuration [35] cannot reproduce the performance of the free-space coupled HC fiber-based approach [29]. This fact is suggesting that the optical coupling

proposed (splicing) might affect the performance. On the other hand, instability e reproducibility are almost two order of magnitude higher than the one observed in the conventional vapor cell based experiments [24, 41]. The encouraging fact is given by the comparison with the commercial product: despite the described limitations, the performance of the spliced HC fiber-based solution is close to the commercially available optical reference. The last thing to be noticed is that the work reported by Wang et al. [35] is published in 2013, after the beginning of my Ph.D. study and it can be considered as the reference work to evaluate the results reported here.

1.3 Organization of the thesis

The aim of my Ph.D. project is to develop a a portable and ready-to-use optical frequency reference capable to reproduce the performance typically achievable only in the controlled environment of a laboratory. Within the ITN QTea network, each Ph.D./Postdoc has to complete some work package/deliverable related to its project: the technical work package of my Ph.D. was to deliver a *"fiber laser locked to sealed HC-PCF with a fractional frequency instability below 5×10^{-11} for averaging time greater than 1 second"*. With this target in mind, in my Ph.D. thesis the emphasis is posed on the *instability* of the optical frequency standard developed and on the *portability* of the stand-alone version.

The thesis is divided into five main chapters, which guide the reader through the HC fiber technology and its application as gas cell for precision spectroscopy and metrology applications. A sixth chapter is written to collect an external activity not related with the main topic of my Ph.D. thesis. At the beginning of each chapter a little summary of the content presented is reported to help the reader. **Chapter 2** introduces the main concepts of the HC fiber technology, focusing on some important aspects of the guidance mechanism useful for the comprehension of the dissertation (i.e. high order modes analysis, effective refractive index, ...). **Chapter 3** gives a brief introduction on the SAS and how the main experimental parameters (i.e. interaction length, pressure, saturation, beam size, ...) have an impact on the laser frequency-stabilization. The most important quantities used to the evaluate the performance of a frequency-stabilized laser are introduced. **Chapter 4** summarized

the results obtained with different HC-PCFs. In **Chapter 5**, some of the results are analyzed and a theoretical model explaining the correlation between the modal properties of a HC fiber and the frequency stability of the laser is proposed. **Chapter 6** aims at giving an overview of the novel HC fiber encapsulation method developed within the Ph.D. study. A detailed description of the technical issues encountered in the developing process, the dedicated tools developed and a comparative analysis with the state of the art performance is also reported. In **Chapter 7**, a brief introduction about the outcome of a collaboration on Raman spectroscopy in water-filled HC fiber is summarized. Despite it is not completely related with the main topic of my Ph.D. thesis, some of the results obtained can be useful for the future development of the next generation of HC fiber-based optical frequency standard.

1.4 Summary of the research activities

Paper I shows the main results performed with the HC-PCFs tested. The laser frequency stabilization is achieved with a SAS setup combined with frequency modulation spectroscopy technique. The performance of the different fibers tested is evaluated using a vacuum box with anti-reflected coated window and the light is free-space coupled to the fiber deployed inside the box. This test is compared with the state of the art of the acetylene-based in-fiber frequency-stabilized laser[29]. The fibers are compared also in terms of modal content and a correlation between the number/type of the guided High Order Modes (HOMs) and the experimental results is observed. A simple theoretical approach is proposed to explain the mechanism behind the light-matter interaction between different spatial modes. After reconsideration, the model has been judged misleading in a certain extent and the theoretical approach I propose in this thesis is meant to be a revision of the one published in the paper.

Paper II is the outcome of a collaboration between DFM and the VTT Laboratories in Helsinki (Finland). The paper proposed different methods to overcome the issue of the interference effect between the two counter-propagating beams. The paper can also be considered as a certification of the portability of the stand-alone optical frequency standard I developed during my Ph.D. .

In fact, the system, assembled at DFM, is shipped to Helsinki to be compared with the optical standards at VTT. In this work, I contributed with the development of the stand-alone system and with the performance evaluation of the system.

Paper III is showing the performance of the stand-alone optical frequency standard developed at DFM. A novel encapsulation method for the gas-filled HC fibers is presented and the main details of the fabrication method are underlined. The system is the same one shipped to Finland and reported in the previous paper. The unchanged performance before and after the shipment proves the portability of the technology. The investigation is focused on discriminating the source of the increased pressure broadening observed during the first six months after sealing. A dedicated test is developed to clarify the situation and the performance of the sealed HC fiber-based system is compared with the state of the art [35].

Paper IV is the outcome of a collaboration between DFM, NKT Photonics and the Niels Bohr Institute (Copenhagen University). The scope of the collaboration is to develop a space-compatible optical frequency reference at 2 μm for remote sensing application. The study has been supported by the European Space Agency (ESA). The technical skills I acquired about the fiber encapsulation process has been extremely useful for the final realization of the presented prototype.

Paper V is the results of a collaboration with former colleagues at DTU Nanotech and DTU Physics for the development of an in-fiber Raman sensor for aqueous solutions. My interest about this application has been initially driven by the research of different fiber encapsulation solutions for the HC fiber. The injection-molded system used was initially developed for blood cell optical stretching applications. Since a preliminary investigation about in-fiber Raman spectroscopy was already planned at DFM, I decided to expand my knowledge about in-fiber sensing applications, studying the optical properties of the injection-molded microfluidic system. The study can be considered as a proof-of-concept evaluation for a possible future application.

Life is like a box of chocolates. You never know what you're gonna get.
La vita é come una scatola di cioccolatini, non sai mai quel che ti capita.

Forrest Gump

2

Hollow-core Fiber Technology

In this Chapter I define some of the main concepts about the hollow-core fiber guidance mechanism, which are important for some considerations made later on this dissertation. The specifications of the fibers tested in this study are published in **Paper I** (Table 1) are also reported here. In addiction, some techniques used to characterize the fibers are presented, such as Windowed Fourier Transform (WFT) analysis of the fiber transmission spectra and an Atomic Force Microscope (AFM) investigation on the fiber crystal structure. I aim to provide a more detailed description about these techniques, including some of the aspects omitted in the papers.

2.1 Fiber guidance: basic concepts

Since the demonstration of the first fiber guiding the light *in air*, many different HC fibers have been developed. The fabrication technique is similar for all the fibers fabricated so far. A stack-and-draw process is performed, where the design generated by stacking glass capillaries of different size/shape is transferred into the fiber by pulling the glass structure. During the stacking, a the core is created by removing some capillaries from the center of the stack, where the light is meant to be guided. The drawing process is happening in two phases: (i) several *canes* are drawn from the stack and (ii) from each cane the fibers are drawn subsequently. Before drawing the fiber, the canes are inspected and some parameters of the crystal structure are measured to fine-tune the fiber drawing step in order to obtain the desired product. This process requires a precise control of the temperature and the drawing speed. A detailed description of the drawing process is out of the scope of this section. More details about how to predict the final design of the fiber by fine-tuning these parameters can be found in [42]. In order to give a flavor of the possible different design developed so far, an extensive overview can be found in [43] and it is reported in Figure 2.1.1.

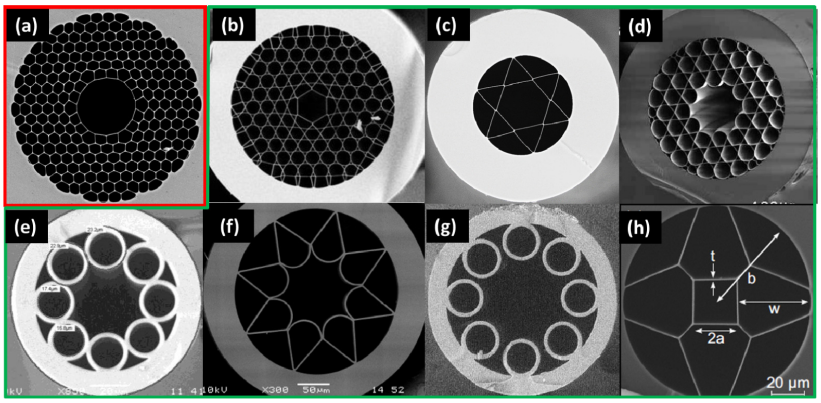

Figure 2.1.1: Reproduced from [43] with permission.(a) Hollow-Core Photonic Crystal Fiber (HC-PCF); (b-h) anti-resonant fibers. In particular, (b) and (d) have a Kagome cladding; (c) and (h) are simplified Anti-Resonant Fibers (ARF); (e), (f) and (g) are simplified hollow core fibers with *negative curvature* core surround.

Despite the great difference observable *by eye*, the guidance mechanism can be connected to the same principle: the *anti-resonant* mechanism. As recently demonstrated by Poletti in [43, 44], the guidance mechanism is given by *anti-resonant* elements present in the core-wall or in the cladding structure. The basic idea is that the optical frequency launched in the fiber can be *in-resonance* with the structure surrounding the core: in this case, the light can is not confined in the core and it can propagate inside the glass structure via surface modes/cladding modes and vanish due to their high propagation loss ($\sim 10^3$ dB/m). However, if the light is in *anti-resonance* with the glass structure (resonators), it will be *confined* in the core and it cannot escape by coupling to the cladding modes. In the so-called Photonic Crystal Fibers (PCFs) (Fig. 2.1.1, a) the anti-resonant elements are given by the *apexes*, which are the glass nodes within the capillaries in the cladding. These fibers are also called *photonic bandgap* fibers because the guidance mechanism has been historically ascribed to the periodicity of the cladding cladding structure, simply considering the cladding structure as 2-D photonic crystal. In the Kagome fiber (Fig. 2.1.1, b and d), the anti-resonant element is given by the core wall. Finally, in the recently developed *Anti-Resonant Fiber* (ARF), the anti-resonant elements are given by the capillaries forming the cladding structure.

Different structures give different guidance properties and once decided the fiber design, these properties can be tuned by controlling the anti-resonant elements and the defect size/shape. In my Ph.D. project, I only worked with HC-PCFs provided by NKT Photonics and the close collaboration with the manufacturer helps me in the selection of the most suitable fiber for studied application. For the purposes of this study, I limit the description of the optical properties of such fibers to the following elements:

1. Core size
2. Number/type of guided modes
3. Effective refractive index of the modes

The first element is extremely important in SAS because the Mode Field Diameter (MFD) of the propagating light is ruled by the core size. In fact, the size MFD is one of the key parameters which determines the linewidth (and therefore the stability) of a in-fiber SAS experiment (3). The core size is mainly

determined by the number of *cells* (glass capillaries) of which the core is made of. A typical HC-PCF core is made of 7-cell or 19-cell, but demonstrations from 3-cell up to 37-cell fiber have been reported in the literature [43, 45]. The number and type of guided modes is fundamental to define whether the fiber is Single Mode (SM) or Multi Mode (MM) at the operational wavelength. A SM mode fiber guides only one mode, usually called Fundamental Mode (FM). A MM fiber guides a number of (spatial) modes different form that FM, which are called High Order Modes (HOMs). In general, a HC fiber guides more than one mode and it is *not possible* to couple all the light coming from a Gaussian beam (free-space) into the FM, because the overlap integral between the FM and a Gaussian mode is theoretically limited to ~ 0.9, slightly varying from fiber to fiber. When a HC fiber is defined SM, it is generally meaning that the fiber has an *effective* SM behavior, due to the higher loss of the HOMs or limited to a restricted portion of the transmission band. Only one single example of a HC fiber with SM property that covers the almost the entire transmission band can be found in literature [45]. This fiber reported is 3-cell fiber with a *triangular* core, which is smaller compared to the the more common 7-cell HC fibers.

2.1.1 Effective refractive index

Figure 2.1.2 (left) shows the the density of modes (in red scale) with respect to the effective refractive index of the mode of a given HC-PCF. The fiber represented has two *transmission bands*: a *small* one at shorter wavelength (dark region between 0.8 μm and 0.95 μm) and the *main* one (between 0.95 μm and 1.3 μm) A closer look inside the main transmission band shows the modes guided inside the core (Fig. 2.1.2, right). The representation is based on the concept of the effective refractive index (n_{eff}), which is defined as

$$n_{\text{eff}} = \frac{\beta}{k_0} = \frac{\beta\lambda}{2\pi} \tag{2.1}$$

where β is the propagation constant of the mode in the fiber. The n_{eff} of the light propagating in a waveguide/fiber has the analogous meaning of the refractive index for light propagating in a homogeneous medium.

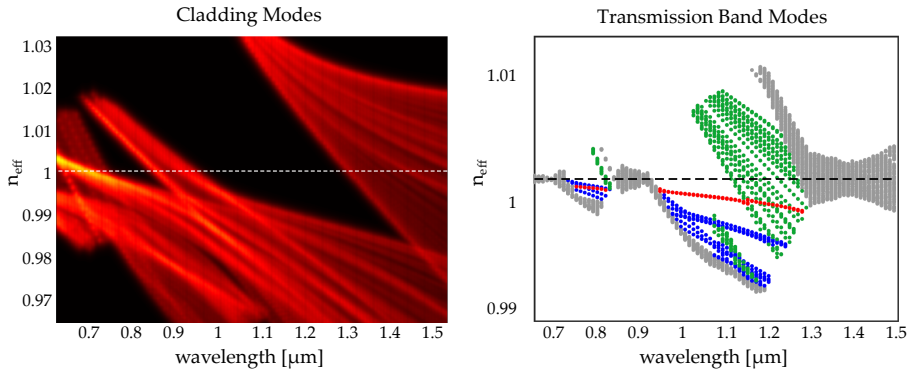

Figure 2.1.2: Typical representation of the HC fiber modes in terms of effective refractive index (n_{eff}). On the left: density of cladding modes On the right: a close loop of the *transmission band* modes. In details: the cladding modes (grey), surface modes (green), HOMs (blue) and FM (red). It is easy to notice that the represented fiber has two *transmission bands*. Courtesy of NKT Photonics A/S.

The n_{eff} is related to the phase velocity of the light (v_{ph}) propagating a mode guided by the HC fiber, since v_{ph} is not equal to speed of light, despite the light propagation in air/vacuum ($n_{air} \simeq 1$). Therefore, the n_{eff} is not depending on the material crossed by light, but it is defined by HC fiber guidance. This concept is still valid in presence of refractive index significantly different than 1. For example, in case of water-filled HC fiber, the presence of the water *shifts* the transmision band at shorter wavelength, as reported in [46]. The n_{eff} is depending both on the mode and on the wavelength in which the light propagates, as shown in Fig. 2.1.2, meaning that different modes have different propagation constants (β). This concept is the key point to understand the considerations that I will introduce in Chapter 5 about the different Doppler effect experienced by molecules interacting with different modes in a HC fiber.

2.1.2 Effective group refractive index

Another concept which will be useful for the rest of the dissertation is related to the group refractive index n_g. It can be observed that the n_{eff} depends not only on the mode but also on the wavelength of the propagating light. This feature makes the HC fiber a *slightly* dispersive medium. The n_{eff} contains information only about the phase velocity of light, but not on the group velocity.

As reported in **Paper I**, the effective group index n_g can be defined in analogy to the group index for plane waves in a homogeneous dispersive medium

$$n_g = n_{eff} - \lambda \frac{dn_{eff}}{d\lambda} \tag{2.2}$$

where λ is the wavelength in vacuum. The n_g is related to the group velocity (v_g) of the mode in the fiber. The difference in effective group refractive index (or simply *group index*) between the modes allow to experimentally evaluate the number of modes guided by an HC fiber, as explained later on in section 2.3.2.

2.1.3 HOMs and Surface Modes

Before going into the details of the fiber characterization, both in terms of simulations and experimental measurements, some general comments about general features observable in a HC is needed. As previously mentioned, a common 7-cell HC fiber usually guides more than one mode. The HOMs and the FM are guided inside the core while the surface modes are confined inside the glass structure surrounding the core and inside the core wall. The FM is typically the mode with lower loss ($\leq 10^{-2}$ dB/m) and it has a *Gaussian-like* intensity distribution (LP_{01}). A number of other modes (HOMs) are also guided theoretically, but only the HOMs with lower order are practically guided due to their limited loss (typically LP_{11} components, loss $\leq$ 1 dB/m) compared to higher order ones (loss $\geq$ 10 dB/m). Three mechanisms can produce an higher intensity in the HOMs, such as (i) non-perfect initial coupling condition, (ii) mode coupling.

The major responsible for the amount of light coupled to the HOMs and surface modes is the initial coupling condition. In an ideal system, when a free-space laser beam is coupled into a HC fiber, in the optimal coupling condition the amount of light coupled to the different spatial components can be calculated from the overlap integral between the launching beam and the HC fiber mode considered. Theoretically, since the overlap integral between a Gaussian mode and the FM of an HC fiber is limited to $\sim$ 0.9, a transmission coefficient (ϵ) greater than 0.9 is expected. In practice, an overall lower performance of the fiber is experienced ($\epsilon \approx 0.7$), mainly due to a non-perfect coupling condi-

tion. The difference between the theory and the experiments can be ascribed to the higher amount of light coupled to the HOMs and surface modes, which have a higher propagation loss with respect to the FM.

The second mechanism is called *mode coupling* and it can occurs in two ways. The core modes are *orthogonal* (described by orthogonal polynomial) which means that a direct coupling (exchange energy) between the core modes should not occur. In practice, due to to the Rayleigh scattering, a certain amount of energy exchange between FM to the HOMs can be observed. The Rayleigh scattering is caused by the roughness of the core wall inner surface and it is also the major responsible for the propagation loss of an HC fiber (up to 1.5 μm). In general, this mechanism has a preferential direction: from the *lower order* modes (like LP_{01}) to the *higher order* modes (LP_{11} and higher). The other way (light pumped back to the core low order modes) can be mediated by the surface modes. The overlap between the electric field of the core modes and the one confined in the glass structure surrounding the core (surface mode) makes possible an energy exchange between the core modes and the surface modes. These effects can be enhanced/affected by some other external perturbations such as (i) temperature variation, (ii) tight coiling and fiber, (iii) twisting or by a combination of these. All of these perturbations are somehow causing a mechanical stress on the fiber, which affects the propagation constant of the modes, by changing the effective refractive index or increasing the fiber loss. These concepts will be used in Chapter 5 to estimate the amount of light coupled to the different spatial components of one of the fibers tested.

2.1.4 Polarization and birefringence

A separate description should be given for the polarization in HC fibers, especially regarding to the polarization maintaining (PM) fiber. In step-index fiber the PM property is generated by the introduction of stress elements which modify the circular symmetry of the core fiber structure [47], generating the so-called *highly induced birefringence*. If a linearly polarized light is launched into the fiber aligned with one of the birefringent axes, the polarization state will be preserved. The propagation constants of the two orthogonal polarized modes are different due to the built-in birefringence, so that the relative phase

between these two modes drifts away. Therefore, only a perturbation that matches the two phases can couple both modes. The physical principle is similar to the mode coupling introduced in the previous section. In HC fiber the mechanism is similar but the main difference is caused by the stress elements. While in the standard step-index fibers the circular symmetry is broken via two stress elements introduced in the cladding [47], in the HC fibers the stress elements are typically introduced in the core wall [48]. These elements are introduced in order to increase the fiber birefringence along two axis, which are called the *fast* and the *slow* axes. An issue caused by this technique is given by the same stress elements introduced in the core wall: they contributes to increase the surface modes and they makes practically impossible to avoid coupling light into these elements, since they are so close to the core. Since a PM fiber requires a perfect alignment with one of the two axes in order to produce the wanted PM performance, this solution has some practical drawbacks. Recently, some examples of PM HC fiber with the stress elements introduced in the cladding have been demonstrated [49, 50]. This novel approach is not only improving the the PM properties, but it contributes to strip the surface modes and the HOMs, leading to a fiber with an improved SM behavior. In conclusion, the PM property is introduced through a built-in birefringence, leading to two polarization modes with different propagation constant. This fact makes a PM fiber similar to a *two-mode* fiber. If the PM property is reduced by a poor coupling/alignment condition with the fiber axis, the cross-talk between the two is possible. The negative effects on the frequency stability on a SAS experiment in a HC fiber similar to [48] are described in **Paper I**.

2.2 Fibers investigated in this study

Using the concepts introduced so far, it is possible to describe the four different HC-PCFs investigated in this study. The fiber specifications are summarized in Table 2.2.1, making use of the same labeling, definitions of modal content and the PM properties reported in **Paper I**.

Table 2.2.1: Reported from **Paper I**. Summary of the fiber characteristics.

Specs/Name	C7_PM	C7_L	C7_S	C19
Core	7-cell	7-cell	7-cell	19-cell
Core diameter	9.3 μm	11.9 μm	8.5 μm	20.0 μm
MFD	6.8 μm	8.2 μm	5.4 μm	13.2 μm
Coupling	63%	67%	61%	72%
PM property	PM	non-PM	non-PM	non-PM
Mode property	single-mode	*few*-mode	single-mode	multi-mode
Structure				

2.3 Experimental Fiber characterization

All the fibers tested have been provided by NKT Photonics and they are experimentally characterized for the HOMs content, using a Windowed Fourier Transform (WFT) analysis as reported in **Paper I**. In one case (C7_L fiber), a simulation of the first HOMs is performed to verify the agreement between the modal properties measured with the WFT analysis and the theoretical prediction. A proof-of-concept experimental measurement using an Atomic Force Microscope (AFM) has also been attempted to characterize the photonic crystal structure. The aim of this test was to support the simulations in order to obtain more reliable numbers. The simulations are typically performed starting from the designed model of the photonic crystal structure. The geometry is usually tuned using the parameters measured on the cane during the fiber drawing process, according to [42, 51]. A final fine-tuning of the simulation is performed using the transmission properties measured on the fiber, in order to match the simulated transmission band with the measured one. Some critical parameters of the PCF structure like the radius of curvature of the apexes, the shape and the thickness of the struts are non trivial to predict using the measurements performed on the cane.

An alternative approach to retrieve useful information for the simulation is to to apply a metal coating on the fiber facet and take a Scanning Electron Microscopy (SEM). This approach is anyway inaccurate it actually measures the geometry of the metal coating applied, making all the measurement dependent on the success of the metal coating process. In order to improve such approach, I proposed to investigate the PCF structure using an AFM. This method avoid the metal coating, because the fiber facet can be measured directly by the microscope tip. However, the measurement presents some challenges. The major one is given by the fiber position: the fiber needs to be place vertically with respect to the AFM tip as any angular misalignment of the fiber will be detrimental for the success of the measurement. In order to have a reliable measurement equipment, the development of some special AFM tools for a correct and reliable characterization is required. Since the development of these tools was out of the scope of my Ph.D. project, I decided to do not pursue the first proof-of-concept measurement performed. For these reasons,

despite the promising results, the measurements have not been reported in a manuscript.

2.3.1 AFM: GEOMETRY INVESTIGATION

The AFM investigation is performed by taping a piece of 8 mm of the C7_S fiber on microscope glass sheet. The glass sheet is clamped on the AFM platform with the cleaved facet of fiber upwards. The AFM operation is quite simple: it scans the structure with the given resolution (usually measured in lines/μm) measuring the height of the sample. Using these information, a grey/color scale contour plot of the structure can be obtained as presented in Fig. 2.3.1.

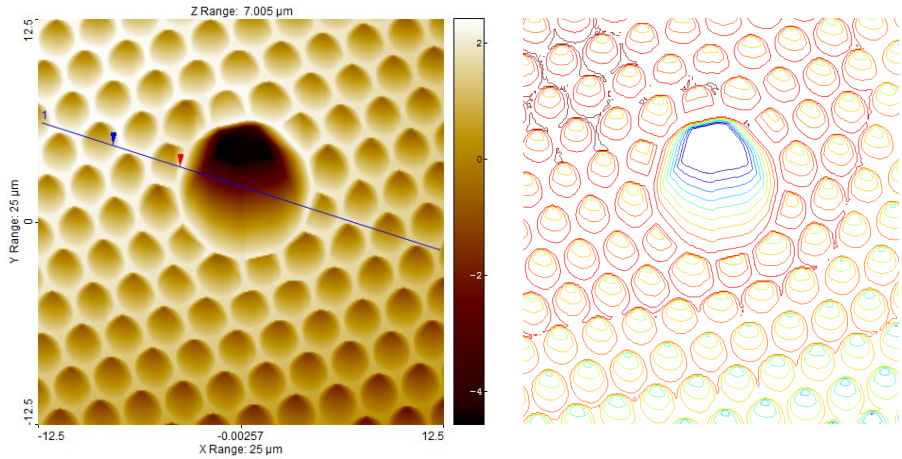

Figure 2.3.1: AFM investigation of the C7_S fiber. Left: the image produced by the AFM software. The color legend on the right side shows the color-to-height conversion (in μm). Right: post-processing of the raw data generating the contour lines. The contour lines are plotted in a red-to-blue scale in a top-to-bottom representation of the height measured by the AFM.

The measurement is taken on a 25 μm$\times$25 μm over the core and the different colors represent different height/depth level of the sample. The measurement time is about 30 min to 2 hours, depending on the resolution required, which is a significant improvement with respect to the SEM image process. The following step could be using such information to automatically reconstruct the

fiber structure, by converting the raw data into *contour lines*. This operation is not straightforward, as shown in Fig. 2.3.1 (right). A small misalignment of the fiber position and the tip geometry should be considered in order to correctly reconstruct the sample structure, requiring a dedicated data post-processing. Although this approach can potentially improve the reliability of the simulations, it requires time to be implemented properly. Future investigations can be pursued in this direction, especially on the development of a dedicated fiber holder for the AFM investigation. Holding the fiber a vertically with respect to the measurement plane with minimal uncertainty can improve the reliability of the measurement.

2.3.2 In-Fiber Mach-Zender Intereferomtry:modal investigation

The HOM characterization is performed using the setup presented in Fig. 2.3.2, similar to the one presented in [52].

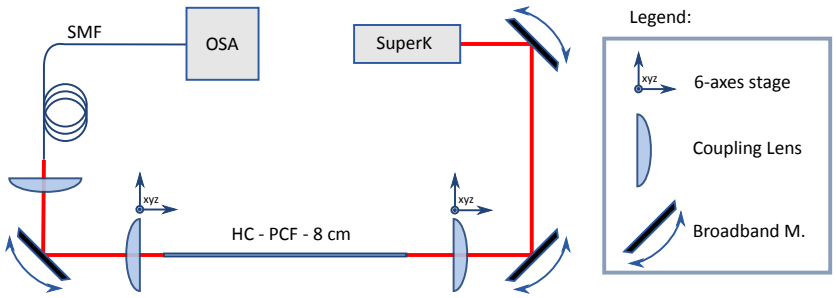

Figure 2.3.2: Setup used for the WFT analysis. A super-continuum source (0.45-2.4 μm) is coupled to a piece of 8 cm of HC fiber and is collected with a SM step-index fiber into an optical spectrum analyzer (OSA). Each spectrum is recorded across most of the fiber band gap with 0.1 nm resolution.

The detailed description of the in-fiber Mach-Zender inteferometer is reported in **Paper I**. The basic concept behind this technique is the different group velocity experienced by the light coupled into the different modes. In case of a broadband source like the SuperK provided by NKT Photonics, the concept of group index n_g defined in Eq. (2.2) can be used to discriminate the different modes, since a *group delay* is accumulated by the light coupled into different modes along the fiber. The results presented in **Paper I** show the different

modal property of the tested fiber, confirming the mode property reported in Table 2.2.1. In this Section the coupling dependence of the modal content of an HC fiber is investigated with the WFT analysis described in **Paper I**. The effect is presented in Fig. 2.3.3 where the fiber modal content in presence of a misalignment of the in-coupling beam is compared with the optimum alignment condition.

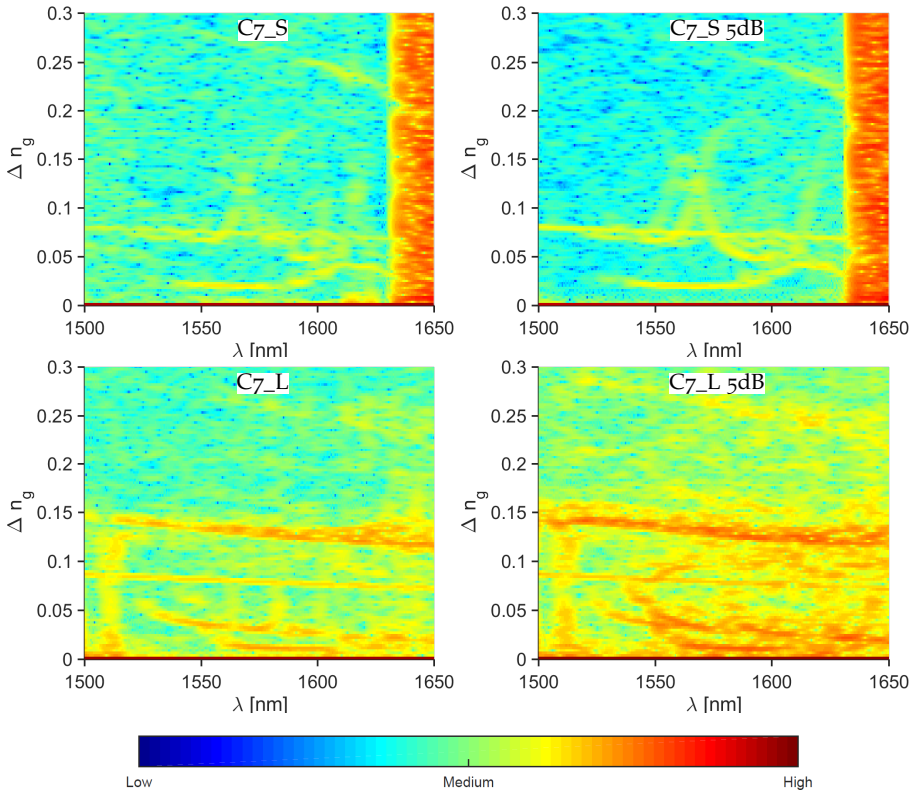

Figure 2.3.3: WFT analysis of the C7_S and C7_L fiber in a optimum coupling configuration (left) and with a misalignment on the in-coupling beam (right). The misalignment is applied in order to give a 5dB lower intensity on the OSA.

The results obtained with the C7_S and C7_L are compared. The figures representing the optimal coupling condition (Fig. 2.3.3, left) are reported from **Paper I** for clarity. The misalignment introduced to check coupling dependence of the modal content is chosen to produce a signal drop on the OSA

of 5 dB at 1542 nm for both the fiber (Fig. 2.3.3, right). The analysis shows clearly that while the C7_S fiber shows negligible difference in the modal content between the two configuration, the C7_L fiber shows an higher presence of HOMs combined with an overall with an higher intensity associated to the HOMs relative to the FM. It is important to underline that 5 dB drop in optical transmission is *strong* misalignment, much greater than any drift that can potentially occur during a SAS experiments. This value has been chosen because it is the *threshold* level for the C7_S fiber: smaller misalignment does not show any significant changes in the C7_S fiber modal content, confirming once more the SM-like performance of the fiber over almost the transmission band.

2.3.3 Technology limitations: parameters to investigate

As previously underlined, the fiber technology has some limitations that cannot be easily solved, if they are meant to be used in SAS experiments. In order to push the state of the art performance of the in-fiber laser frequency stabilization, not only parameters like pressure, fiber length and power need to be taken into account. As already anticipated in this chapter, the modal content is a key parameter to improve the frequency stability. In the next Chapter the key parameters are defined with some basic theoretical concepts, with the scope of preparing the subsequent discussion.

Science is the belief in the ignorance of experts.
Scienza è credere nell'ignoranza degli esperti.

Richard Phillips Feynman

3

Laser Frequency Stabilization: Doppler-free Spectroscopy

In this chapter I summarize the basic concepts of laser frequency stabilization in order to recover the minimal information required to follow the dissertation. After a brief introduction on the basic theoretical concepts of the SAS, I will focus on some parameters related to the experimental investigation and I will define some concept like the *instability* and *reproducibility*, which will used later on when discussing the fiber performance.

3.1 Saturated Absorption Spectroscopy: Basic Concepts

The concept behind the SAS is based on the velocity-selection of the molecules which mainly contributes to the signal by injecting two counter-propagating beams in the gas cell. Thanks to the Doppler effect, the class of molecules which *sense* the same optical frequency from both beams reaches a higher degree of saturation among the others. The higher saturation produces a non-linear absorption that results, in its turn, in a less opaque medium at that specific optical frequency. The mechanism can also be understood by using the "hole burning" concept described the first time by Bennet [53]. Assuming to address a two-level molecular transition, when one of the two beams (usually referred as *pump beam*) is injected into the vapor cell, the molecules are pumped from the ground state to the excited state. The optical pumping depends on the detuning of the pump with respect to the optical transition and it burns a *hole* in the molecular velocity distribution. The interaction with the pump reduces the number of molecules available on the ground state with a specific velocity component along the light propagation axis. When the counter-propagating beam (usually referred as *probe beam*) is interacting with the same molecular class, it finds an excess of molecules in the excited state, having lower probability of being absorbed by the medium. This effect generates an excess of signal historically called *Lamb dip* [54]. This optical feature is usually referred to as *Doppler-free*, meaning the that the Full Width Half Maximum (FWHM, or simply referred as linewidth) is not affected by the first-order Doppler broadening. Second-order Doppler broadening is still present and can be removed only by using techniques such as laser cooling [55, 56].

Limiting our discussion to the SAS spectroscopy, in the ideal case of two counter-propagating beams aligned in free-space, it is easy to calculate the velocity component along the light propagation direction of the molecular center of mass that contributes to the Lamb dip. In order to *detect* the same optical frequency coming from both the counter-propagating beams, the velocity of the molecular center of mass must fulfill the following relation

$$\omega_0 - \omega_1 + \vec{k}_1 \cdot \vec{v} = \omega_0 - \omega_2 + \vec{k}_2 \cdot \vec{v} \tag{3.1}$$

where ω_0 is the frequency of the addressed optical transition, $\omega_{1,2}$ and $\vec{k}_{1,2}$ are the optical frequency and the wavevector of the probe/pump beam respectively. In general, $\omega_{1,2}$ can differ from ω_0, so that both beams have an arbitrary detuning ($\omega_{1,2} = \omega_0 + \Delta_{1,2}$) with respect to the molecular transition. For given probe and pump frequencies, the equation gives the velocity component along the axes of light propagation (v_z) of the class of molecules that *see* the same optical frequency for both the beams. This molecular class gives the highest contribution to the sub-Doppler signal in correspondence with the center of the Lamb dip feature. Defining $\vec{k}_1 = +k_1\hat{z}$ as the direction of propagation of the probe (and $\vec{k}_2 = -k_2\hat{z}$ for the pump), it is possible to calculate can v_z from Eq. (3.1)

$$
\begin{aligned}
-\Delta_1 + k_1 v_z = -\Delta_2 - k_2 v_z \Longrightarrow \\
v_z = \frac{\Delta_1 - \Delta_2}{k_1 + k_2} = \frac{(\Delta_1 - \Delta_2)\, c}{2\omega_0 + \Delta_1 + \Delta_2} \simeq \frac{(\Delta_1 - \Delta_2)\, c}{2\omega_0}
\end{aligned}
\tag{3.2}
$$

if $\omega_0 \gg \Delta_{1,2}$. Equations (3.1) and (3.2) are valid in the non-relativistic approximation, which is generally fulfilled for the molecular velocity of a gas at room temperature and assuming that the detuning between the two counter propagating beams ($|\Delta_1 - \Delta_2|$) is smaller than the linewidth of the optical transition ($|\Delta_1 - \Delta_2|/2 \leq \gamma$). If $|\Delta_1 - \Delta_2|/2 > \gamma$, the two beams *burns* two independent *holes* in the molecular velocity distribution and no Lamb dip will be observed. Therefore, when a relative detuning between the pump and probe occurs (within the mentioned boundary conditions), the center frequency of the saturation dip can be calculated using the non-relativistic Doppler formula

$$
\begin{cases}
\omega_1^{'} = \omega_1 \left(1 - v_z/c\right) \\
\omega_2^{'} = \omega_2 \left(1 + v_z/c\right)
\end{cases}
\tag{3.3}
$$

where $\omega_{1,2}^{'}$ refers to the frequencies observed in the reference frame of the reference frame of the molecular center of mass. When inserting v_z in Eq. (3.3), the optical frequency of the maximum of the Lamb dip ($\omega^{'} = \omega_2^{'} = \omega_1^{'}$) in the molecular reference frame can be calculated as a function of the pump/probe

optical frequencies measured in the reference frame of the laboratory ($\omega_{1,2}$)

$$\begin{aligned}\omega' &= \omega_2' = \omega_1' = \frac{\omega_2' + \omega_1'}{2} = \frac{\omega_1}{2}\left(1 - v_z/c\right) + \frac{\omega_2}{2}\left(1 + v_z/c\right) = \\ &= \frac{\omega_1 + \omega_2}{2} + \frac{\omega_2 - \omega_1}{2}\frac{v_z}{c} = \omega_0 + \frac{\Delta_1 + \Delta_2}{2} + \frac{(\Delta_2 - \Delta_1)}{2}\frac{v_z}{c} \\ &= \omega_0 + \frac{\Delta_1 + \Delta_2}{2} - \frac{(\Delta_2 - \Delta_1)^2}{4\omega_0} \simeq \omega_0 + \frac{\Delta_1 + \Delta_2}{2}\end{aligned} \tag{3.4}$$

The term $\propto \Delta^2$ is neglected because the factor Δ^2/ω_0 is typically on the order of 10^{-2} Hz. Therefore, the Lamb dip center frequency is expected to be at the average optical frequency of the two beams, in both the molecular and laboratory reference frame. It is important to clarify that the results is direct consequence of the relation introduced in Eq. (3.1): no other constraint are imposed. The relation $\omega' = \omega_2' = \omega_1' = (\omega_2' + \omega_1')/2$ is a pure mathematical equality used to simplify the calculation and it is valid in general. In Chapter 5 I will show how Eq. (3.1), (3.2) and (3.4) change due to the *space modulation* introduced by different spatial modes propagating inside a HC-PCF. A detailed description of the theory of the SAS can be found in [57, 58]. In order to study the above described SAS technique is essential to know the absorption coefficient (α) as a function of the main parameters such as pressure (P) of the gas, interaction length (L), optical intensity (I) and the relative detuning ($\Omega = |\Delta_1 - \Delta_2|$) between the two counter-propagating beams. In general, the two-level system can be described using the density matrix equation and it can be numerically solved for a chosen particular case of frequency detuning and intensities [57]. In some particular cases, when the counter-propagating beams have the same frequency ($\Omega = 0$) and same intensity ($I_1 = I_2 = I$), the system can be solved analytically in the rate approximation giving a general expression for the absorption coefficient [58]

$$\alpha(\omega, S, L, P) = L \cdot P \cdot \frac{\alpha^0(\omega_0)}{\sqrt{1+S}} \cdot \mathrm{e}^{-\left(\frac{\omega-\omega_0}{0.6\delta\omega_D}\right)^2} \frac{\gamma/2}{B\left[1 - 4\left(\frac{\omega-\omega_0}{A+B}\right)^2\right]^{1/2}} \tag{3.5}$$

with

$$A = \left[(\omega - \omega_0)^2 + (\gamma/2)^2\right]^{1/2} \text{ and } B = \left[(\omega - \omega_0)^2 + (\gamma/2)^2(1+2S)\right]^{1/2}$$

where $S = {}^{I}/_{I_s}$ is the saturation parameter, I_s the saturation intensity, γ the linewidth of the unsaturated absorption line and $\delta\omega_D$ is the Doppler linewidth as defined in [58], respectively. $\alpha^0(\omega_0)$ is the unsaturated absorption coefficient, measured in $\mathrm{Pa}^{-1}\ m^{-1}$. Equation (3.5) is valid for any arbitrary level of saturation S, which is defined as the saturation produced by one of the two beams. The *height* of the Lamb dip can be calculated as proposed in [58]

$$\frac{\alpha(\omega - \omega_0 \gg \gamma) - \alpha(\omega_0)}{\alpha(\omega_0)} = \frac{1}{\sqrt{1+S}} - \frac{1}{\sqrt{1+2S}} \tag{3.6}$$

If the intensity of one of the two beams is very small ($I_2 \ll I_1$), the following equation is obtained instead of (3.5)

$$\alpha_w(\omega, S, L, P) = L \cdot P \cdot \alpha^0(\omega_0) \cdot \mathrm{e}^{-\left(\frac{\omega-\omega_0}{0.6\delta\omega_D}\right)^2} \left(1 - \frac{S}{2} \frac{(\gamma_s/2)^2}{(\omega-\omega_0)^2 + (\Gamma_s/2)^2}\right) \tag{3.7}$$

where $\gamma_s = \gamma\sqrt{1+S}$ is the saturated linewidth and $\Gamma_s = {}^{(\gamma+\gamma_S)}/_2$ the average between the saturated linewidth (strong beam) and the unsaturated linewidth (weak beam). In Eq. (3.7), S is defined as the saturation given by the stronger beam. This configuration yields to a Lamb dip height of

$$\frac{\alpha_w(\omega - \omega_0 \gg \gamma) - \alpha_w(\omega_0)}{\alpha_w(\omega_0)} = \frac{S}{2}\frac{(\gamma_s)^2}{(\Gamma_s)^2} = \frac{2S(1+S)}{2+S+2\sqrt{1+S}} \tag{3.8}$$

instead of (3.6). Depending on the saturation level, the ratio between ${}^{\alpha_w}/_{\alpha}$ can vary between 1.3 and 6 for saturation level between 0.1 and 1. These relations are used to *weight* the different contribution between the interaction of different modes that occurs in the HC fiber filled with gas considered in Chapter 5.

3.2 Frequency Modulation Spectroscopy

In order to convert the sub-Doppler feature into a suitable signal for locking the laser frequency, many different methods can be implemented. A typical frequency locking scheme is based on a Proportional-Integral-Derivative (PID) component which require an voltage signal proportional to the laser

frequency to track the laser frequency fluctuations. Therefore, the ideal signal for locking is a voltage-to-frequency ramp with a zero crossing point at the addressed optical transition. Here I describe two different methods that can be used to obtain the wanted signal. The first one is used in the secondary standard of length developed at the Danish Fundamental Metrology and it is described in [24]. The laser frequency is modulated across the Lamb dip, by applying a sinusoidal signal to the laser driver (frequency modulation). By detecting the the signal before/after passing through the gas cell with a balanced detector, a fast component in phase with the modulation frequency can be detected. Once demodulated using a phase-sensitive detector (lock-in amplifier), it yields a signal that is proportional to the amplitude of the Lamb Dip and inversely proportional to the linewidth, with a characteristic dispersion-like form, centered at the optical transition. This laser will be referred as the *reference* laser later on in the dissertation, since it is used to measure the performance of the in-fiber SAS setup.

An alternative method has been proposed by Bjorklund [17, 59] and Hall [20] for the first time. The light of the probe beam is phase-modulated using an Electro-Optic-Modulator (EOM) using radio frequency (RF) synthesizer. The phase modulation generates an infinite number of coherently detuned light components called *sidebands*. If we limit the analysis at two first-order sidebands, in absence of an absorbing medium, the frequency modulated probe beam hits the detector and generates two beat notes at the modulation frequency (RF), in addition to the DC component. Since the sidebands have opposite sign, the two RF components cancel out. The presence of an absorbing medium between the laser source and the detector unbalance the situation. Due to the uneven changes in phase or amplitude between the sidebands. A demodulation of the produced beat note with the RF provided by the synthesizer is generating the dispersion-like signal used for locking. This second technique is used in the experiments discussed in this dissertation, since it can provide a fairly simple and compact locking scheme, which can be potentially converted into an *all fiber-based* apparatus.

3.3 Frequency Standard Characterization

In order to evaluate the experiments, some concepts and definitions need to be introduced. The performance of a optical frequency standard can be evaluated in terms of *relative uncertainty*, *reproducibility* and *instability*. Before defining such concepts, it is important to define the parameters of the SAS that might affected these three quantities. This section is not meant to be a full compendium about experimental parameters and their effect on the performance of the frequency-stabilized laser, therefore I will introduce only the key elements which are required for the following discussion.

3.3.1 Signal-to-Noise Ratio of the locking signal

Using the frequency modulation technique as defined in the previous section, the sub-Doppler feature generated by the SAS is converted in a ready-to-use voltage-to-frequency conversion signal for locking. The efficiency of the locking scheme depends directly on the ratio between the voltage *slope* provided and the noise level. The signal-to-noise ratio (SNR) of the locking scheme can be written as

$$\mathrm{SNR} = \frac{V - V_0}{\gamma} \frac{\nu_0}{\mathrm{noise}} \tag{3.9}$$

where V is the intensity (voltage) of the probe detected at center of the Lamb dip, V_0 the light intensity of the probe in absence of the pump beam, γ the linewidth (FWHM) of the sub-Doppler feature and ν_0 the frequency of the center of the Lamb dip, respectively. The *noise* is defined as the off-resonance Root-Mean Square (RMS) of signal used for locking. The inverse of the SNR can give an estimate of the expected fractional frequency instability of the locked-laser. Both the fractional frequency instability and the SNR calculated using this definition depends on the bandwidth of the detection scheme (usually defined by the integration time of the lock-in amplifier). For example, if V, V_0 and the *noise* are measured with a detection bandwidth of 1 Hz, $1/\mathrm{SNR}$ forecasts the fractional frequency instability of the locked laser at 1 second averaging time. A detailed definition of the fractional frequency instability is reported in Section 3.3.3.

The term $V - V_0$ is proportional to the height of the Lamb dip, as defined in Eq. (3.6) and (3.8). The linewidth of the Lamb dip in the typical experimental condition is governed by two different broadening effects: the *collisional* broadening (γ_P, known also as pressure broadening) and the *transit-time* broadening (γ_T). This two effect are independent, therefore in first approximation we can assume that the total linewidth of the Lamb dip is given by the sum of the two effects

$$\gamma = \gamma_T + \gamma_P \simeq 0.12\frac{\bar{u}}{w_0} + k_p P \tag{3.10}$$

where $\bar{u}$ is the thermal velocity of the molecules, k_p is the pressure broadening coefficient and w_0 is the beam waist. In the HC fiber the size of the mode is typically express in terms of the Mode Field Diameter (MFD), which can be considered as twice the waist (MFD $\simeq 2w_0$) [57, 60]. k_p of $^{13}C_2H_2$ is 234 kHz/Pa [33] and the $\bar{u}$ is about 430 m/s at room temperature, as reported in **Paper I**. While the contribution to the linewidth of the collisional broadening depends only on the pressure of the gas loaded into the fiber, the transit-time broadening depends on the beam size. The size of the FM in a HC fiber is proportional to the core size, therefore fiber with smaller core will give a higher contribution to the broadening.

The advantage of the HC fiber with respect to the free-space experiments is the chance to reduce the pressure broadening contribution. It is easy to see from Eq. (3.5) that once the reference gas has been chosen, the absorption is determined by the product of the interaction length (L) and the pressure of the gas (P). In the free-space experiments the interaction length is the limiting factor, therefore the pressure cannot be lowered as desired to keep the total absorption high enough to produce a detectable signal. In a free-space configuration, the interaction length is given by the Rayleigh range of beam, which is proportional to the beam size: increasing the interaction length requires larger beam size (waist) with a consequently decreasing of the light intensity. In a HC fiber, the intensity is typically two order of magnitude higher, due to the correspondent smaller MFD. Therefore, the pressure can be lowered (almost) as much as desired because the gas absorption can be compensated with an (almost) indefinite length of the fiber. The drawback is represented by the smaller MFD, which is setting the limits of the technology due to the other broadening effect, the transit-time. It is easy to see from Eq. (3.10) that

with a MFD of few microns, the contribution to the linewidth due to the transit-time broadening is on the MHz level. In case of a fiber with a core diameter of 10 μm filled with acetylene, γ_T is about 20 MHz. The transit-time broadening can be reduced using fiber with larger core diameter [61, 62] or by selecting *slow-molecules* with an appropriate choice of the saturation parameter and gas pressure [33]. Despite the latter case seems desirable due to the narrower linewidth, the lower intensity required to run the experiment in those conditions reduces the overall SNR, since the system is also affected by noise sources other than the laser phase noise, such as electronic noise, mechanical vibrations, etc. Regarding the choice of fibers with bigger core size, the experimental results reported in this thesis aims to demonstrate that is not always true that a fiber with a large core produces a lower instability, as it can be inferred at first sight. In fact, the presence of the HOMs guided in the HC fiber with a large core can be detrimental for the frequency instability of the stabilized laser.

As reported in **Paper I** and **Paper III**, the experimental investigation performed in this thesis are typically run with a fiber length of 3 m and a gas pressure of 30 Pa. These values are chosen after the considerations given so far. Using HC fiber with a core size smaller than 20 μm, the linewidth cannot be narrower than approximately 13 MHz, while the contribution from the pressure broadening at 30 Pa is about 7 MHz. In this condition, lowering the pressure is not significantly a reducing the linewidth and consequently the laser instability. The major effect of a pressure reduction is practical: a lower pressure requires a longer fiber length to keep constant the total absorption. Since the filling time is proportional to the square of the fiber length and the typical filling time for a 3 m fiber at 30 Pa is approximately 25-30 minutes [27], reducing the pressure and consequently increasing the fiber length is not desirable. For these reasons, the pressure and fiber length have been chosen as a compromise to keep both the pressure broadening and the filling time low. Furthermore, a longer fiber requires a longer purging step before filling and the longer filling time exposes the fiber to an higher risk of contamination. As we will see in the following chapters, the main advantage of a longer fiber could be given by the increased HOMs suppression, which might be a solution to reduce the HOMs contribution.

3.3.2 Standard Uncertainty and Reproducibility

In this section, I define two of most useful parameters to evaluate the performance of a stabilized laser: the *standard uncertainty* and *reproducibility*. The (standard) *uncertainty* define the error associated to the optical frequency of the locked laser and it is typically depending on the experimental parameters used. For example, the reference laser used to evaluate the in-fiber laser frequency stabilization performance is a secondary standard realization of the meter [24], stabilized to the optical transiton of $^{13}C_2H_2$ at 1542 nm, following the *mise en pratique* procedure of the BIPM [34]. It has a relative uncertainty of 2.6×10^{-11} at one standard deviation (1σ), which is equivalent to 5 kHz, certified by the BIPM. In other words, the standard uncertainty describes how much the frequency of the laser is expected to vary from setup to setup, at the given experimental parameters.

The *reproducibility* is another useful parameter to verify the goodness of an optical reference. By repeating the experiments several times in slightly different experimental conditions (changing the detector, re-filling the fiber, ...), the lock-point reproducibility measures how reliable is the experiment. It is given by the standard deviation of the repeated lock-point frequencies with respect to the reference. In principle, when two frequency-locked lasers are compared the lock-point fluctuation of both the lasers can affect the reproducibility. Since the reproducibility of the reference laser is on the order of the 10^{-13} [24], the lock-point fluctuations of the reference laser are neglected in the analysis, because they are one order of magnitude lower than the one given by the in-fiber experiments.

3.3.3 Instability: Allan Deviation

The concept of *instability* is the last one that requires to be introduced, in order to quantify how much the frequency of the locked-laser is *drifting* over time. When a similar measurement take place, it requires the presence of at least two oscillators: the *tested* and the *reference* one. By definition, a measure is a comparison between *something* with a *reference*. In order to compare two

oscillator is useful to introduce the concept of *fractional frequency* as

$$y(t) = \frac{\nu(t) - \nu_R}{\nu_R} \tag{3.11}$$

where $\nu(t)$ is the instantaneous frequency response of the *tested* oscillator and ν_R is the frequency of the reference one. A system with frequency fluctuation at a certain timescale τ_1 is considered *unstable* in the range of the fluctuation timescale, but it can be *stable* at a timescale $\tau \gg \tau_1$ or $\tau \ll \tau_1$. One way to measure the instability of a system at different timescale is to calculate the Power Spectral Density (PSD) of the fractional frequency. Instead, in metrology the instability is usually expressed in terms of fractional frequency instability or *Allan deviation*, as a tribute to D.W. Allan who developed this tool for the first time in 1974 [63]. The Allan deviation has been developed specifically to estimate the effect of the random noise frequency modulation on an individual oscillator when compared with other ones. A modified version of the Allan deviation has been introduced by Allan in 1981 [64]. This version is the one usually called *Allan deviation* nowadays. The modified Allan deviation as defined in [64] is used to compute the fractional frequency instability (σ_y) in all the experiments presented in this thesis:

$$\sigma_y^2(n\tau_0) = \frac{1}{2}\left\langle \left[\frac{1}{n}\sum_{i=0}^{n-1} \bar{y}_{i+n} - \bar{y}_i\right]^2 \right\rangle \tag{3.12}$$

where $\bar{y}$ is the averaged fractional frequency time series over τ

$$\bar{y}(t,\tau) = \frac{1}{\tau}\int_0^{\tau} y(t+t_v)\,dt_v \tag{3.13}$$

The Allan deviation gives the chance to calculate the instability at different integration time $\tau = n\tau_0$. The terms *fractional frequency instability* and *Allan deviation* are equivalent. I am not going into the details of the mathematical definition of the Allan deviation and to the sources of instability that can affect its noise spectrum. For the comprehension of this dissertation it is sufficient to underline the connection between the physics behind the SAS experiments and the Allan deviation. We can start defining a frequency source as a sinu-

soidal function like

$$V(t) = (V_0 + \epsilon(t)) \sin(2\pi\nu_0 t + \phi(t)) \tag{3.14}$$

where V_0 is the amplitude (voltage), $\epsilon(t)$ is the amplitude deviation, ν_0 the nominal frequency of the oscillator and $\phi(t)$ the phase deviation [65]. It is easy to see that a phase variation can produce a deviation from the nominal frequency. In fact, the instantaneous frequency of the laser is given by derivative of the total phase

$$\nu(t) - \nu_0 = \frac{1}{2\pi}\frac{d\phi}{dt} \tag{3.15}$$

The upper term of the fractional frequency defined in Eq. (3.11) can be rewritten in terms of the derivative of of the total phase.

3.3.4 Short-Term and Long-Term Instability

In order to easily compare the performance of different SAS experiments in terms of instability at different integration time, two main regions of the *noise* spectrum can be defined: the *short-term* and the *long-term* instability. The typical range of the short-term timescale is given by averaging time (τ) below 10 s, while the long-term one is defined for 100< τ <10000 s. For longer timescale, the lock-point reproducibility gives a more reliable estimate of the stability of the system under testing. In the short-term range, the system instability is limited by the laser phase noise. As previously anticipated, the capability of the frequency locking system to correct the for the laser phase noise depends on the voltage-to-frequency conversion slope of the error-signal, as defined in Eq. (3.9). Therefore in the *short-term* timescale the instability is proportional to the linewidth of the Lamb dip. Fibers that provides narrower linewidth (larger core size) are likely produce lower short-term instability. Another contribution to the short-term noise is likely to be given by polarization instability. In a SAS experiment the polarization of the two counter-propagating beam is affecting the amplitude of the Lamb dip [12]. If the relative polarization of the two beams change over time, the amplitude of the Lamb dip can change, varying the SNR. In the long-term timescale, a number of other effects like

thermal/mechanical drift, gas contamination, power fluctuations etc. can produce a drift of the laser frequency. This distinction has been used in **Paper I** and **Paper III** to easily compare the performance of the different experiments at a different timescale.

Everything went like clockwork.
Preciso come un orologio svizzero

Proverb

4

In-Fiber Laser Frequency Stabilization

In this chapter I report the results obtained with the different fibers tested, which have been already published in **Paper I**. Therefore this chapter is only meant to summarize the results compare them with the state of the art.

4.1 Experimental realization of in-fiber laser frequency stabilization

The detailed description of the testing setup has been published in **Paper I**. The schematic together with a brief summary of the main parameters is reported in Fig. 4.1.1. The SAS scheme is based on two counter propagating

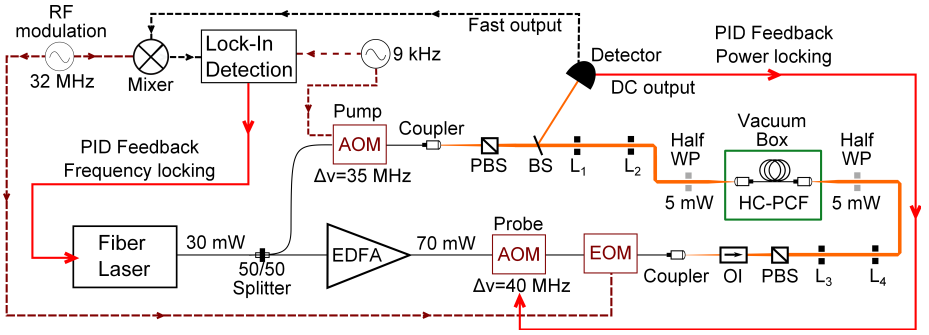

Figure 4.1.1: Reported from **Paper I** with permission. Schematic layout of the SAS Setup. OI: optical isolator. (P)BS: (polarized) beam splitter. L_{1-4}: lenses. Half WP: half wave plate.

beams with the same power (5 mW). The fibers are coiled with an aluminum metal spool of 5 cm diameter and deployed inside a vacuum chamber connected with an acetylene vessel and a turbo pump. The light is coupled via free-space propagation thanks to two anti-reflecting coated windows. The fibers are typically filled with 29 Pa of acetylene after being purged for one week. An Acousto Optic Modulator (AOM) is used to chop the pump light at 9 kHZ and it blue-shifts the optical frequency by 35 MHz. A second AOM is applied on the probe arm to blue-shifts the optical frequency by 40 MHz and it is also used to stabilize the probe power. The optical detuning introduced between the pump and the probe is used to avoid that optical interference between the two counter propagating beams produces a beat not at low frequencies (DC). Other experimental approaches which can be used to reduce the effect of the interference of the two counter-propagating beams are presented in **Paper II**. The light is launched in two orthogonal linearly polarized beams and the , the polarization is controlled with half wave plates. In order to obtained an error-signal for the frequency-locking, the probe is

frequency modulated using an EOM at around 32 MHz. The modulation frequency is manually tuned form time to time, maximizing the slope of the error signal (voltage-to-frequency). For this reason the modulation frequency can be 32 ± 300 kHz , depending on linewidth and on the amplitude of the sub-Doppler feature. Small variation on the modulation frequency can be caused by the different fiber design (core size) and/or small filling pressure difference ($\pm$ 0.5 Pa experimental reproducibility). A Peltier cell is put under the vacuum box to control/manipulate the temperature of the fiber, which is measured with multiple temperature probes at the level of the fiber spool.

4.2 In-fiber laser frequency stabilization performance

As described in **Paper I**, the fibers have been tested in two different environments over three phases: (i) 12 hours in a temperature stabilized, (ii) 12 hours with applied temperature ramp and (iii) about 6 hours back in a temperature stabilized environment. The scope of the first two phases aims to test the temperature dependence of the fractional frequency instability. The third phase (iii) is used to check that no permanent defects have been introduced by the temperature ramp applied in the second phase. All the measurements reported in **Paper I** show comparable performance between the first and third phase. The measurements are also repeated after that each fiber is re-cleaved/re-filled to check the reproducibility of the results, presenting comparable performance. The temperature sensitivity of a HC fiber-based SAS experiment is interesting because temperature variation has already been investigated as a source of phase instability in fiber optic gyroscope (FOG) applications [66]. This phase noise arise from the different thermal expansion between the spool where the fiber is coiled and the glass. The observed instability is stronger if the fiber is birefringent. Since all the tested fibers have a certain level of birefringence due to a non-perfectly circular core section or because of the anti-resonant elements introduced in the core wall (C7_ PM), the experiment is build to evaluate also this parameter. The results are reported and discussed in details in **Paper I** (Fig. 3 to 5) and here I summarize the main points. Considering the overall performances, the C7_S fiber is the most suitable for frequency standard applications, showing a fractional fre-

quency instability below 4×10^{-12}, for averaging time between 1 and 10^4 seconds (almost 3 days), in a stabilized temperature environment. Its remarkable performance in a *stressed* environment ($\sigma(\tau) \leq 8 \times 10^{-12}$), which simulates outdoor temperature variation observable in a random day can be considered as a proof-of-concept of the capability of such a fiber in for remote sensing applications. If compared with the state of the art of the acetylene based optical frequency standard, this test can be considered a significant improvement of the in-fiber technology. Although the performance of the free-space optics vapor cell based standard is practically hard to achieve due to intrinsic limitations of the in-fiber technology (transit-time broadening), the gap with respect to vapor cell based reference laser [24] is reduced and the fractional frequency instability is improved with respect to previously reported HC-fiber based experiments [29]. In Fig. 4.2.1 the comparison with the state of (left) and the lock-point reproducibility (right) of the C7_S fiber is reproduced from **Paper I**. The lock-point reproducibility measured on 6 different days shows that the

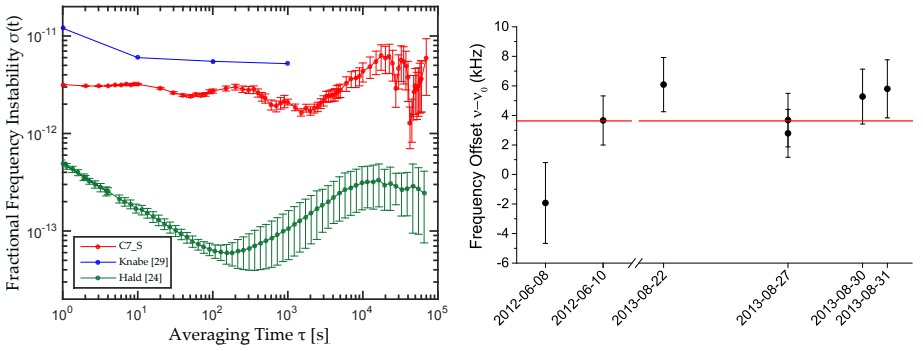

Figure 4.2.1: Reproduced from **Paper I** with permission. Left: Summary of the performance achieved using the C7_ S fiber in a temperature stabilized environment (red). The system is compared with the reference laser [24] stabilized to a bulk glass cell (green) and with the best performance reported with a gas-filled HC-fiber stabilized laser (blue) [29]. Right: The lock-point reproducibility over 7 measurements. The error bars represent the root mean square value of the measured data.

locked frequency is repeatable within 2.5 kHz with respect to the reference laser (1σ). This analysis of the *long-term* fiber performance shows a consistent result over a period of more than 1 year. An important effect observed in the experiment which I have not described is the correlation between the long-term instability and the modal properties of the fibers tested. A detailed

analysis has been reported in **Paper I** and the effect of different spatial modes on the SAS is studied in Chapter 5, where a theoretical explanation and a evaluation of the effect are proposed.

4.2.1 Final Considerations and Future Prospective

A comparison with the previous published results in similar configuration is summarized in Table 4.2.1. It is easy to see that the two experiments are com-

Table 4.2.1: Comparison between previously published results [29] using experimental conditions similar to the one presented here (Fig 4.1.1). The standard uncertainty associated with the experiment presented in this thesis corresponds to the quadrature sum of the reproducibility associated and the uncertainty of the reference laser [24] square-rooted.

Experiment	Uncertainty (1σ)	Instability (1s)	Reproducibility (1σ)
Knabe et al. [61]	2.8×10^{-11}	1.2×10^{-11}	5.9×10^{-11}
Paper I	3.2×10^{-11}	3.1×10^{-12}	1.3×10^{-11}

parable in terms of reproducibility but this study is reducing the instability of the HC fiber-based technology by almost an order of magnitude at 1 s averaging time. Comparing the two studies at different averaging time ($1< \tau < 10^4$ s), the overall instability is reduced by at least a factor 2 over the entire range. A further optimization can contribute to reduce the instability to the 10^{-13} level, in the nearest future. For example, a complete study of the effect of pressure, light intensity and fiber length variation on the SAS spectroscopy parameter is desirable to further reduce the locking instability. Although initially scheduled, I decided to skip this investigation because it would have taken a considerable amount of time which I used to optimize the novel encapsulation approach presented in Chapter 6. A further step on the instability reduction may be achieved with the recently developed ARF fibers [44, 67]. The remarkable results achieved in terms of single modeness in large core HC fiber could be the turning point for bringing the portable optical frequency standard technology to the industrial market.

Once bitten, twice shy.
Sbagliando si impara.

Proverb

5

In-fiber Spectroscopy: novel concept

In this section I aim at presenting a more correct explanation of the effect of different spatial modes on the center frequency response of the locked-laser with respect to the one published in **Paper I**. Although the explanation here provided is more robust, it cannot reproduce the experimental results with good agreement. This model aims to analytically explain the mechanism of the HOMs contribution to the sub-Doppler feature using some approximations, giving a relatively simple explanation of the importance of the single-modeness of the used HC fiber when performing an in-fiber SAS experiment.

5.1 HOMs contribution to the instability

The dependence of the locking-point of the stabilized laser on the the probe coupling condition reported in [29] and the time-varying locked-frequency reported in **Paper I** (Fig. 3) are contributing to point in the direction of the presence of HOMs to explain the frequency shift mechanism. In the last section of **Paper I**, I proposed an explanation for the locking-point oscillations observed in the C7_L fiber, by using the analogy with the angled beam interaction in free space. I introduced such an analogy to account for the effect generated by the different wavevectors associated with different spatial modes (see Eq. (3.2)). Although the idea is *correct*, using the angled-beam interaction analogy is misleading.

In fact, it leads to conclude that a frequency shift of the frequency-locked laser caused by the HOMs contribution can occur also if the two counter-propagating beams have the same optical frequency and this is not the case. This *spatial modulation* of the standing wave can only affect the molecules that have a non-zero velocity component along the light propagation direction $v_z \neq 0$ (i.e. longitudinally along the fiber). In case of two counter-propagating beams with the same optical frequency, the saturation dip comes from the class of molecules with $v_z = 0$ (zero-velocity along the light propagation direction), as explained in Chapter 3. This also happens in case of a pump/probe interaction between two different spatial modes. In fact, the effect I describe here differs from a *real* angled beam interaction configuration [68]. If considering the intensity distribution of modes across the fiber section, a *real* angled beam interaction can also occur inside the HC fiber. The HOMs can have regions of higher intensity on the outer part of the core, while the FM has a typical Gaussian-like intensity distribution: molecules which interact with HOM (with the higher intensity region on the outer part of the core) must have a certain radial velocity component in order to interact with the FM (with the higher intensity in the center of the core). If the two counter propagating beams are detuned, a certain angle between the molecular velocity and the two wavevectors can occur, depending on the ratio between the radial (v_ρ) and longitudinal (v_z) velocity components of the molecules. In this case the interaction is a *real* angle beam interaction and a frequency shifted

sub-Doppler feature can occur. But due to the central symmetry of the spatial modes guided in the HC fiber, accordingly to [68], both positive and negative shifts should occur with equal probability. Therefore, from a geometrical point of view, multiple angled beam interactions should average out the effect, as reported in [29].

The effect that I describe here is not based on the different spatial intensity distribution of the modes. This effect is simply based on the mechanism of the Doppler effect: the frequency shift is generated by the different phase velocity of the light when it propagates in different modes. The mechanism of the Doppler effect in homogeneous medium has been discussed by Papas in [69]. Going into the details of the relativistic Doppler effect is not required for the application described here, but it is important to underline the role of the refractive index of the material. The refractive index of the medium introduce an *aberration* by changing the phase velocity of the light. The key point to understand the effect introduced here is hidden in difference between an homogeneous medium and the HC fiber. In the HC fiber, a monochromatic beam that propagates in different core modes experience a different phase velocity (or propagation constant): this situation is almost unique to the HC fiber and not comparable with a free-space experiment in similar conditions, where the relation between the wavenumber and the optical frequency of the beam is locked. The interaction between two beams launched in two different spatial modes can be seen as light propagating in two different homogeneous medium (with different refractive index) but *occupying* the same space.

In a SAS experiment such a difference leads to a *spatially distorted* standing-wave, whether a pump/probe interaction occurs between two different modes. The spatial distortion is not caused by a *real* optical frequency difference between the two counter-propagating beams but rather by the difference between the *effective* refractive index of the light propagating in two different modes. In fact, accounting for the different effective refractive index of the modes in Eq. (3.1), the effect generated by interaction between different modes become visible. Calling $n_{1,2}$ the effective refractive index of the probe/pump

mode respectively, we obtain

$$\begin{aligned} &-\Delta_1 + n_1 k_1 v_z = -\Delta_2 - n_2 k_2 v_z \Longrightarrow \\ &\quad v_z = \frac{\Delta_1 - \Delta_2}{n_1 k_1 + n_2 k_2} = \frac{(\Delta_1 - \Delta_2)\, c}{(n_1 + n_2)\omega_0 + n_1 \Delta_1 + n_2 \Delta_2} \simeq \frac{(\Delta_1 - \Delta_2)\, c}{(n_1 + n_2)\omega_0} \end{aligned} \tag{5.1}$$

This results can be achieved also by including the different phase velocities of the two counter-propagating beams in Eq. (3.3)

$$\begin{cases} \omega_1^{'} = \omega_1 \left(1 - {}^{v_z}/_{v_{ph_1}}\right) = \omega_1 \left(1 - {}^{v_z n_1}/_{c}\right) \\ \omega_2^{'} = \omega_2 \left(1 + {}^{v_z}/_{v_{ph_2}}\right) = \omega_2 \left(1 + {}^{v_z n_2}/_{c}\right) \end{cases} \tag{5.2}$$

where $v_{ph_{1,2}}$ are the phase velocities of the light in the the probe/pump mode, respectively. If we combine Eq. (5.1) and (5.2), we can calculate the center frequency of the Lamb dip, similarly to what was done in Chapter 3, by substituting v_z into (5.2)

$$\begin{aligned} \omega_2^{'} = \omega_1^{'} &= \frac{\omega_1^{'} + \omega_2^{'}}{2} = \frac{\omega_1}{2}\left(1 - n_1 \frac{v_z}{c}\right) + \frac{\omega_2}{2}\left(1 + n_2 \frac{v_z}{c}\right) = \\ &= \frac{\omega_1 + \omega_2}{2} + \frac{\omega_2 n_2 - \omega_1 n_1}{2}\frac{v_z}{c} = \\ &= \omega_0 + \frac{\Delta_1 + \Delta_2}{2} + \frac{(n_2 - n_1)}{2}\frac{\omega_0 v_z}{c} + \frac{\Delta_2 n_2 - \Delta_1 n_1}{2}\frac{v_z}{c} = \\ &= \omega_0 + \frac{\Delta_1 + \Delta_2}{2} + \frac{(\Delta_1 - \Delta_2)\,(n_2 - n_1)}{2\,(n_1 + n_2)} + \frac{(\Delta_2 n_2 - \Delta_1 n_1)\,(\Delta_1 - \Delta_2)}{2\omega_0\,(n_1 + n_2)} = \\ &\simeq \omega_0 + \frac{\Delta_1 + \Delta_2}{2} + \frac{(\Delta_1 - \Delta_2)\,(n_2 - n_1)}{2\,(n_1 + n_2)} \\ &= \omega_0 + \frac{\Delta_1 + \Delta_2}{2} + \delta \end{aligned} \tag{5.3}$$

The term $\propto \Delta^2$ is neglected as previously but an extra term appears with respect to Eq. (3.4)

$$\delta = \frac{(n_2 - n_1)}{2}\frac{\omega_0}{c} v_z = \frac{(\Delta_1 - \Delta_2)\,(n_2 - n_1)}{2\,(n_1 + n_2)} \tag{5.4}$$

This term is proportional to the frequency detuning between the two beams

($\Delta_1 - \Delta_2$) and on the effective refractive index difference between the two modes ($n_2 - n_1$). In case of probe/pump with the same optical frequency ($\Delta_1 = \Delta_2$), the homogeneously broadened profile is given by molecules with velocity component $v_z = 0 \pm \gamma/2k$ [57, 58]. Differently from what is erroneously stated in **Paper I**, in the absence of detuning between the beams, the extra term is negligible, leading back to Eq. (3.4). In other terms: in the absence of detuning, no effect due to the different spatial modes is expected. The effect of the spatial modes arises if a detuning between the two counter propagating beams is present. If $\Delta_1 \neq \Delta_2$, the last term of Eq. (5.3) can give a non-zero contribution if the pump/probe interaction is occurring between two different spatial modes ($n_1 \neq n_2$). The higher the detuning, the higher is the mean velocity along the light propagation axis of the class of molecules that *see* the same frequency from both the beams. As reported in **Paper III**, the use of two frequency detuned beams is likely to be a common situation in many SAS experiments. In fact, this configuration prevents the optical interference between the two beams that produces noise at low frequency (DC), which is detrimental for the short-term stability of the electronic control loop. From here onward, I will call the interaction occurring between two different modes in a HC fiber a *cross-mode* interaction, meaning that the pump and the probe are not propagating with the same propagation constant.

The analysis presented so far about the Doppler effect in a SAS experiment leads to a simple conclusion: in presence of a frequency detuning between the two beams, the center frequency of the Lamb dip in the molecular reference frame is *not* equal to the average of the two optical frequencies measured in the reference frame of the laboratory. This fact is valid in general, not only in a HC fiber experiments, as demonstrated in Eq. (5.3), by considering the neglected term $\propto \Delta^2$. In case of a free-space SAS experiment at 1542 nm, the term $\propto \Delta^2$ would be on the order of 10 mHz, requiring a fractional frequency instability around 1 mHz ($\approx 5 \times 10^{-17}$) to be resolved. This shift is an intrinsic consequence of the nature of the Doppler effect, which depends on the phase-velocity of interacting beams, but is negligible in a free-space experiment. The situation changes in an HC fiber, due to the light propagation constrains introduced by the fiber itself. Despite the guidance in air, the light propagation in a HC fiber is far from the free-space one. The contribution given by the different spatial modes produces a frequency shift that can be *detected* with the

typical sensitivity achievable in the typical HC fiber based SAS experiments nowadays. In fact, the *shift* depends both on the detuning and on the spatial modes considered. Typically, in a HC fibers the effective refractive index difference between the FM and one of the first HOMs is on the order of 10^{-2} and the frequency can vary between 1 and 50 MHz. Therefore the cross-mode interaction can potentially produce shifts of the frequency-locked laser at the kHz level. Depending on (i) the number of modes excited, (ii) the intensity associated with the different modes and (iii) the detuning between the beams, the result can vary significantly. The scope of this section was to show how molecules that interact with two different spatial modes in a SAS experiments can produce a shift of the sub-Doppler feature detected. In the following sections I introduce a method to account the different parameters involved in this mechanism, in order to quantify the effect in a real experiment. Serving the scope of simplifying the calculation, the approach is applied to the case of the C7_L fiber and a comparison with the oscillation reported in the **Paper I** is provided.

5.2 Superposition principle: a simple weighting method

Using the novel concepts introduced so far, when a SAS experiments is done in a HC fiber, a superposition of many cross-mode interactions should be taken into account in order to correctly predict the center of the sub-Doppler feature. Similarly to what is presented in **Paper I**, thanks to the orthogonality of the different spatial modes, we can describe each beam with a superposition of the spatial modes guided by the fiber. In first approximation, the detected sub-Doppler feature detected can be seen as the a superposition of multiple pump/probe interactions that occurs between different spatial modes

$$I_{tot} = \sum_{i=1}^{n} \sum_{j=1}^{m} I_i \mathrm{e}^{-\alpha_{ij}(\omega,S,L,P)} \tag{5.5}$$

where α_{ij} is the absorption profile of the interaction between the i-th spatial component of the probe with the j-th spatial component of the pump and I_i is the intensity associated the i-th spatial component of the probe. In the SAS configuration, the probe beam is used to generate the locking signal, there-

fore the total intensity detected depends on the absorption profile at a given interaction and on the loss of the optical mode caused by the fiber. In general, multiple spatial components of the pump can contribute to the optical pumping of the same class of molecules. In order to reduce the number of possible cases, I limit the analysis to the case of molecules to the case of molecules optically pumped by a single spatial component. This is equivalent to assume that the pump beam is in only in the FM. This assumption is *required* to used the absorption α_{ij} as defined in Eq. (3.5) and (3.7): these definitions represent (i) a configuration where both the beam as equal intensities (Eq. (3.5)) and (ii) where the probe beam is weaker than than the pump (Eq. (3.7)), respectively. In general, the validity of Eq. (3.7) when a weak pump and a strong probe beam are counter propagating is not obvious and the absorption profile may vary significantly. Therefore, the case of the pump in a HOM component interacting with the probe in the FM is not considered in this analysis.

Therefore, under the assumption that the saturation is given only by the (strong) pump beam and assuming that different spatial components do not contribute to the saturation of the same molecular class, each interaction can be evaluated separately and summed together. Since each interaction depends on the intensity associated with the spatial modes considered, it is required to know the power distribution of the light among the guided modes. Depending on the number of modes guided by the HC fiber, the evaluation of Eq. (5.5) can still be complicated, therefore some approximations are required to stick to an analytic solution. The *weighting method* I propose here does not aim to give an *accurate* evaluation of the effect of the different cross-mode interaction. A more reliable result can potentially be achieved only with numerical solution of the density matrix equations [57] of a similar experiment, taking into account of the saturation parameters and the wavenumbers associated with all the guided modes. However, the following approach is meant to be a simple way to establish if the effect of the spatial distortion caused by the different modes can be detected in real SAS experiments. Moreover, it can provide some practical indications about the fiber behavior before running the experiment. The ultimate goal is to reduce the experimental investigation on fibers which are likely to produce high instability.

5.3 C7_ L Fiber: a particular case

Since the primary goal is to evaluate if the frequency oscillation of the locking point reported in **Paper I** can be ascribed to the HOMs as presented so far, it is beneficial to directly apply the calculation to a particular case. The structural features of the C7_L indicates that the fiber is a good candidate to test the simplified approach I propose. Despite the apparent multi-mode performance, the fiber could be considered as a *two*-mode fiber, where only one of the HOMs has limited loss to reasonably affect the light-matter interaction (black dots, Fig. 5.3.1). Using the information reported in 5.3.1, we can con-

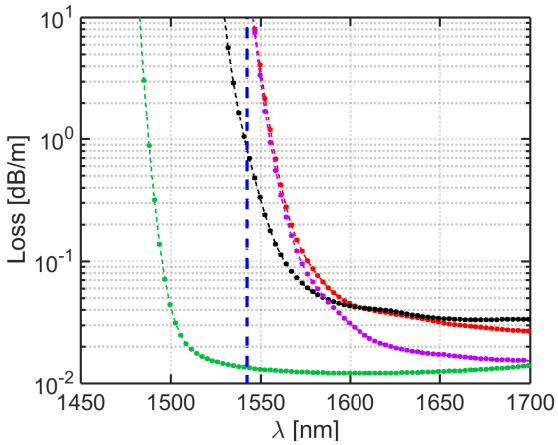

Figure 5.3.1: Figure reported from **Paper I** with permission. Simulation results of C7_L: three HOMs (red, violet and black dots) and a surface mode (blue) are highlighted. A dashed blue line at 1542 nm is added.

sider that the loss of the FM is negligible and the power launched into the HOM considered is halved along the fiber (1dB/m, 50% transmission along the 3 m of the fiber).

5.3.1 The Intensity Distribution

As previously mentioned, this approach require to know the *power* coupled to the different spatial components, in order to define the absorption profile of the given pump-probe interaction (α_{ij}) and the average intensity associated

with the different spatial components of the probe (I_i). In the following section, the concepts of *power* and *intensity* of the light associated with a single spatial mode in the HC fiber are equally used and the difference in the spatial distribution of the modes inside the core is neglected. In general, all the core modes are going to be distinguished only by the different propagation constant (or wavevector) associated. Differently from what is reported in **Paper I**, here I propose a more robust way to calculate the intensity associated with the different spatial components, using some simple experimental considerations on the fiber transmission properties.

The experimental transmission coefficient ϵ of the *empty* HC fiber depends on the overlap integral between the launched mode and the linear combination of the guided modes in the HC fiber and on their optical loss associated. Knowing the relative intensity and the total loss associated with the modes, it is possible to calculate the total optical transmission along the HC fiber using the Beer-Lambert's law

$$\epsilon = \sum_{i=0}^{n} \xi_i \exp\left[-\phi_i L\right] \tag{5.6}$$

with L the fiber length and ϕ_i $[m^{-1}]$ is the loss associated with i-th mode. ξ_i represents the relative intensity launched to i-th spatial mode. In an optimal coupling conditions, the light coupled to the core modes of an HC fiber should theoretically vary between 90% and 95%, depending on the core size and on the fiber properties. Experimentally, the typical coupling efficiency can vary between 60% and 75%, as reported in **Paper I** and in [29, 62]. The experimental transmission coefficient of the C7_L fiber is $\epsilon = 0.67$ (Table 2.2.1). The discrepancy between theory and experiments can be ascribed to a mode-mismatch of the in-coupling beam due to angle/lateral misalignment or to a non-optimal combination of coupling lenses. Using the results of the simulation performed on the C7_L fiber, we can calculate the maximum theoretical overlap integral between a Gaussian mode and the linear combination of the modes guided by the fiber. Due to the higher loss of the considered HOM ($\simeq$0.8 dB/m, $\phi_{\mathrm{HOM}} \simeq$0.184) with respect to the FM mode ($\simeq$0.02 dB/m, $\phi_{\mathrm{FM}} \simeq$0.005) reported in Fig. 5.3.1, the higher optical transmission ($\simeq$90%) is achieved when the majority of the light is coupled to the fundamental mode. By using Eq. (5.6), it is possible to calculate which combination of the relative

intensities associated with the guided modes that matches the experimental transmission coefficient ($\epsilon = 0.67$).

It is easy to understand that in general hundreds of different intensity distribution over the modes can reproduce the experimental value. This is due to the fact that the power that is *escaping* the core (coupling through surface modes and/or cladding modes) is unknown. Altogether, in order to roughly quantify the effect of the HOMs in the SAS experiments we are interested only to determine the extreme scenarios which can explain the experimental transmission coefficient of 67%. In the particular case considered, the most representative ones are occurring when

a) No light is launched into the HOM. 67% of the light is launched into the FM mode and the remaining is decoupled from the core and/or launched into HOMs with high loss.

b) 50% of the light is launched into the FM ($\xi_{\mathrm{FM}} = 0.50$), 34% of the light is launched into the considered HOM ($\xi_{\mathrm{HOM}} = 0.34$) and the remaining is decoupled from the core.

These cases are useful to draw some boundaries to the possible amount of light coupled to the HOM, although the most probable scenario is likely to occur in a configuration in between them.

Despite the limited amount of information, it si possible to estimate the effect of a two-mode interaction in the C7_L fiber by using these two extreme cases. It's easy to understand that in configuration **b)** the effect will be maximum while no shift will occur in configuration **a)**. Any scenario in between will produce a reduced effect with respect to **b)**. The two configurations are represented in Fig. 5.3.2. The power/intensity associated with the two modes needs to be calculated using the Beer-Lambert's Law

$$I_i = I_0 \xi_i \mathrm{e}^{-\phi_i L} \tag{5.7}$$

where I_i is the power associated with the mode considered at the fiber output, ξ_i is the relative power launched in the i-th mode and ϕ_i is its propagation loss. From now on, $i = 1, 2$ refers to the FM and to the HOM components of the probe, while $i = 3$ refers to the pump in the FM, accordingly to the

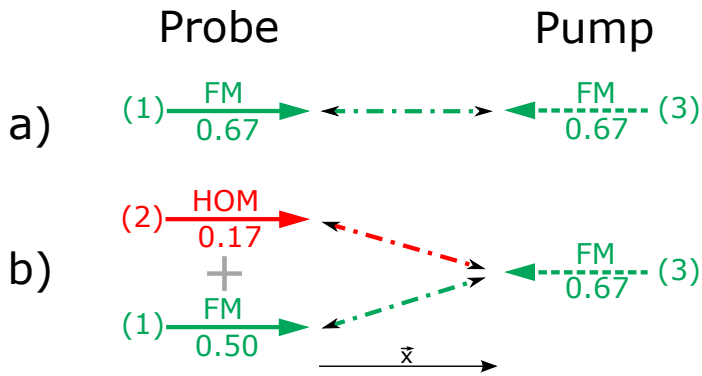

Figure 5.3.2: Schematic representation of the pump-probe interaction in a single mode to single mode **a)** or in a *multi*-mode to single mode interaction **b)** in the HC fiber. The values under the spatial components represents the relative intensity associated with the modes, calculated using Eq. (5.7).

notation represented in Fig 5.3.2. I_0 represents the total power launched at the fiber facet, which is equal to 5 mW in the case considered. Using Eq. (5.7) the power associated with the FM and the HOM of the probe is calculated in $I_{\mathrm{FM}} = 0.5I_0$ and $I_2 = 0.17I_0$, respectively. Now we have all the elements for estimating the theoretical effect of the superposition of a FM-FM interaction and the FM-HOM (configuration **b)**). Since the pump is considered in the FM for simplicity, by using Eq. (3.5) for the FM-FM interaction and Eq. (3.7) for the FM-HOM one, it is possible to calculate the absorption profile in the two cases, accounting for the lower level of saturation induced by the FM-HOM interaction with respect to the FM-FM one.

5.3.2 The Saturation Parameter and the Lamb Dip Shift

In order to use Eq. (3.5) and (3.7) it is required to calculate the saturation parameter. In both the cases, we use the approximations that the intensity of the HOM is much smaller than the pump one ($I_2 \ll I_3$) and that the intensity of the FM of the probe is equal to the pump one in both the configurations ($I_1 \approx I_3$). The pump intensity is only a factor of 4 greater than the HOM one, however this approximation facilitates the calculation. Since the saturation power of a similar in-fiber SAS with acetylene has been measured to be

approximately 23 mW [27], the saturation parameter can be calculated by

$$S = \frac{I_3}{I_{\text{SAT}}} = 0.67\frac{I_0}{I_{\text{SAT}}} \tag{5.8}$$

where I_3 is the average intensity of the pump beam, I_0 =5 mW and I_{SAT} =23 mW. The last element is given by the expected shift generated by a *pure* HOM-FM interaction on the Lamb dip in the C7_L experiment. Using Eq. (5.4) we obtain a theoretical shift of the center wavelength of

$$\delta_{\text{C7\_L}} = \frac{(\Delta_{\text{PROBE}} - \Delta_{\text{PUMP}})\,(n_{\text{PUMP}} - n_{\text{PROBE}})}{2\,(n_{\text{PROBE}} + n_{\text{PUMP}})} = +8.8kHz \tag{5.9}$$

since the detuning is 5 MHz (Δ_{PROBE} =40 MHz, Δ_{PUMP} =35 MHz) and the effective refractive index difference is 0.007 (n_{PROBE} =0.9875, n_{PUMP} =0.9945). Now, Eq. (3.5) can be used for the FM-FM interaction in both the configurations, while Eq. (3.7) can be used for the HOM-FM interaction of configuration **b)**. In both cases, Eq. (3.5) and Eq. (3.7) need to be rewritten introducing ω_0' instead of ω_0, where

$$\begin{aligned} \text{FM-FM interaction:} \;\rightarrow\; \omega_0' &= \omega_0 + \frac{(\Delta_{\text{PROBE}} + \Delta_{\text{PUMP}})}{2}; \\ \text{HOM-FM interaction:} \;\rightarrow\; \omega_0' &= \omega_0 + \frac{(\Delta_{\text{PROBE}} + \Delta_{\text{PUMP}})}{2} + \delta_{\text{C7\_L}}; \end{aligned} \tag{5.10}$$

where $\delta_{\text{C7\_L}}$ is calculated from Eq. (5.9). Is is possible to evaluate the absorption profile and the error-signal used for locking in both the configurations using Eq. (5.5), as represented in in Figure 5.3.3. It is easy to understand that the center of the sub-Doppler peak in configuration **b)** will be blue-shifted by some kHz, due to the superposition of the HOM-FM and the FM-FM interaction. A numerical analysis shows that shift is expected to be around 3 kHz. Therefore, this calculation can predict frequency shift of the maximum of the Lamb dip up to 3 kHz, if the system is varying from configuration **a)** to **b)**. Experimentally the effect is measured to be approximately one order of magnitude greater, with a shift up to 25 kHz (see Fig. 3, **Paper I**). Despite the limitations of the proposed method, some important considerations can be done, also related to the previously published results in [29] and in **Paper I**.

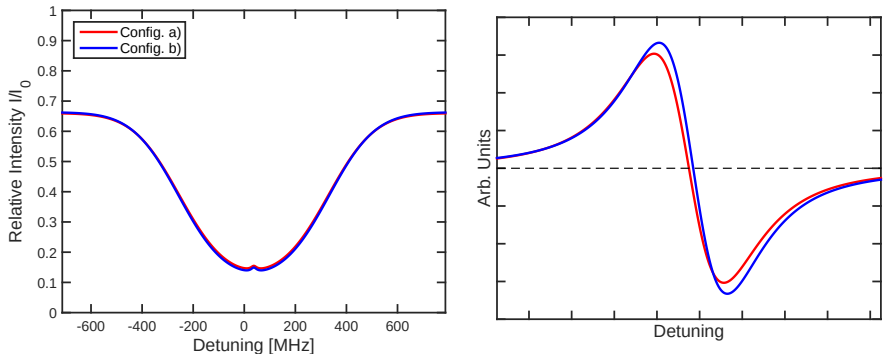

Figure 5.3.3: Absorption profile (left) and associated error-signal (right) as simulated with the method proposed. The shift between the two error-signals has been enhanced to be clearly visible *by eye*.

5.3.3 Final Considerations

The limitations of the theoretical approach I proposed here can be ascribed to the simplified analysis, as previously mentioned. This analysis is not taking into account eventual HOM components of the pump, which are reasonable to expect. Their presence can contribute to explain the *negative* shifts of the Lamb dip center frequency measured in **Paper I**, although the calculation might be more complicated using the method proposed. If the interaction occurs between the pump light in the HOM and the probe in the FM, the configuration is the opposite with respect to **b)**: the probe intensity will be higher than the pump one and the absorption profile might differs significantly from Eq. (3.5) and/or (3.7). In the approximation that the absorption profile does not vary a lot, this configuration will be the *opposite* of the HOM-FM interaction represented in configuration **b)**. In fact, in this case the *pure* HOM-FM will give a symmetric shift of -8.8 kHz with respect to **b)**, while the *real* effect might be around -3 kHz or lower/higher due to the different absorption profile.

Other causes might contribute to enhance the effect observed on the laser-locked frequency, such as some residual shift caused by the *real* angled-beam interaction previously mentioned in [29] or the contribution given by the polarization, which has not been taken into account so far. The role of the surface modes and/or the scattering loss caused by the core-wall roughness is important in the mechanism of energy exchange between the core modes. While

the core modes are orthogonal (not exchanging energy), the surface roughness and the initial coupling condition can contribute to pump light into the surface modes. This mechanism is one of those responsible for the power *leak* of the HC fiber, but it is not to be excluded that it can pump back light into the core modes. In a simple mental experiment using a ray-picture total internal reflection guidance mechanism, the angle of incidence of the light with the interface is determined by the mode in which the light is propagating. In case of a *rough* interface, the angle of incidence changes *locally* with the roughness. In the HC fiber, the light scattered by surface roughness makes of the core-wall can be coupled to other spatial components and/or leak out from the core, producing an higher fiber loss. Measure the surface roughness of the core-wall is extremely difficult, and despite few attempts and the availability of the AFM, I did not manage to measure the core-wall roughness in a reliable and useful manner. This explanation is left as a simple consideration shared with the fiber manufacturer and which might be evaluated in the nearest future.

Altogether, what is important to underline is that the proposed approach can be valuable to set some boundaries on the HC capabilities and give an important suggestion for the experimental setup design, without requiring more robust and complicated calculations. The key-point is determined by Eq. (5.4). The HOMs can generate a shift which is directly proportional to the effective refractive index difference and to the detuning between the two beams, as a direct consequence of Doppler effect. The *distortion* caused by the effective refractive index difference is enhanced by the velocity component along the fiber of the molecular class that mainly contribute to the signal: the higher the velocity (which is proportional to the detuning), the greater will be the effect of the distortion. This interpretation is compatible with the difference in frequency shift reported in [29] and in **Paper I**. In [29] the maximum frequency shift observed (caused by a misaligned beam coupling) is around 100 kHz, where a kagome fiber with about 68 μm core diameter and a detuning $\sim$ 55 MHz is used. Without considering that the larger core of the kagome fiber guides an higher number of HOMs with respect to the C7_L fiber, it is possible to forecast a frequency shift of about $\sim$ 30 kHZ in similar experimental conditions. In Table 5.3.1 the comparison is summarized. The only consideration used to predict the shifts in an experimental condition similar to [29] is

Table 5.3.1: Comparison between experimental results and model prediction prediction. *Detuning*: detuning between the pump and the probe beam. *FM-HOM*: shift given by a *pure* FM-HOM interaction, as defined in Eq. (5.4). *Predicted*: predicted effect in a configuration similar to config. **b)** (Fig. 5.3.2). *Experim.*: effect reported in literature.

Experiment	Detuning [MHz]	FM-HOM [kHz]	Predicted [kHz]	Experim. [kHz]
Paper I	5	8.8	2.9	25
Knabe et al. [61]	55	96.8	31.9	100

that the frequency shift scales with the detuning (Eq. (5.4)). In general, different optical intensity due to different power/core size or different effective refractive index difference ($n_{\mathrm{PUMP}} - n_{\mathrm{PUMP}}$) can vary the forecast.

Therefore, despite the presence of the detuning is important to avoid the interference between the counter-propagating beams increases the noise at DC level frequency, this value should be also kept as low as possible to mitigate the HOMs effect. From the experimental point of view, while a detuning above 1-2 MHz is desireable to avoid the effect caused by the interference, keeping it below 5-10 MHz is also desirable to avoid the possible contribution of the HOMs, especially if a multi-mode HC fiber is used, such as the kagome reported in [29] or the C19 fiber reported in **Paper I**.

The last consideration is about the reliability of the frequency reference that can be achieved with different HC fiber. Despite large core HC fibers can potentially give a linewidth (FWHM) of the sub-Doppler feature below 10 MHz [29], reducing the short-term instability, the single-mode property is more important for the realization of a reliable stand-alone optical frequency reference: a small drift in the coupling condition or thermal/mechanical stress (as reported in **Paper I**) will be detrimental for the frequency stability of the locked-laser if the fiber guides more than one mode. This consideration can be applied also to the polarization in HC fibers with a high birefringence, as reported in **Paper I**: in a birefringent HC fiber the *slow* and *fast* axis guides *two* orthogonal linearly polarized modes with different propagation constants. But although they are both in the *FM* configuration, they are effectively two *different* spatial components, due to the effective refractive index difference. Therefore, they can produce a frequency shift similar to the one given by the

HOMs. In conclusion, by using this simplified approach, I was able to identify the reasons that caused the instability in the multi-mode/PM HC fibers and the coupling sensitivity of the locking frequency reported in **Paper I** and in [29].

5.3.4 Future Prospective

Following this analysis, reducing the detuning between the two counter-propagating beams can be extremely important in order to limit the effect of any HOM on the locking stability. The fact that a simple calculation shows that the effect should *visible* at the kHz level is confirming that the HOM are at least partially responsible of the instability observed. But it is important to clarify that, despite the effect described so far is the result of the nature of the Doppler effect, the fact this is the major mechanism responsible of the shift reported in this thesis still needs to be proved. In order to validate this analysis, a simple experiment can be set: using a setup similar to the one reported in Figure 4.1.1, once the coupling condition of the pump/probe is optimized, a controlled misalignment on the probe can be introduced. This action should produce a shift of the locked-frequency, as reported in **Paper I** and in [29]. In this configuration, the light will be naturally launched in a (random) linear combination of the modes guided by the HC fiber. At this point, by changing the detuning between pump and the probe frequency, a variation on the locking frequency should be observed. If a measurement of the effective spatial modes content of HC fiber output is performed in parallel, using for example the S^2 imaging technique [70], the correlation between the guided spatial components, their intensities and the shifts produced could be understood more deeply. The suggestion could be to start with a fiber that guides a limited number of HOMs, like the C7_L fiber considered in this evaluation, to limit the number of possible cross-mode interactions that need to be identified.

So close yet so far.
Cosí vicino eppure ancora cosí lontano.

Proverb

6

Fiber Encapsulation and Stand-Alone Frequency Standard

In this Chapter I present the stand-alone optical frequency standard developed using the best HC-PCF tested. The main results have already been published in **Paper III**, but some details about fabrication of the novel encapsulation method has been omitted. The development of a suitable sealing method for a compact and efficient encapsulation of the fiber was one of the major task of my Ph.D. study. In order to give a flavor of the workload I did to complete this task, this chapter includes a brief description of the 3-D printed tool I developed to improve the sealing tightness and the optical properties of the encapsulation. Therefore the fabrication process and the dedicated tools developed to achieve the wanted performance are the major topics covered in this chapter.

6.1 State of the art encapsulation technology

Developing a reliable encapsulation for the HC fiber is one of the major challenge of the HC fiber based optical frequency standard. In order to comply with the requests of a potential market, the system needs to combine high optical and sealing properties in a compact design. The best solution for a *fully* fiber based system would be to splice both the end of the HC fiber to a SM step-index fiber [26, 35, 38]. Although this approach is desirable for its compactness, obtaining a tight sealing and a low coupling loss is not free of challenges. The mode of the two fibers needs to match in order to have an high coupling efficiency, limiting the use of fibers with large core size. If large core HC fibers are meant to be used, a dedicated tapering/collapsing of the cladding structure could be required to increase the mode matching. Or a step-index MM fiber needs to be implemented, with all the consequence described in Chapter 5. Additionally, an angled splice is desired to limit back-reflections from the facet of the solid core fiber: the two spliced interfaces could act as *imperfect* mirrors, generating an unwanted Fabry-Perot *cavity* [39]. The etalon effect generated leads to the so-called *baseline variations*: a variable transmission efficiency strongly depending on the optical frequency launched in the fiber [37] This effect (if not actively controlled) is detrimental for the frequency stability of the locked laser, since the zero-crossing point of error-signal used for locking depends on the overall transmission coefficient.

As widely described in **Paper III**, the splicing technique requires a dedicated fiber filling method [37], which involves a mixture of acetylene and high pressure inert gasses that can diffuse through the glass structure after filling. These considerations arose the necessity to look for other solutions. In **Paper III**, I presented a novel encapsulation technique for the HC fibers which aims to overcome some of the technical difficulties reported by the state of the art techniques.

6.2 From the First Attempt to the Final Design

The proposed encapsulation is an evolution of a previous design tested at DFM before the beginning of my Ph.D. study. To simplify the description,

from now one the encapsulation of the HC is called simply *cell*. The previous cell design is visible in Fig. 6.2.1

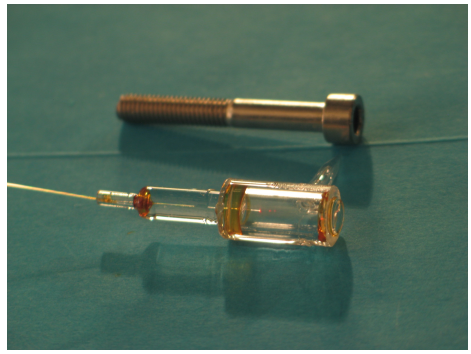

Figure 6.2.1: Previous encapsulation design

Two capillaries of different Outer Diameter (OD) have been used and the assembly requires three steps: (i) one capillary with Internal Diameter (ID) of 127 μm is used to glue the bare HC fiber in place, while (ii) a second capillary with ID that match the OD of the first one is used to glue an aspheric lens used for coupling. This second capillary is provided with a lateral glass tube to the have access to the fiber core after the assembly. In this manner, the lens and fiber gluing occurs in two separate steps. Finally, (iii) the two capillaries are inserted one in to the other and the relative position of the two is adjusted to optimize the coupling between an incoming collimated free-space beam and the HC fiber. A short capillary is used on one back part of the first capillary is used to increase the mechanical resistance of the glued bare fiber. The glue is a double components space-compatible epoxy glue, with low outgassing properties (EPO-TEK® 383ND). The lateral tube attached to the external capillary allows to purge, fill with acetylene and seal the fiber using the same procedure reported in **Paper III**.

Monitoring the linewidth of the sub-Doppler feature of the system over time, the pressure stability observed was not considered satisfactory. The pressure broadening initially observed was ascribed to a design limitation, due to the tolerances of the ID and OD of the two nested capillaries. Therefore, it has been decided to apply a silicone-based vacuum sealant (VacSeal®) on the ex-

posed epoxy layer. Immediately after the application, the linewidth increased significantly, with a rate of few MHz per day. A subsequent thermal curing step of several hours above 70°C did not stop the pressure broadening, suggesting that the uncured VacSeal was diffusing through the epoxy, producing unwanted outgassing in the cell. A second thermal curing step combined with purging step applied to the cells (similarly to what reported in **Paper III**) significantly reduced the pressure broadening observed. With these experimental observations, I started to work on the first evolution of the cell design.

6.2.1 First Evolution and Final Design

From the described prototype, I modified the design to produce a more compact and easy-to-fabricate cell. The design was similar to the one published in **Paper III**, except for ID of the capillary tube, which was 127 μm. In fact, the system was initially designed to inject the bare fiber into the capillary: this characteristic has been maintained from the first prototype in order to avoid any possible outgassing of the fiber coating exposed inside the cell. The drawback was represented by the necessity of having a supporting sleeve at the end of the capillary tube, similarly to what is shown in Fig. 6.2.1. This approach can easily end at having a significant portion of bare fiber sticking out from the cell, unsupported. After a couple of failed assembly attempts, due this mechanical weakness, I decided to move to the designed proposed in **Paper III**, where the ID of the capillary is chosen to injected the fiber without stripping the coating. This solution has significant impact in the mechanical stability of the sealed fiber and no mechanical failure has been encountered in all the fabricated. This cell has not been used only to produce the optical frequency references with $^{13}C_2H_2$ (**Paper III**) and CO_2 (**Paper V**), but it has been successfully used in a high-resolution Raman spectroscopy experiment [71], demonstrating the versatility and reliability of the encapsulation developed. Now, I present the full fabrication process, including some of the technical details omitted in **Paper III**. The fabrication steps are briefly reported in Fig. 6.3.1 to improve the readability, but the attention will be focused only on those steps that require additional details with respect to the published recipe.

6.3 The novel approach: fabrication

The schematic fabrication process is reported in Fig. 6.3.1. The entire fabrication process can be summarized in two different phases: the first three steps (A-C) are used to *fabricate* the cell, while in the last three (D-F) the system is *assembled*.

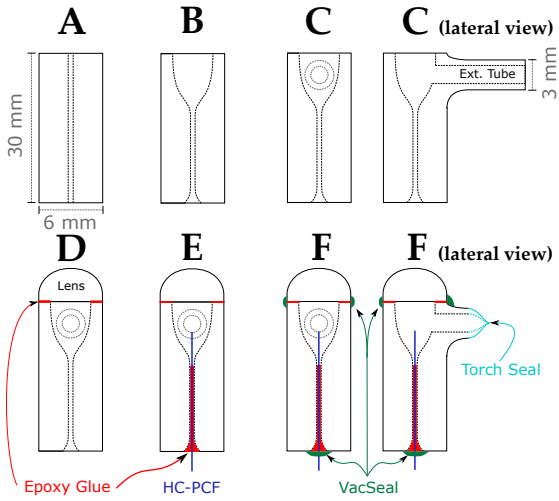

Figure 6.3.1: Reported from **Paper III** with permission. Schematic of the novel encapsulation technique. (A) capillary selection. (B-C) capillary modification to include a small *chamber*. (D) lens gluing. (E) Fiber injection and gluing. (F) Filling and final sealing.

6.3.1 Steps A to C: Cell Fabrication

The first three steps are widely described in **Paper III** and they are fairly easy to complete. The size of the capillary will depends on the OD of the fiber, which si typically in the range of 220-240 μm for standard HC fibers. The ID of the capillary does not require to fit the fiber OD: a gap of 20 to 30 μ will not create any issue on the fiber sealing. The glue will fill up the gap along the capillary during the gluing step, drag by capillary forces. Since the glass is annealed to be processed, a possible failure mechanism is caused by the partial collapsing of the capillary, which could prevent the fiber to be injected

in the cell. A preliminary check of the clearance of all the capillaries made with a dummy fiber is required to scrap the failed cells. The yield of success of this first phase is above 95%, despite the process is done manually by a technician.

6.3.2 Step D: Lapping Tool

One of the most delicate task is represented by the lapping of the front facet of the cell. After the annealing, the cell comes with an irregular surface which is not ideal for the lens to be glued. The lens require to be placed centered on the capillary and with the focal plane orthogonal to the axis of the capillary. A correct gluing of the lens is extremely important to have the best coupling condition for the HC fiber. The front facet of the cell needs to be polished to optical finish: the presence of scratches leads to a compromised sealing. For these reasons, after several attempts failed in the lapping and/or the gluing step, I designed a dedicated tool that helps to overcome all the encountered technical issues. The tool has been 3-D printed of Polylactic acid (PLA) and

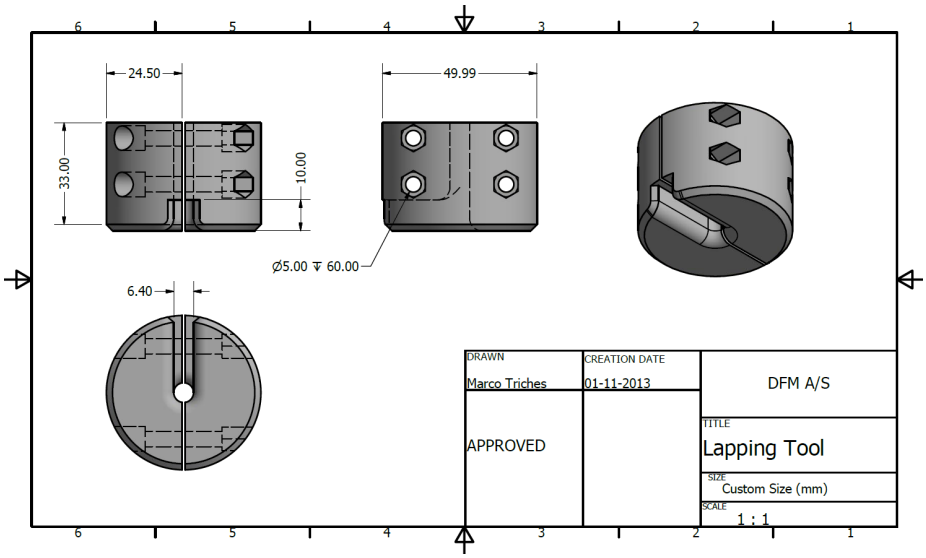

Figure 6.3.2: Lapping tool designed for 3D printing

is made of two solid hemi-cylinder used to clamp the cell, as represented in

Fig. 6.3.2. The clamping is provided by four screws and the tool is designed to hold the bolts in place for an easy handling. The polishing film used is the one suggested by Thorlabs for polishing the ceramic fiber connectors: a diamond-dust based polishing film, in different grit size, from 30 down to 0.02 μm grit. Once the cell is clamped, the facet is polished using a finer grit after each polishing cycle. The polishing method is also the same used for the fiber connectors: dropping distilled water on to the sheet and polish the facet in a *figure-eight* motion.

Differently from the fiber connectors, the surface needs to be flushed with a considerable amount of water, especially with the coarser grit because the amount of glass dust is considerably higher. For this reason, other lapping film types like aluminum-oxide or silicon-carbide are not recommended: these films degrade too fast an particle with size bigger than 30 μm are likely to be ripped apart during the process and they could scratch the cell facet, forcing to restart the entire lapping cycle. The cell facet is checked before changing paper grit size, using a 10x ocular magnifier and looking at the light reflected by the cell facet under a lamp: if the surface roughness is uniform, the scratches done by the greater grit has been removed and the finer grit can be chosen. After the last polishing step, the cell facet should look like a *silver mirror* if it is observed using the magnifier at the Brewster angle condition. The entire process takes around 30 minutes per cell, but the time required can increase up to one hour if the facet surface is scratched in one of the polishing steps. After cleaning the cell with 15 min of ultrasonic bath in distilled water, the cell facet can be checked using a polished quartz substrate. Posing the quartz on the facet surface and applying a soft share force would make the cell sticks to the quartz: if a negligible presence of Newton's ring is observed, the facet can be considered flat and polished to *optical finish*. The presence of a single scratch will prevent the adhesion of the two glass substrates, giving a clear indication that the lapping procedure needs to be repeated. Typically, this extra test is not required: from the experience acquired during my Ph.D., checking the facet with 10x magnifier is enough to clear the presence of any major scratch that would compromise the following steps.

6.3.3 Step D: Glue the Lens

The advantages given by the developed lapping tool are also clear in the second part of step D: the tool can be used as holder for the cell, as shown in Fig. 6.3.3 (left). The tool holds the cell in place with the capillary orthogonal

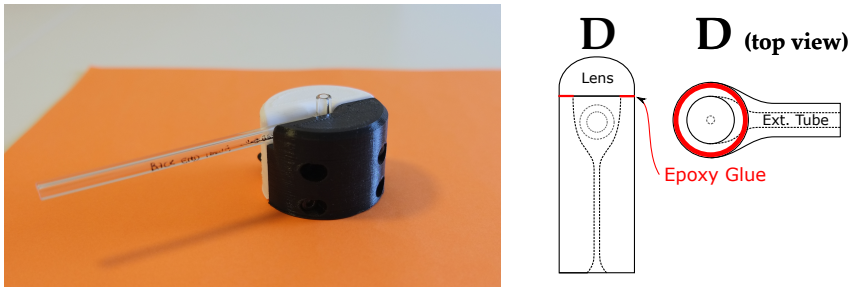

Figure 6.3.3: Left: 3-D printed lapping tool used to hold the ferrule before gluing the lens. Right: how to deploy the glue in order have a good adhesion avoiding to damage the lens and the optical properties of the cell.

to the table and the facet facing up. This situation makes easy to apply the glue that comes in a syringe. After various attempts, I found that the best way is to apply the glue only on external part of the face, as represented in Fig. 6.3.3 on the right. This helps to reduce the amount of glue applied to the facet and it is limiting the possible floating of the lens during the thermal curing step. In fact, if the glue is applied over the entire surface, once the lens is deployed it is likely to happened that glue adheres also to the central part of the lens, reducing the clearance of the lens. Moreover, with this approach the lens is likely to float during the curing step due to the reduced viscosity of the glue at high temperature. The initial attempts when the glue has been applied on the entire facet shows a yield lower than 50% due to these problems, while the current procedure has a yield above 90%. This improvement can be partially ascribed also to the improved skills I acquired all along the Ph.D. study on this procedure.

The glue requires a thermal treatment of 150°C for about 1 hour or a dynamic cure of 25-30 minutes 20-200 °C with a ramp of 5-6°C/min. The first attempts using one of these recipes have caused several failures. The main reason is due to the floating of the lens mentioned above due to a too fast cure. My

experience suggests that it is better to split the cure in multiple steps with a progressive increasing temperature. Staring with low temperature cure step for longer time allows the glue to harden slowly, avoiding the floating of the lens. A subsequent cure at high temperature is completing the cure without affecting the position of the lens. The suggested procedure is made of the 5 steps with the temperature/time parameters reported in Table 6.3.1. The cure

Table 6.3.1: Lens curing procedure: step 1 to 5

	# 1	# 2	# 3	# 4	# 5
Temperature	< 40 °C	70 °C	90 °C	110 °C	150 °C
Time	> 10 hrs	3 hrs	3 hrs	1 hr	30 min

proposed is chosen due to the successful experimental evidence and because 100 °C is the glass transition temperature of the glue. Alternatively, instead of the steps 1-3, a single step of 24 hours at room temperature is giving comparable results. This procedure might not the best one or the more efficient, but it gives reproducible results. A dynamic cure with different temperature ramp might give similar results in a shorter timescale.

6.3.4 step F: Fiber Encapsulation

In the final step, both the fiber ends are inserted into a cell and the fiber is glued following the procedure described in **Paper III**. During the purging step of the fiber (1 week at more than 80°C) the VacSeal is applied on the exposed glue to avoid possible leaks. As reported in **Paper III** this procedure might not cure the VacSeal completely and this fact might compromise the future pressure stability of the system. The uncured VacSeal can slowly diffuse into the cell over time, polluting the gas inside the HC fiber and causing a pressure increase. The solution proposed in **Paper III** can be implemented with a dedicated *oven* design to control the pressure inside the cell and on the surrounding environment. The system could be made of an aluminum box with vacuum feed-through to connect the cell to a turbo molecular pump and the box to an oil pump. The box can be heated with a hot plate deployed underneath. In this manner, once the fiber is glued and the VacSeal applied, the fiber can be purged at the desired temperature and a lower vacuum (1

mBar) can be applied on the atmosphere surrounding the cells to cure the VacSeal. Despite the effort I put to complete this task, I have not been able to fabricate it within my Ph.D. study. The future fabrication of the oven and the further development of the sealing recipe is left to DFM.

6.4 Final Prototype Assembly

After the purging step, the system is filled with the desired gas mixture and sealed as proposed in **Paper III**. The two cells are deployed on an aluminum V-groove with the possibility to fix a free-space couplet in front of the coupling lens, in a close coupling configuration. The stand-alone optical frequency standard has been developed in two different configurations. The first prototype has been delivered to VTT institute of Helsinki (Finland) to be tested to prove its portability, as reported in **Paper II** and **Paper III**. The *Plug&Play* configuration still has the characteristic of an R&D tool, with the possibility of realign the optical beam. Despite being non customer-like, the system proves the portability of the technology for the first time, to our knowledge, also thanks to the improved mechanical stability of the novel encapsulation design.

The final goal of the portability is represented by the system published in **Paper IV**, a fiber-based reference cells at 2.05 μm using CO_2. The system is developed in collaboration with the Niels Bohr Institute (Copenhagen University) and NKT Photonics A/S, within a project involving the European Space Agency (SA) for the development of a compact and space compatible optical frequency standard for space remote sensing. This work, although performed in parallel with the main task, can be considered the natural evolution of the first prototype. In the final prototype a 100 meters long fiber is coiled on a spool with the cell encapsulation and some other optics/electronics elements that fit into a box of $25 \times 25 \times 5$ cm^3 (Fig. 4, **Paper IV**). This optical reference, fabricated with a low absorbing medium, is a representative example of the outcome of my Ph.D. project: the longer fiber required using similar gas reference and the size/weight reduction desired to be space-compatible benefit of the improvements I contribute to achieve, both on the encapsulation/sealing techniques and on the fiber characterization.

6.5 Acetylene Stand-alone Performance

Focusing on the main task of the Ph.D. study, the performance of the acetylene-based stand-alone optical frequency standard has been already reported in **Paper III**. One thing that is relevant to underline here is related to the deliverable requested by the ITN *QTea*, as reported in Chapter 1. In Figure 6.5.1 the results reported in **Paper III** are compared with the request of a *sealed HC-PCF with fractional frequency instability of* 5×10^{-11} *for averaging time* $\tau > 1$ *second*. Without going into the details of the different configurations, which

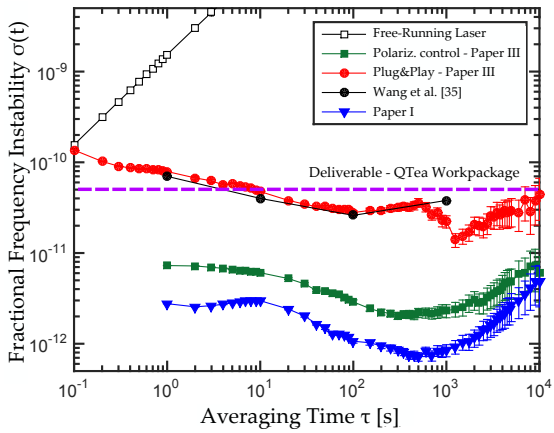

Figure 6.5.1: Comparison between the performance of the stand-alone optical frequency standard developed with control of the polarization of the light launched into the fiber (green) and without the polarization control (Plug&Play, red), the performace of the same fiber using the testing setup reported in **Paper I** (blue), the state of art of this technology before this study ([35], black) and the deliverable performance requested by the QTea work package (purple flat line). The details about the different configurations are reported in **Paper I** and **Paper III**.

are widely described in **Paper III**, the sealed HC fiber-based optical frequency standard shows an instability more than a factor of 5 lower the requested value (purple line, Fig. 6.5.1), when the light is launched with linear polarization, with orthogonal polarization between the pump and the probe. Also in the ready-to-use configuration (Plug&Play), when the polarization of the light is unknown, the instability is within the requested value for averaging time $\tau > 5$ seconds. It is important to notice that the system developed during

this study shows a performance of the sealed fiber (green curve, Fig. 6.5.1) compatible with and the one given by the same fiber using the testing setup described in Chapter 4 (green curve, Fig. 6.5.1). The difference on the instability (approximately a factor of 2) is ascribed to the different filling pressure (factor of 2) between the two experiments, as explained in **Paper III**. Therefore, we can conclude that the sealing method proposed is not compromising the fiber performance and it is suitable for this technology.

A comparison between the system developed in this study and the state of the art of the sealed HC-fiber based optical frequency standard is also reported in Table 6.5.1. The fractional frequency instability measured with the system

Table 6.5.1: Comparison between previously published results [35] using experimental conditions similar to the one presented in **Paper III**. The standard uncertainty associated with the experiment presented in this thesis corresponds to the quadrature sum of the reproducibility associated and the uncertainty of the reference laser [24] square-rooted.

Experiment	Uncertainty (1σ)	Instability (1s)	Reproducibility (1σ)
Wang et al. [35]	4.4×10^{-10}	7.0×10^{-11}	4.4×10^{-11}
Paper III Polariz. Control	7.5×10^{-11}	7.1×10^{-12}	2.7×10^{-11}
Paper III Plug&Play	5.1×10^{-11}	7.2×10^{-11}	4.9×10^{-10}

with polarization control of the launched light is almost one order of magnitude better than previously reported experiments [35]. Also the ready-to-use configuration has comparable performance with the state of the art before this study, confirming the goodness of the system developed.

6.6 Portability and Future Investigation

The portability of the system has been reported in **Paper II** and **Paper III**: the first Plug&Play prototype (slightly bigger than a shoe box) has been shipped to the VTT laboratories in Finland, and the comparable performance reported before/after the shipment confirms the portability of the proposed solution.

In reality, the first prototype developed was far from being an commercial-like product. In order to have a flavor of the capability of this encapsulation approach in terms of size/weight reduction, we can refer to the prototype proposed in **Paper IV**. The necessity to have a completely stand-alone system (both optically and electronically) required dedicated solution for the light coupling: a custom made holder for the fiber cell (V-groove) is glued in place with a free-space coupler, in a compact configuration, as shown in Fig. 6.6.1 (part 7 and 8). Without going into the details of the different components, we can notice from Fig.6.6.1 that the fiber spool (12) the EOM (9) and the fiber coupling (7,8) fit in a box of $25 \times 25 \times 5$ cm^3.

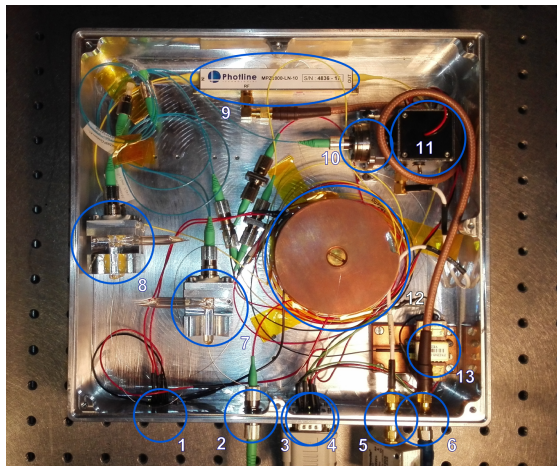

Figure 6.6.1: Reported from **Paper IV**. Portable prototype developed for the ESA project in collaboration with NKT Photonics and the Copenhagen University. Details are reported in **Paper IV**

Although the performance of the encapsulation method that I proposed is satisfactory, different approaches might be suitable for this technology, perhaps with a more production-oriented fabrication process. An example could be given by the injection-molded platform reported in **Paper V**, which is briefly introduced in Chapter 7.

The things a Ph.D. student can do to avoid writing the thesis are uncountable.
Le cose che un dottornado puó fare per evitare di scrivere la tesi sono non numberabili.

Marco Triches

7

Other Activities

In this Chapter I would like to briefly report the results of a research activity done in parallel with the the development of the main tasks of the Ph.D. project. The outcome of this collaboration with former colleagues at DTU Nanotech and DTU Physics has been published in **Paper V** and it is related to the proof-of-concept study of an in-fiber Raman detector for liquids. In this (short) chapter, the emphasis is given to the platform used to fill the HC fiber with liquids, which might be suitable as a fiber encapsulation approach for the fiber-based optical frequency standard technology.

7.1 In-Fiber Raman Spectroscopy for Liquids

In **Paper V**, an optofluidic polymer platform initially developed for performing optical stretching of blood cells is used to encapsulate a short piece of HC fiber, as reported in Fig. 7.1.1.

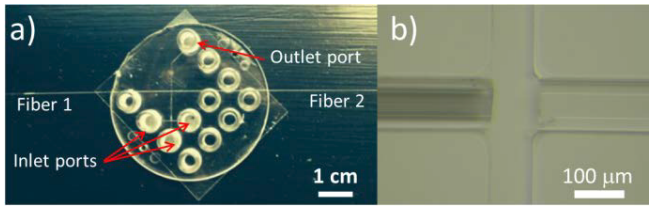

Figure 7.1.1: Reported from **Paper IV** with permission. a) Optofluidic polymer chip with a system for hydrodynamic focusing of cells and embedded optical fibers. Coupling with external fluidics is ensured by the presence of on-chip standard Luer connectors. b) Detail of chip a HC-PCF injected on the left and single-mode fiber on the Right.

The polymer platform is made of TOPAS 5013 L10 with the injection-molded procedure described in **Paper V**. The important thing to underline is that the preliminary tests on this platform demonstrate a HC-to-SM fiber optical coupling around 50% (3 dB loss), similar to the optical coupling produced by the encapsulation method reported in Chapter 6. The advantage of this approach is given by the platform reproducibility in a production-oriented fabrication process: the injection-molded chip can be fabricated a rate of 100 samples per hour, with sub-micron tolerances. The drawback is given by the material used to be produced: no studies of the outgassing of TOPS at low pressure ($\sim$ 1-30 Pa) have been found in the literature. Therefore, despite the promising results and its production-oriented technology, a deeper investigation about the performance in low pressure environment needs to be proved before implementing the platform in the optical frequency standard technology. The decision to read the details about the Raman application reported in **Paper V** are left to the reader, since they are not completely related with the main topic of this thesis.

It was hard, but it is over.
É stata dura, ma ce l'abbiamo fatta.

figure of speech

8

Conclusions

In this Chapter I summarize the results and the activities done during my Ph.D., including some comments about the future prospective for the fiber-based frequency standard technology.

8.1 Final Considerations and Future Prospective

The major aim of my Ph.D. project was to develop a portable optical frequency standard based on HC fiber technology. The main challenge was to build a suitable encapsulation method capable to combine good sealing and optical properties. The state of the art was pointing into the direction of large core Kagome fiber spliced to standard single-mode fiber to bring the technology to the market, with the target of developing an all-fiber based system. This approach presents great advantages on the size and weight reduction capability. But the main limitation is given by the difficulties to reproduce the HC fiber performance typically achievable in a testing environment in a stand-alone configuration. Pressure stability and limited control on some experimental parameters (i.e. polarization and fiber modal content) were causing this discrepancy. Moreover, the gas handling was made complicated by the chosen sealing method: filling the fiber with a mixture of reference gas (acetylene) and high pressure of *light* inert gasses (i.e. helium) which can diffuse through the glass structure after sealing cannot be considered production-oriented. On the other hand, the understanding of some light-matter interaction mechanism requires deeper investigation to be understood and the tentative to improve the HC fiber performance in this application is a continuous challenge. In such a contest, the novel encapsulation method that I contribute to develop may provide an alternative to overcome some of the limitation.

My work demonstrated that the HC fiber technology can produce a portable optical frequency standard at the 10^{-12} level. This results can be achieved with: (i) accurate selection of a HC fiber with single-mode operation at the addressed wavelength; (ii) appropriate frequency detuning between the counter-propagating beam; (iii) control of the polarization of the light launched into the HC fiber; (iv) active control of the light intensity; (v) use of dedicated encapsulation method which preserves the optical advantages of the free-space coupling in a compact configuration. Special emphasis was placed on the realization of the novel fiber encapsulation and on the comprehension of the correlation between the instability and the modal content of the HC fiber selected. I established and verified a protocol for the production of the fiber encapsulation based on small glass cells with a yield above 90%. This result was

possible thanks to the development of dedicated tools that helps to improve the overall quality of the cell. Nevertheless, the willingness to further improve the performance of the sealing method in terms of size and weight reduction bring to an possible innovative solution: an injection-molded microfabricated optomechanic platform capable at combining the desired optical properties in a production-ready *spliced*-like configuration can represent the missing piece to bridge the gap with market requirements.

I also investigated the physical reasons that may cause the instability in the large core multi-mode fiber. The proposed mechanism has been theoretically proved and a first estimate about the effects that can potentially be measured in a *real* experiment is reported, using some approximations. Finally, I proposed a relatively simple experiment that can validate the theoretical model and eventually discriminate between the effect accounted in this study and other mechanisms that may contribute to the observed frequency shift.

8.2 Future Prospective

The path for bringing this technology to the industrial market is far from being completed, despite the advancement made in this study. Luckily, the future success of this technology can rely on some novel outcomes in the fiber technology: the recent advent of the ARF and their remarkable capability of combining *quasi* single-mode operation in a large core (above 20 μm) can represent the turning point to bring the HC fiber-based system to cross the limit of 10^{-12} fractional frequency instability. This technological advancement will require a further investigation in order to optimize the overall performance, but it can potentially bring the HC fiber-based systems to approach the performance of the conventional free-space experiments for the first time. From the encapsulation prospective, the approach proposed in this study has a versatility that can be implemented in various applications, especially when a splicing approach is not feasible: in the field of high-power pulse delivery, the HC fiber technology is giving promising results with the novel ARFs and the the market request of Raman-free pulse delivery cable can be achieved by purging and sealing the fiber with an encapsulation method similar to the one proposed in this study.

Bibliography

[1] A. Michelson and C. Guillaume, "Détermination expérimentale de la valeur du mètre en longueurs d'ondes lumineuses," Travaux et Mémoires du Bureau international des Poids et Mesures **3**, 85 (1894).

[2] K. M. Evenson, J. S. Wells, F. R. Petersen, B. L. Danielson, G. W. Day, R. L. Barger, and J. L. Hall, "Speed of Light from Direct Frequency and Wavelength Measurements of the Methane-Stabilized Laser," Physical Review Letters **29**, 1346–1349 (1972).

[3] T. Udem, J. Reichert, R. Holzwarth, and T. W. Hänsch, "Absolute Optical Frequency Measurement of the Cesium D 1 Line with a Mode-Locked Laser," Physical Review Letters **82**, 3568–3571 (1999).

[4] S. Diddams, D. Jones, J. Ye, S. Cundiff, J. Hall, J. Ranka, R. Windeler, R. Holzwarth, T. Udem, and T. Hansch, "Direct link between microwave and optical frequencies with a 300 THz femtosecond laser comb," Physical review letters **84**, 5102–5 (2000).

[5] E. Hinkley, "Laser monitoring of the atmosphere," Berlin and New York **14** (1976).

[6] M. Kasevich, E. Riis, S. Chu, and R. DeVoe, "rf spectroscopy in an atomic fountain." Physical review letters **63**, 612–615 (1989).

[7] R. Holzwarth, T. Udem, T. Hansch, J. Knight, W. Wadsworth, and P. Russell, "Optical frequency synthesizer for precision spectroscopy," Physical review letters **85**, 2264–7 (2000).

[8] G. Wilpers, T. Binnewies, C. Degenhardt, U. Sterr, J. Helmcke, and F. Riehle, "Optical clock with ultracold neutral atoms." Physical review letters **89**, 230801 (2002).

[9] M. Takamoto, F.-L. Hong, R. Higashi, and H. Katori, "An optical lattice clock." Nature **435**, 321–4 (2005).

[10] M. D. Swallows, M. Bishof, Y. Lin, S. Blatt, M. J. Martin, A. M. Rey, and J. Ye, "Suppression of collisional shifts in a strongly interacting lattice clock." Science (New York, N.Y.) **331**, 1043–6 (2011).

[11] C. Chou, D. Hume, J. Koelemeij, D. Wineland, and T. Rosenband, "Frequency Comparison of Two High-Accuracy Al + Optical Clocks," Physical Review Letters **104**, 070802 (2010).

[12] C. Wieman and T. W. Hänsch, "Doppler-Free Laser Polarization Spectroscopy," Physical Review Letters **36**, 1170–1173 (1976).

[13] F. V. Kowalski, W. T. Hill, and A. L. Schawlow, "Saturated-interference spectroscopy," Optics Letters **2**, 112 (1978).

[14] M. de Labachelerie, K. Nakagawa, and M. Ohtsu, "Ultranarrow 13C2H2 saturated-absorption lines at 1.5 μm," Optics Letters **19**, 840–842 (1994).

[15] C. Chardonnet, F. Guernet, G. Charton, and C. J. Bordé, "Ultrahigh-resolution saturation spectroscopy using slow molecules in an external cell," Applied Physics B Lasers and Optics **59**, 333–343 (1994).

[16] J. Hall, C. Bordé, and K. Uehara, "Direct Optical Resolution of the Recoil Effect Using Saturated Absorption Spectroscopy," Physical Review Letters **37**, 1339–1342 (1976).

[17] G. C. Bjorklund, M. D. Levenson, W. Lenth, and C. Ortiz, "Frequency modulation (FM) spectroscopy," Applied Physics B Photophysics and Laser Chemistry **32**, 145–152 (1983).

[18] T. Hansch and B. Couillaud, "Laser frequency stabilization by polarization spectroscopy of a reflecting reference cavity," Optics Communications **35**, 441–444 (1980).

[19] J. N. Eckstein, A. I. Ferguson, and T. W. Hänsch, "High-Resolution Two-Photon Spectroscopy with Picosecond Light Pulses," Physical Review Letters **40**, 847–850 (1978).

[20] J. L. Hall, "Optical heterodyne saturation spectroscopy," Applied Physics Letters **39**, 680–682 (1981).

[21] K. Nakagawa, A. Onse, K. Okumura, and J. Yoda, "Development of a compact acetylene optical frequency standard at 1.5 μm," in "Conference on Precision Electromagnetic Measurements. Conference Digest. CPEM 2000 (Cat. No.00CH37031)," (IEEE, 2000), pp. 204–205.

[22] C. Edwards, G. Barwood, P. Gill, and W. Rowley, "Development of acetylene-stabilized diode laser frequency standards," in "The 15th Annual Meeting of the IEEE Lasers and Electro-Optics Society," , vol. 1 (IEEE, 2002), vol. 1, pp. 281–282.

[23] A. Czajkowski, A. A. Madej, and P. Dubé, "Development and study of a 1.5 μm optical frequency standard referenced to the P(16) saturated absorption line in the (ν1+ν3) overtone band of 13C2H2," Optics Communications **234**, 259–268 (2004).

[24] J. Hald, L. Nielsen, J. C. Petersen, P. Varming, and J. E. Pedersen, "Fiber laser optical frequency standard at 1.54 μm." Optics express **19**, 2052–2063 (2011).

[25] R. F. Cregan, B. Mangan, P. Russell, J. Knight, P. Roberts, and D. Allan, "Single-mode photonic band gap guidance of light in air," Science **285**, 1537–1539 (1999).

[26] F. Benabid, F. Couny, J. C. Knight, T. A. Birks, and P. S. J. Russell, "Compact, stable and efficient all-fibre gas cells using hollow-core photonic crystal fibres." Nature **434**, 488–491 (2005).

[27] J. Henningsen, J. Hald, and J. C. Peterson, "Saturated absorption in acetylene and hydrogen cyanide in hollow-core photonic bandgap fibers." Optics express **13**, 10475–10482 (2005).

[28] R. Thapa, K. Knabe, M. Faheem, A. Naweed, O. L. Weaver, and K. L. Corwin, "Saturated absorption spectroscopy of acetylene gas inside large-core photonic bandgap fiber," Optics letters **31**, 2489–2491 (2006).

[29] K. Knabe, S. Wu, J. Lim, K. A. Tillman, P. S. Light, F. Couny, N. Wheeler, R. Thapa, A. M. Jones, J. W. Nicholson, B. R. Washburn, F. Benabid, and K. L. Corwin, "10 kHz accuracy of an optical frequency reference based on (12)C2H2-filled large-core kagome photonic crystal fibers." Optics express **17**, 16017–16026 (2009).

[30] P. T. Marty, J. Morel, and T. Feurer, "All-fiber multi-purpose gas cells and their applications in spectroscopy," Journal of Lightwave Technology **28**, 1236–1240 (2010).

[31] P. S. Light, J. D. Anstie, F. Benabid, and A. N. Luiten, "Hermetic optical-fiber iodine frequency standard." Optics letters **40**, 2703–6 (2015).

[32] C. Perrella, P. S. Light, T. M. Stace, F. Benabid, and A. N. Luiten, "High-resolution optical spectroscopy in a hollow-core photonic crystal fiber," Phys. Rev. A **85**, 12518 (2012).

[33] J. Hald, J. C. Petersen, and J. Henningsen, "Saturated optical absorption by slow molecules in hollow-core photonic band-gap fibers," Physical Review Letters **98**, 213902 (2007).

[34] R. Felder, "Practical realization of the definition of the metre, including recommended radiations of other optical frequency standards (2003)," Metrologia **42**, 323–325 (2005).

[35] C. Wang, N. V. Wheeler, C. Fourcade-Dutin, M. Grogan, T. D. Bradley, B. R. Washburn, F. Benabid, and K. L. Corwin, "Acetylene frequency references in gas-filled hollow optical fiber and photonic microcells." Applied optics **52**, 5430–5439 (2013).

[36] C. Hensley, D. H. Broaddus, C. B. Schaffer, and A. L. Gaeta, "Photonic band-gap fiber gas cell fabricated using femtosecond micromachining," Optics Express **15**, 6690 (2007).

[37] P. S. Light, F. Couny, and F. Benabid, "Low optical insertion-loss and vacuum-pressure all-fiber acetylene cell based on hollow-core photonic crystal fiber," Optics Letters **31**, 2538 (2006).

[38] R. Thapa, K. Knabe, K. L. Corwin, and B. R. Washburn, "Arc fusion splicing of hollow-core photonic bandgap fibers for gas-filled fiber cells," Optics Express **14**, 9576 (2006).

[39] F. Couny, F. Benabid, and P. Light, "Reduction of Fresnel Back-Reflection at Splice Interface Between Hollow Core PCF and Single-Mode Fiber," IEEE Photonics Technology Letters **19**, 1020–1022 (2007).

[40] Neoark, "Neoark C2H2LDS-1540," .

[41] K. Nakagawa, M. de Labachelerie, Y. Awaji, and M. Kourogi, "Accurate optical frequency atlas of the 1.5-μm bands of acetylene," Journal of the Optical Society of America B **13**, 2708 (1996).

[42] E. N. Fokoua, M. N. Petrovich, N. K. Baddela, N. V. Wheeler, J. R. Hayes, F. Poletti, and D. J. Richardson, "Real-time prediction of structural and optical properties of hollow-core photonic bandgap fibers during fabrication." Optics letters **38**, 1382–1384 (2013).

[43] F. Poletti, "Nested antiresonant nodeless hollow core fiber," Optics Express **22**, 23807 (2014).

[44] F. Poletti, M. N. Petrovich, and D. J. Richardson, "Hollow-core photonic bandgap fibers: technology and applications," Nanophotonics **2**, 315–340 (2013).

[45] M. N. Petrovich, F. Poletti, A. van Brakel, and D. J. Richardson, "Robustly single mode hollow core photonic bandgap fiber," Optics Express **16**, 4337 (2008).

[46] G. Antonopoulos, F. Benabid, T. A. Birks, D. M. Bird, J. C. Knight, and P. S. J. Russell, "Experimental demonstration of the frequency shift of bandgaps in photonic crystal fibers due to refractive index scaling," Optics Express **14**, 3000 (2006).

[47] J. Noda, K. Okamoto, and Y. Sasaki, "Polarization-maintaining fibers and their applications," Journal of Lightwave Technology **4**, 1071–1089 (1986).

[48] J. K. Lyngsø, C. Jakobsen, H. R. Simonsen, and J. Broeng, "Truly single-mode polarization maintaining hollow core PCF," OFS2012 22nd International Conference on Optical Fiber Sensor **8421**, 84210C–84210C–4 (2012).

[49] M. Michieletto, J. K. Lyngsø, J. Lægsgaard, and O. Bang, "Cladding defects in hollow core fibers for surface mode suppression and improved birefringence." Optics express **22**, 23324–23332 (2014).

[50] J. M. Fini, J. W. Nicholson, B. Mangan, L. Meng, R. S. Windeler, E. M. Monberg, A. DeSantolo, F. V. DiMarcello, and K. Mukasa, "Polarization maintaining single-mode low-loss hollow-core fibres." Nature communications **5**, 5085 (2014).

[51] J. K. Lyngsø, C. Jakobsen, H. R. Simonsen, and J. Broeng, "Single-mode 7-cell core hollow core photonics crystal fiber with increased bandwidth," in "21st International Conference on Optical Fibre Sensors (OFS21)," , vol. 7753, W. J. Bock, J. Albert, and X. Bao, eds. (International Society for Optics and Photonics, 2011), vol. 7753, p. 77533Q.

[52] R. M. Gerosa, D. H. Spadoti, L. d. S. Menezes, and C. J. S. de Matos, "In-fiber modal Mach-Zehnder interferometer based on the locally post-processed core of a photonic crystal fiber." Optics express **19**, 3124–3129 (2011).

[53] W. R. Bennett, "Hole Burning Effects in a He-Ne Optical Maser," Physical Review **126**, 580–593 (1962).

[54] W. E. Lamb, "Theory of an Optical Maser," Physical Review **134**, 1429–1450 (1964).

[55] W. Phillips and W. Phillips, "Laser-cooling and trapping neutral atoms," Annales de Physique **10**, 717–732 (1985).

[56] M. Kasevich and S. Chu, "Laser cooling below a photon recoil with three-level atoms," Physical Review Letters **69**, 1741–1744 (1992).

[57] V. S. Letokhov and V. Chebotayev, *Nonlinear Laser Spectroscopy* (1977).

[58] W. Demtröder, *Laser Spectroscopy: Basic Concepts and Instrumentation* (Springer, 1996).

[59] G. C. Bjorklund, "Frequency-modulation spectroscopy: a new method for measuring weak absorptions and dispersions," Optics Letters **5**, 15 (1980).

[60] K. Shimoda, *Topics in Applied Physics: High-Resolution Laser Spectroscopy*, vol. 13 of *Topics in Applied Physics* (Springer, Berlin, Heidelberg, 1976).

[61] K. Knabe, R. Thapa, B. Washburn, and K. Corwin, "Reflected Pump Technique for Saturated Absorption Spectroscopy Inside Photonic Bandgap Fibers," 2007 Conference on Lasers and Electro-Optics (CLEO) **28**, 3–4 (2007).

[62] C. Wang, S. Wu, B. Mangan, L. Meng, J. M. Fini, R. S. Windeler, E. M. Monberg, A. Desantolo, K. Mukasa, J. W. Nicholson, D. DiGiovanni, B. R. Washburn, and K. L. Corwin, "Single-mode hollow-core fiber for portable acetylene sub-Doppler frequency reference," in "CLEO: 2014," (OSA, Washington, D.C., 2014), p. SM3N.7.

[63] J. Gray and D. Allan, "A Method for Estimating the Frequency Stability of an Individual Oscillator," in "28th Annual Symposium on Frequency Control," (IEEE, 1974), pp. 243–246.

[64] D. W. Allan and J. A. Barnes, "A Modified "Allan Variance" with Increased Oscillator Characterization Ability," Proceedings of the 35th Annula Frequency Control Symposium, USAERADCOM pp. 470–474 (1981).

[65] F. Riehle, *Frequency Standards* (Wiley-VCH Verlag GmbH & Co. KGaA, Weinheim, FRG, 2003).

[66] V. Dangui, H. K. Kim, M. J. F. Digonnet, and G. S. Kino, "Phase sensitivity to temperature of the fundamental mode in air-guiding photonic-bandgap fibers," Optics Express **13**, 6669–6684 (2005).

[67] M. Michieletto, J. K. Lyngsø, C. Jakobsen, J. Lægsgaard, O. Bang, and T. T. Alkeskjold, "Hollow-core fibers for high power pulse delivery," Optics Express **24**, 7103 (2016).

[68] S. E. Park, H. S. Lee, T. Y. Kwon, and H. Cho, "Dispersion-like signals in velocity-selective saturated-absorption spectroscopy," Optics Communications **192**, 49–55 (2001).

[69] C. H. Papas, *Theory of electromagnetic wave propagation* (Courier Corporation, 2014).

[70] J. W. Nicholson, A. D. Yablon, J. M. Fini, and M. D. Mermelstein, "Measuring the Modal Content of Large-Mode-Area Fibers," IEEE Journal of Selected Topics in Quantum Electronics **15**, 61–70 (2009).

[71] P. G. Westergaard, M. Lassen, and J. C. Petersen, "Differential high-resolution stimulated CW Raman spectroscopy of hydrogen in a hollow-core fiber," Optics express **23**, 16320–8 (2015).

Appendix I. List of Publications and Submitted Manuscripts

Paper I

Optical frequency standard using acetylene-filled hollow-core photonic crystal fibers

M. Triches, M. Michieletto, J. Hald, J. K. Lyngsø, J. Lægsgaard and O. Bang

Optics Express, Vol. 23, Issue 9, pp. 11227-11241 (2015)

Optical frequency standard using acetylene-filled hollow-core photonic crystal fibers

Marco Triches,[1,2,*] Mattia Michieletto,[2,3] Jan Hald,[1] Jens K. Lyngsø,[3] Jesper Lægsgaard,[2] and Ole Bang[2]

[1] *Danish Fundamental Metrology, Matematiktorvet 307, 2800 Kgs. Lyngby, Denmark*
[2] *DTU Fotonik, Department of Photonics Engineering, Technical University of Denmark, Ørsteds Plads 343, 2800 Kgs. Lyngby, Denmark*
[3] *NKT Photonics A/S - Blokken 84, 3460 Birkerød, Denmark*
** mt@dfm.dk*

Abstract: Gas-filled hollow-core photonic crystal fibers are used to stabilize a fiber laser to the $^{13}C_2H_2$ P(16) ($\nu_1 + \nu_3$) transition at 1542 nm using saturated absorption. Four hollow-core fibers with different crystal structure are compared in terms of long term lock-point repeatability and fractional frequency instability. The locked fiber laser shows a fractional frequency instability below 4×10^{-12} for averaging time up to 10^4 s. The lock-point repeatability over more than 1 year is 1.3×10^{-11}, corresponding to a standard deviation of 2.5 kHz. A complete experimental investigation of the light-matter interaction between the spatial modes excited in the fibers and the frequency of the locked laser is presented. A simple theoretical model that explains the interaction is also developed.

OCIS codes: (120.0120) Instrumentation, measurement, and metrology; (140.3425) Laser stabilization; (140.3510) Lasers, fiber; (300.6460) Spectroscopy, saturation; (060.5295) Photonic crystal fibers.

References and links

1. R. Felder, "Practical realization of the definition of the metre, including recommended radiations of other optical frequency standards (2003)," Metrologia **42**, 323–325 (2005).
2. M. de Labachelerie, K. Nakagawa, and M. Ohtsu, "Ultranarrow $^{13}C_2H_2$ saturated-absorption lines at 1.5 μm," Opt. Lett. **19**, 840–842 (1994).
3. J. L. Hall, "Optical heterodyne saturation spectroscopy," Appl. Phys. Lett. **39**, 680–682 (1981).
4. C. Chardonnet, F. Guernet, G. Charton, and C. J. Bordé, "Ultrahigh-resolution saturation spectroscopy using slow molecules in an external cell," Appl. Phys. B: Lasers Opt. **59**, 333–343 (1994).
5. C. Edwards, G. Barwood, P. Gill, and W. Rowley, "Development of acetylene-stabilized diode laser frequency standards," in "15th Annu. Meet. IEEE Lasers Electro-Optics Soc.", (IEEE, 2002), vol. 1, pp. 281–282.
6. A. Czajkowski, A. A. Madej, and P. Dubé, "Development and study of a 1.5 μm optical frequency standard referenced to the P(16) saturated absorption line in the (ν1+ν3) overtone band of $^{13}C_2H_2$," Opt. Commun. **234**, 259–268 (2004).
7. J. Hald, L. Nielsen, J. C. Petersen, P. Varming, and J. E. Pedersen, "Fiber laser optical frequency standard at 1.54 μm," Opt. Express **19**, 2052–2063 (2011).
8. R. F. Cregan, B. Mangan, P. Russell, J. Knight, P. Roberts, and D. Allan, "Single-mode photonic band gap guidance of light in air," Science **285**, 1537–1539 (1999).
9. F. Benabid, F. Couny, J. C. Knight, T. a. Birks, and P. S. J. Russell, "Compact, stable and efficient all-fibre gas cells using hollow-core photonic crystal fibres," Nature **434**, 488–491 (2005).
10. J. Henningsen, J. Hald, and J. C. Peterson, "Saturated absorption in acetylene and hydrogen cyanide in hollow-core photonic bandgap fibers," Opt. Express **13**, 10475–10482 (2005).

11. R. Thapa, K. Knabe, M. Faheem, A. Naweed, O. L. Weaver, and K. L. Corwin, "Saturated absorption spectroscopy of acetylene gas inside large-core photonic bandgap fiber," Opt. Lett. **31**, 2489–2491 (2006).
12. K. Knabe, S. Wu, J. Lim, K. a. Tillman, P. S. Light, F. Couny, N. Wheeler, R. Thapa, A. M. Jones, J. W. Nicholson, B. R. Washburn, F. Benabid, and K. L. Corwin, "10 kHz accuracy of an optical frequency reference based on $^{12}C_2H_2$-filled large-core kagome photonic crystal fibers," Opt. Express **17**, 16017–16026 (2009).
13. P. T. Marty, J. Morel, and T. Feurer, "All-fiber multi-purpose gas cells and their applications in spectroscopy," J. Light. Technol. **28**, 1236–1240 (2010).
14. J. Henningsen and J. Hald, "Dynamics of gas flow in hollow core photonic bandgap fibers," Appl. Opt. **47**, 2790–2797 (2008).
15. C. Wang, N. V. Wheeler, C. Fourcade-Dutin, M. Grogan, T. D. Bradley, B. R. Washburn, F. Benabid, and K. L. Corwin, "Acetylene frequency references in gas-filled hollow optical fiber and photonic microcells," Appl. Opt. **52**, 5430–5439 (2013).
16. C. Wang, N. V. Wheeler, J. Lim, K. Knabe, M. Grogan, Y. Wang, B. R. Washburn, F. Benabid, and K. L. Corwin, "Portable acetylene frequency references inside sealed hollow-core kagome photonic crystal fiber," in "CLEO2011 - Laser Appl. to Photonic Appl.", (OSA, 2011), p. CFC1.
17. P. J. Roberts, D. P. Williams, H. Sabert, B. J. Mangan, D. M. Bird, T. A. Birks, J. C. Knight, and P. S. J. Russell, "Design of low-loss and highly birefringent hollow-core photonic crystal fiber," Opt. Express **14**, 7329–7341 (2006).
18. R. M. Gerosa, D. H. Spadoti, L. d. S. Menezes, and C. J. S. de Matos, "In-fiber modal Mach-Zehnder interferometer based on the locally post-processed core of a photonic crystal fiber," Opt. Express **19**, 3124–3129 (2011).
19. M. Kusaba and J. Henningsen, "The $\nu_1+\nu_3$ and the $\nu_1+\nu_2+\nu_4^1+\nu_5^{-1}$ combination bands of $^{13}C_2H_2$. linestrengths, broadening parameters, and pressure shifts," J. Mol. Spectrosc. **209**, 216–227 (2001).
20. V. S. Letokhov, *High-Resolution Laser Spectroscopy*, vol. 13 of *Topics in Applied Physics* (Springer, 1976).
21. J. Hald, J. C. Petersen, and J. Henningsen, "Saturated optical absorption by slow molecules in hollow-core photonic band-gap fibers," Phys. Rev. Lett. **98**, 213902 (2007).
22. V. Dangui, H. K. Kim, M. J. F. Digonnet, and G. S. Kino, "Phase sensitivity to temperature of the fundamental mode in air-guiding photonic-bandgap fibers," Opt. Express **13**, 6669–6684 (2005).
23. D. Payne, A. Barlow, and J. Ramskov Hansen, "Development of low- and high-birefringence optical fibers," IEEE Trans. Microwave Theory Tech. **30**, 323–334 (1982).
24. I. Kaminow, "Polarization in optical fibers," IEEE J. Quantum Electron. **17**, 15–22 (1981).
25. W. Demtröder, *Laser Spectroscopy: Basic Concepts and Instrumentation* (Springer, 1996).
26. J. M. Fini, J. W. Nicholson, B. Mangan, L. Meng, R. S. Windeler, E. M. Monberg, A. DeSantolo, F. V. DiMarcello, and K. Mukasa, "Polarization maintaining single-mode low-loss hollow-core fibres," Nat. Commun. **5**, 5085 (2014).
27. M. Michieletto, J. K. Lyngsø, J. Lægsgaard, and O. Bang, "Cladding defects in hollow core fibers for surface mode suppression and improved birefringence," Opt. Express **22**, 23324–23332 (2014).
28. E. N. Fokoua, M. N. Petrovich, N. K. Baddela, N. V. Wheeler, J. R. Hayes, F. Poletti, and D. J. Richardson, "Real-time prediction of structural and optical properties of hollow-core photonic bandgap fibers during fabrication," Opt. Lett. **38**, 1382–1384 (2013).
29. J. K. Lyngsø, C. Jakobsen, H. R. Simonsen, and J. Broeng, "Single-mode 7-cell core hollow core photonics crystal fiber with increased bandwidth," Proc. SPIE in "21st Int. Conf. Opt. Fibre Sensors," **7753**, 77533Q (International Society for Optics and Photonics, 2011).
30. J. L. Hall and C. J. Borde, "Shift and broadening of saturated absorption resonances due to curvature of the laser wave fronts," Appl. Phys. Lett. **29**, 788–790 (1976).
31. S. E. Park, H. S. Lee, T. Y. Kwon, and H. Cho, "Dispersion-like signals in velocity-selective saturated-absorption spectroscopy," Opt. Commun. **192**, 49–55 (2001).

---

1. Introduction

Portable optical frequency standards are important in metrology and in many other applications (optical sensing, telecommunication, aerospace, etc.) that need an accurate and reliable optical reference away from the laboratories. In the telecommunication band the $^{13}C_2H_2$ P(16) ($\nu_1+\nu_3$) line at 1542.3837 nm is the recommended optical transition for the realization of the meter [1]. During the last decade, I_2, acetylene and Rb vapour cells have been widely investigated and implemented in laser stabilization using the saturated absorption spectroscopy (SAS) technique [2], often combined with frequency modulated spectroscopy [3–7]. Since the demonstration of the first photonic band gap guidance in air [8], the increased availability of fibers with an hollow core (HC) allowed to investigate the realization of a *portable*

optical frequency reference based on a gas-filled HC fiber [9–13].

Hollow core fibers are particularly useful in this technology because they provide a very long interaction length in a compact space. Moreover, the possibility to develop an all fiber-based optical reference makes this solution easier to implement in an industrial environment. However, developing a portable and user-friendly optical frequency standard is not free of challenges; although fiber gas-filling and other main technical issues have already been characterized [14], targeting the most suitable fiber for this technology is still under debate. State of the art research suggest that kagome fibers produce better performance than more common hollow core photonic crystal fibers (HC-PCF), both in terms of lock-point repeatability and stability [12, 15]. Limited transit-time broadening due to larger core size and absence of surface modes are the key-features of the kagome fibers. On the other hand, they are highly multi-mode, which could create an issue for long term frequency stability, as mentioned in [12].

SAS technique used to frequency-lock lasers to a sub-Doppler optical transition is limited by the strength of the signal and the linewidth of the sub-Doppler feature. Maximizing the strength of the signal while choosing a narrow-linewidth transition is the target of any frequency locking scheme. As shown in previous work [10], the major contribution to the width of a sub-Doppler absorption line in HC fibers is due to the transit-time broadening effect. Therefore, having a larger core diameter seems to be the best solution to reduce the instability.

Despite the previous considerations, the multi-mode characteristic of the large core kagome fibers could introduce a factor of instability, mainly related to the lock-point repeatability. Previously published works ascribe this effect to the presence of high order modes (HOMs) [12], surface modes [15] inside the *band gap* or polarization instability between the pump and probe beams [16]. The mechanism ascribed to the lock-point inaccuracy presented in [12] suffers a lack of universality and it cannot explain some of the effects presented in these paper. This work aims at demonstrating that most of these effects are directly connected to the interaction between different spatial modes inside the fiber. The correlation between the modes excited in the HC fibers and the repeatability of the lock-point is investigated and a simple theoretical approach is proposed to explain the physical mechanism involved.

Here we present a complete characterization of four different HC-PCFs, investigating their performances, using SAS combined with a frequency modulation spectroscopy technique. The performance achieved improves previously published results [12, 15] for gas-filled HC fibers both in terms of frequency stability and lock-point repeatability, reducing the gap with respect to the performance achieved with bulk glass cells [7].

2. Fiber characterization

2.1. Fiber specifications overview

Before testing the fibers in the SAS setup, a detailed investigation on the HOM contents of the various HC fibers is needed to check any (possible) correlation between the HOMs guided and the stabilization performance. In this section we compare the fiber characteristics with the HOMs investigation. The relevant properties of the HC fibers are listed in Table 1. Three fibers have a 7-cell core whereas the last one is a 19-cell HC fiber. The C7_ PM fiber differs from all the others as it is fabricated to be polarization maintaining (PM). The enhanced birefringence needed to have the PM property is introduced thanks to four anti-resonant features on the core wall [17]. At the same time, these features lead to improved mode confinement. The C7_ L and C7_ S fiber have about the same crystal structure, but with different scaling factor (*pitch*), which results in a larger core size of C7_ L with respect to C7_ S. To simplify the notation, in the rest of the manuscript we will refer to the different fibers as *single* mode, *few* mode or *multi* mode fiber with respect to the mode content at 1542 nm. All the fibers tested have a total loss lower than 18 dB/Km at the addressed wavelength and they are provided by NKT Photonics.

Table 1. Summary of the fiber characteristics.

Specs/Name	C7_ PM	C7_ L	C7_ S	C19
Core	7-cell	7-cell	7-cell	19-cell
Core diameter	9.3 μm	11.9 μm	8.5 μm	20.0 μm
MFD	6.8 μm	8.2 μm	5.4 μm	13.2 μm
Coupling	63%	67%	61%	72%
PM property	PM	non-PM	non-PM	non-PM
Modes property	single-mode	*few*-mode	single-mode	multi-mode
Structure	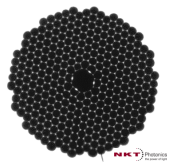	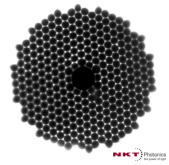		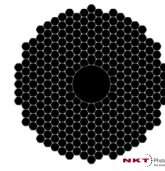

2.2. HOMs characterization: in-fiber Mach-Zender interferometer

The HOM characterization is performed using a setup similar to the one presented in [18]. A super-continuum source (0.45-2.4 μm) is coupled to a piece of 8 cm of HC fiber and is collected with a single-mode (SM) fiber into an optical spectrum analyzer (OSA). Each spectrum is recorded across most of the fiber band gap with 0.1 nm resolution. The total field distribution and hence the coupling efficiency to the SM fiber depends on the relative phase of the modes. The different spatial modes excited in the HC fiber are interfering once collected into the SM fiber, due to their different group velocity. The configuration is similar to a Mach-Zender interferometer, where the reference arm is provided by the light in the fundamental mode (FM). The difference between the group velocity of the FM and the one of a given HOM/surface mode gives rise to a wavelength dependent phase difference. The spectrum is then processed applying a windowed Fourier transform (WFT) analysis, which highlights the HOMs excited in terms of the group velocity refractive index difference (Δn_g) with respect to the FM ($\Delta n_g = 0$). The results are presented in Fig. 1. The *flat* feature visible at $\Delta n_g \simeq 0.08$ that affects most of the spectrum is an artifact introduced by the apparatus. In fact, it does not depend on the fiber tested because it is reproduced in all the tests performed at the same effective group index difference. Except from this artifact, the fibers show widely different features. The C7_ PM has a strong feature with $\Delta n_g \leq 0.05$, which covers most of the spectrum and strongly diverges around 1650 nm: this is probably due to an anti-crossing between the FM and a surface mode. Despite the measurement here presented could not resolve it, the fiber guides two orthogonal polarized FMs with two different effective refractive index (and/or different group velocity refractive index), due to its enhanced birefringence. The C19 fiber is clearly showing a multi-mode behavior.

The most interesting features are related to the C7_ L and the C7_ S. Even though they have a similar photonic crystal structure, the larger core of the C7_ L fiber allows *few* HOMs to be guided at 1542 nm, with propagation constant close to the FM, which are absent in the C7_ S spectrum. Moreover, a strong beating at a higher group index difference ($\Delta n_g \approx 0.15$) suggests the presence of a *surface* mode (localized on the core-wall). These considerations will be more clear in Section 5.1, where the C7_ L spectrum acquired will be compared with simulations.

The HOM excitation in the HC fibers is also strongly influenced by the coupling. In order to characterize the coupling dependence of the spectra observed, the measurements are repeated with a (strongly) misaligned in-coupling beam: the misalignment increases the light intensity coupled to the various HOM components, but does not give rise to any HOMs different than

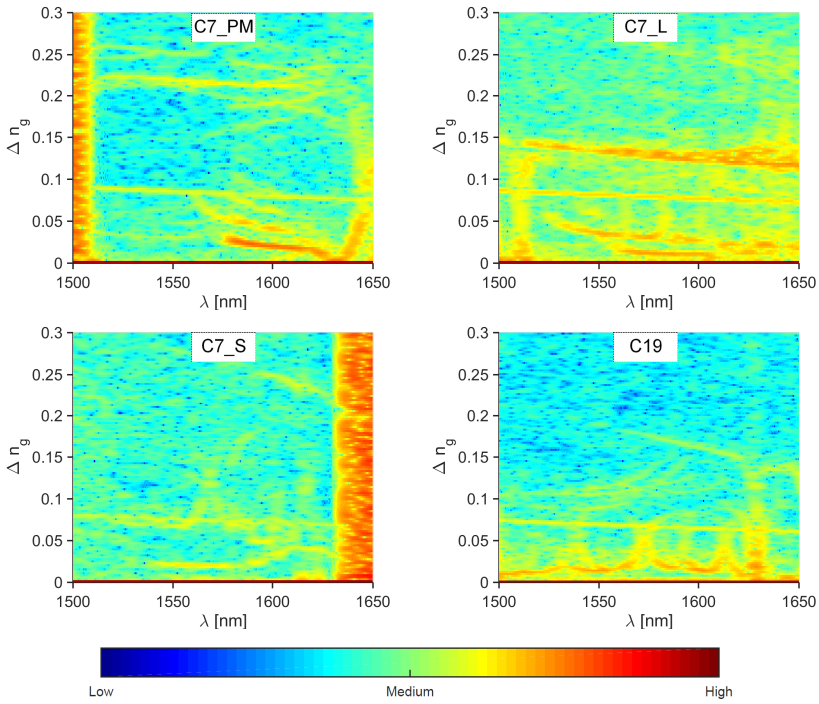

Fig. 1. WFT analysis of the spectra collected. The HOMs/surface modes are represented by the *yellow/orange* features. The the *red* border represent the band gap edge/cladding modes (C7_S). The "flat" yellow feature present in all the measurements ($\Delta n_g \approx 0.08$) is an artifact introduced by the setup. The colors represent the light intensity, according to the legend [a.u.].

the ones previously observed. This test also simulates the effect of possible deviations from optimal coupling that might occur in the SAS setup. The investigations in [12] suggest that the presence of the HOMs/surfaces mode in similar setup could shift the frequency of the locked laser by few MHz, but an high number of HOMs should average out the effect, reducing the overall shift observed (on the order of few kHz). Moreover, the presence of some surface modes could enhance the light coupling to the HOMs, changing the mode field distribution of the core-guided modes [15]. Following these interpretations, the highly multi-mode fiber (C19) should produce a limited shift of a few kHz, while no shift of the locked laser frequency is expected if no HOMs are excited (C7_S fiber). On the contrary, the shift should be stronger (a few MHz) if only a *few* HOMs are excited at the operational wavelength (C7_L fiber), because the averaging mechanism does not occur to reduce overall shift. As the following analysis will clarify, some of these assumptions appear incorrect.

3. Experimental SAS setup

A SAS setup similar to the one described in [3] is used to investigate the four different HC fibers (Fig. 2). A sealed box with AR coated windows is connected to a vacuum pump and to

an acetylene vessel. A fiber laser source (Koheras E15 Adjustik^{TM}) of 30 mW power is split into two beams, and coupled into the HC fiber placed inside the box with free-space optics.

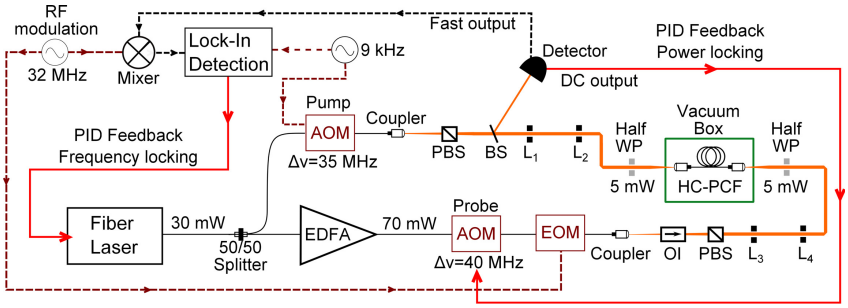

Fig. 2. Schematic layout of the SAS Setup. OI: optical isolator. (P)BS: (polarized) beam splitter. L_{1-4}: lenses. Half WP: half wave plate.

Using an acousto-optic modulator (AOM) the light of the first beam (called *pump*) is intensity modulated at 9 kHz using an external square-wave function generator, and blue-detuned by 35 MHz. The other (*probe*) beam is blue-detuned by 40 MHz using a second AOM, after being amplified by an erbium-doped fiber amplifier (EDFA). This configuration avoids low-frequency noise ($\leq$100 kHz) from the interference between the two counter-propagating beams, while it maintains the sub-Doppler feature in the central part of the Doppler absorption profile, where the signal-to-noise ratio is high.

The probe is also phase modulated through an electro-optic modulator (EOM) at 32 MHz to generate the side-bands needed for frequency modulation spectroscopy. The transmitted probe beam is detected using a beam splitter and free space coupling to a low noise detector, with both AC and DC response. The fast signal is used to lock the laser to the optical transition, using a lock-in amplifier combined with a servo-loop. The same square function used to modulate the pump intensity is providing the detection reference. Meanwhile, the DC output is used to stabilize the probe power via the probe AOM. Both beams have a power of 5.5 mW at the HC-fiber input; since the saturation power (P_{sat}) measured in similar system is more than 20 mW [10], the experiment presented here is in the low saturation regime ($P \ll P_{\text{sat}}$). A small fraction of the laser output is combined with the output of a reference laser and the resulting beat signal is monitored with a fast photodiode and a frequency counter. The reference laser is locked to an an acetylene bulk glass cell as described in [7] and it has a frequency instability (Allan deviation) below 5×10^{-13} for sampling time $1 < \tau < 10^5$ s and a lock-point repeatability of about 100 Hz.

The box is temperature controlled through a Peltier cell deployed underneath and the temperature inside the box is monitored using two Pt-100 probes. This configuration allows testing the fibers both in a stable and varying temperature environment, in order to investigate how fiber temperature affects the frequency stability. The polarization of the two counter propagating beams is controlled using a polarized beam splitter (PBS) combined with zero-order half wave plates. The fiber is placed inside the chamber, coiled with a diameter of about 6 cm. Once cleaved, both the facets are connected to a free space coupler fixed inside the chamber, using bare fiber adapters. Each fiber is left under vacuum ($\leq 3 \times 10^{-6}$ hPa) for about a week.

After the purging step, the chamber is exposed to 29 Pa of $^{13}C_2H_2$ vapour. All the fibers tested are about 3 m. The filling pressure and the length of the fibers have been chosen to limit the filling time (less than 30 min) and the pressure broadening. Therefore, the contribution to

the full with half maximum (FWHM) of the transition profile due to the gas pressure is limited to 6 MHz [7], while the calculated absorption of the $^{13}C_2H_2$ P(16) line for a 3 m fiber at 29 Pa is about 54% [19]. As previously mentioned, the transit-time broadening is the major limiting factor for SAS in HC fibers, because the mode field diameter (MFD) is one order of magnitude smaller than what is typically used in bulk vapour cell systems. This effect is inversely proportional to the MFD and the FWHM contribution is about 15 to 30 MHz, depending on the fiber tested [20, 21].

4. Performance evaluation

The fiber test takes about 30 hours and it is subdivided in three consecutive phases. In the first phase the temperature of the is box stabilized to 24°C (12 hours) while a temperature variation is induced during the second phase (12 hours, see Section 4.2). During the third phase, the temperature is restored to the initial condition and the fiber is tested to check that performance is consistent with the one observed in the first phase. The last phase takes about 6 hours and it is important to check that the temperature ramp does not introduce any permanent effects in the setup/fiber due to thermal expansion of some components inside the box (fiber holder, free space couplers etc). All the measurements presented show comparable performance between the first and third phase. The measurements are also repeated after each fiber is re-cleaved/re-filled to check the reproducibility of the results, presenting comparable performance. The second phase is done to check the temperature sensitivity and to simulate the the long term performance of the fiber. The temperature variation has been previously investigated as a source of phase instability in fiber optic gyroscope (FOG) applications [22], arising from the differential thermal expansion between the spool and the glass, and the instability observed is stronger if the fiber is birefringent. The birefringence could be due to a deformed/elliptical core [23] or because of the anti-resonant elements introduced in the core wall (C7_ PM). Moreover, the temperature stress induces small mechanical variations in the components inside the box (coupler/holder), simulating coupling changes that could occur on the long term scale (days). The frequency difference between the laser locked to the gas-filled HC fibers and the reference laser are presented in Fig. 3 and 4 together with the corresponding fractional frequency instability (Allan deviation). The frequency offset results are plotted with a relative shift of 100 kHz for clarity.

4.1. Temperature stabilized environment

Here we present the results obtained with the four fibers under a temperature stabilized environment (first phase). The difference between the single-mode and the multi-mode fibers is clearly visible (Fig. 3, left). The fluctuations observed are within about 25 kHz for most of the fibers, while the laser locked to fiber C7_ S shows a remarkable *stability* with an offset limited to 4 kHz. This test confirms that the presence of the multiple modes excited in a fiber contributes to a shift of the laser frequency.

The performance of the C7_ PM fiber needs a dedicated explanation: although the previous analysis (Fig. 1) does not show the presence of HOMs at 1542 nm, this fiber guides two *orthogonal* polarized modes with a slightly different effective refractive index. In this sense, the interaction between the two orthogonal polarized FMs introduces a perturbation in the light-matter interaction similar to the one given by a FM-HOM one. The interaction mechanism will be discussed in Section 6. Moreover, if the launched polarization is not aligned to one of the major axes, the SAS configuration will not be the one described in Section 3 (two counter propagating beams with orthogonal polarized light). Depending on the *beat length* of the fiber and on the misalignment, the modal content could vary over the interaction length, generating a superposition of linear/elliptical/circular polarized light in both the beams [24]. This non-homogeneous polarization combined with the different propagation constant of the two orthogonal polarized

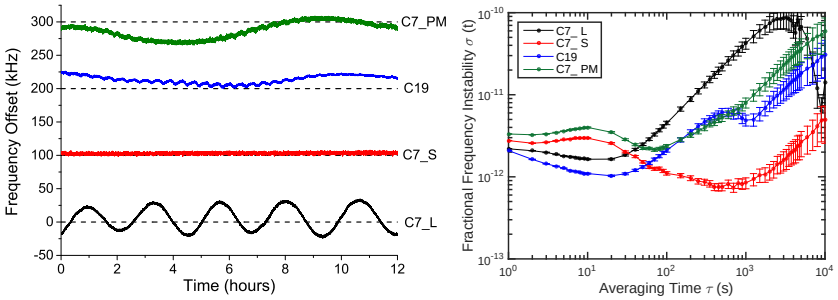

Fig. 3. Stable environment test: Frequency of the locked laser over time (left). The results are plotted with a relative shift of 100 kHz for clarity, after the frequency of the reference laser [7] is subtracted. Fractional frequency instability (*Allan* deviation) of the four fibers (right).

FMs could contribute to the instability observed in Fig. 3. This consideration is supported by the measurements done during the temperature variation (Fig. 4).

The fractional frequency instability is presented in Fig. 3 (right). The long-term performance ($\tau \geq 100$ s) confirms the remarked difference between the C7_ S and the other fibers: the *multi-mode* fibers follow the same trend (increased instability), while the C7_ S presents an instability below 4×10^{-12} for $1 < \tau < 10^4$ s. In the short term ($\tau < 100$ s), the instability is inversely proportional to the MFD: the noise of the locked-laser depends on the slope of the error signal produced for locking, which is inversely proportional to the linewidth (FWHM) of the transition addressed. The linewidth is dominated by the transit-time broadening caused by the small beam diameter [20, 21]. The measured instability confirms this effect within the experimental uncertainties, except for the PM fiber, since the MFD of the C7_ PM is larger than the C7_ S. The second phase of the test could help to clarify this unexpected performance.

4.2. Environment under temperature variation

The temperature ramp applied is described in Fig. 4 (bottom-right corner). The test under temperature variation confirms the validity of the previous analysis: the amplitude of the fluctuations observed in the *multi-mode* fibers are comparable, while the frequency variations of the C7_ S fiber remain within 10 kHz. Despite the slow temperature variation introduced (less than 1.7°C/hour, Fig. 4 bottom-right corner), the perturbation can easily excite HOMs/surface modes, increasing the instability. The test also shows that the lock-point stability is almost temperature insensitive for the C7_ S fiber, maintaining the fractional frequency instability well below 1×10^{-11}, giving us the best candidate for a future portable optical frequency standard. Practically, the thermal stress introduced is enhancing the frequency fluctuations previously observed (Fig. 3, left), reducing the timescale of the oscillations by a factor 10. This fact confirms that the introduced stress helps to understand the long-term performance of the various fibers, considerably reducing the total acquisition time. All the measurements show comparable maximum shift in the repeated tests. A detailed analysis of the PM fiber performance in Fig. 4 shows that the fractional frequency instability at 1 s averaging time is increased by a factor 2 with respect to to what observed in the first phase of the test (Fig. 3). This effect occurs only to the PM fiber while the others show comparable instability in all the phases of the test (at 1 s). Moreover, the instability of the C7_ PM shown during the third phase of the test reproduces the behavior shown in Fig. 3, excluding that a permanent perturbation has been introduced on the

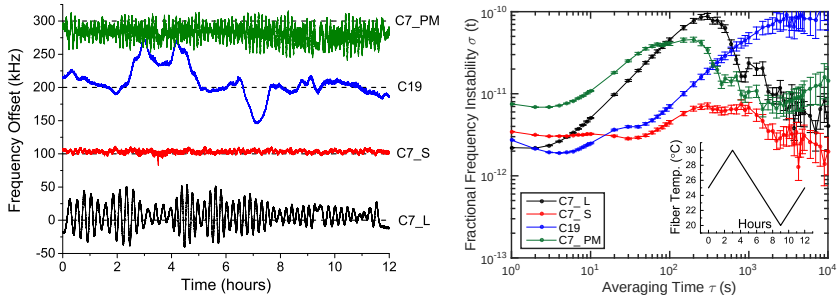

Fig. 4. Stress test. Frequency of the locked laser over time (left). The results are plotted with a relative shift of 100 kHz for clarity, after the frequency of the reference laser [7] is subtracted. Fractional frequency instability (*Allan* deviation) of the four fibers (right). The temperature ramp applied is plotted in the bottom-right corner.

setup/fiber.

This effect could not be ascribed to the HOMs contribution to the light-matter interaction, which can explain the long term oscillations observed ($\tau > 10$ s), as presented in Sec. 6. Following the previous considerations, a possible explanation could come from the polarization instability, since the different light polarization between the pump and probe beam is known to affect Lamb dip detection [25]. The mechanical stress introduced by the temperature ramp could cause small *deformations* in the fiber structure, changing the relative propagation constant between the two orthogonal polarized FMs [22, 23]. An other source of instability could come from the presence of some surface modes introduced by the special core wall structure of this fiber. Since the maximum Δn_g shown in Fig. 1 is limited by the resolution of the OSA, there could be some surface modes at 1542 nm with $\Delta n_g > 0.3$, which are not highlighted by the measurements. The tests performed allow anyway to conclude that the C7_ PM has an enhanced temperature sensitivity with respect to the other fibers. These characteristics possibly make this fiber suitable for sensors applications. Possible candidate PM fiber suitable for this technology can be the fiber recently demonstrated in [26] or in [27]. The *defects* introduced in the cladding structure make these fibers PM without introducing additional surface modes which could affect the FM. In this sense, one of these fiber could also help to discriminate the source of the instability here observed on the C7_ PM.

4.3. Overall comparison

Considering the overall performances, the C7_ S fiber is the most suitable for the frequency standard applications, showing a fractional frequency instability $\leq 8 \times 10^{-12}$ in a *stressed* environment and better performance in a controlled one ($\sigma(\tau) < 4 \times 10^{-12}$, $1 < \tau < 10^4$ s timescale). The C7_ S fiber is also tested over 55 hrs (in a temperature stabilized environment), in order to compare the instability of the system developed here with previously published results. Fig. 5 (left) compares the performance of the C7_ S fiber with the stabilized laser presented in [12] (gas-filled kagome fiber) and with the performance of the reference laser [7]. The lowered instability achieved with respect to [12] is reducing the gap between the bulk cell performance and the HC-fiber based system. The lock-point repeatability is also measured on 6 different days (Fig. 5, right): the system shows an average shift of 3.6 kHz with respect to the reference, with a standard deviation of 2.5 kHz. This analysis of the *long-term* performance shows a consistent result over a period of more than 1 year.

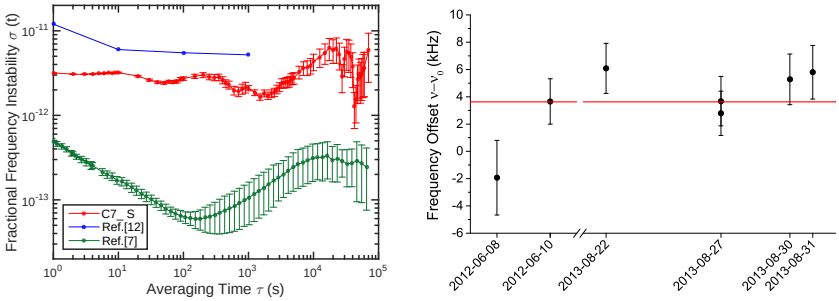

Fig. 5. Left: Summary of the performance achieved using the C7_S fiber in a temperature stabilized environment (red). The system is compared with the reference laser [7] stabilized to a bulk glass cell (green) and with the best performance reported in [12] for an gas-filled HC-fiber stabilized laser (blue). Right: The lock-point repeatability over 7 measurements. The error bars represent the root mean square value of the measured data.

5. Modelling of HOMs

In order to understand how the different modes could influence the frequency of locked laser, a numerical investigation on the mode content is performed. The C7_L fiber has similar properties to that of C7_S, nonetheless the C7_L results in a larger variation of the laser frequency. We believe the reason is the presence of HOMs at the addressed wavelength as highlighted by the measurements in Fig. 1. For this reason fiber C7_L is chosen for the numerical investigation. The purpose of this analysis is to address the mode(s) that could be responsible of the frequency shift/fluctuation observed. The simulations are performed starting from an idealized model of a 7-cell HC-PCF structure, using the parameters measured on the cane during the fiber drawing process, according to [28, 29]. Results are shown in Fig. 6.

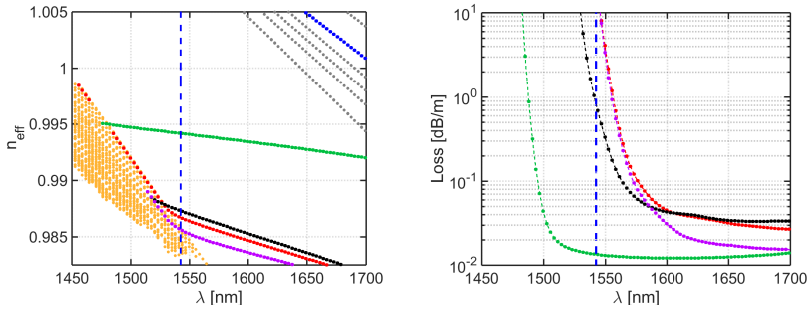

Fig. 6. Simulation results of C7_L. The mode trajectories (left) and the loss of the different modes (right) are plotted. The FM is plotted in green, the cladding modes in orange and the surface modes in grey. Three HOMs (red, violet and black dots) and a surface mode (blue) are highlighted. A dashed blue line at 1542 nm is added. The surface modes on the left figure are omitted for clarity.

The FM and the relevant HOMs/surface modes are highlighted. The loss data plotted is limited to the 10 dB/m for clarity. Remembering that the tested fibers have a length of 3 m, Fig. 6 (right) can also represent the transmission of the different modes through the fiber: 10^{-2} dB/m

corresponds to 99% while 10 dB/m gives 0.1% of transmission. Therefore, the simulations show that only one HOM has a loss low enough to be detected (black curve).

5.1. Simulated and measured spectrum comparison

A direct comparison between simulated and measured spectrum requires the calculation of the group refractive index (n_g) of the simulated modes

$$n_g = n_{\text{eff}} - \lambda \frac{dn_{\text{eff}}}{d\lambda} \tag{1}$$

where λ is the wavelength and n_{eff} is the effective refractive index. The group index difference with respect to the FM (Δn_g) superimposed on the spectrogram of the C7_L fiber from Fig. 1 is presented in Fig. 7. The intensity profiles are also plotted to clarify the difference between the modes.

The simulations reproduce quite well the measured mode content and they confirm that the features with a lower group index difference (less than 0.05) are HOMs excited in the fiber, while the strong feature observed at $\Delta n_g \sim 0.12$ that covers most of the band gap is a surface mode (or a combination of many of those). The simulations also confirm that the flat feature at $\Delta n_g \sim 0.08$ is not caused by any HOM/surface mode. Since the simulation of the surface modes is strongly dependent on the accuracy of the description of the structures surrounding the core wall, the numerical evaluation of the surface modes is less trustworthy than the HOMs one. A deeper investigation (using e.g. SEM/AFM images) is necessary to have a better knowledge of the geometry that surrounds the core, in order to obtain a more reliable simulation of surface modes.

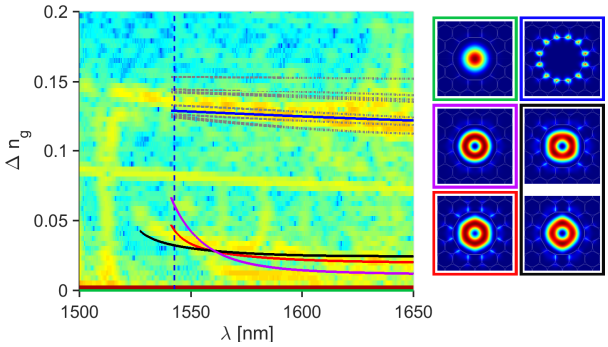

Fig. 7. The group index evaluation of the various modes is compared with the experimental data of the fiber C7_L from Fig. 1 (left). The colors are the same used in Fig. 6. The FM is visible at $\Delta n_g = 0$ (green). The intensity profile of the different modes simulated is plotted (right). The HOM represented in *black* is in fact the superposition of two different modes, as highlighted by the mode intensity profiles on the right.

6. Laser frequency shift: a simple theoretical approach

The frequency shift observed in the multi-mode fibers presented in Fig. 3 needs to be explained. Any change in one of the fundamental parameters that defines the light-matter interaction can (potentially) cause a shift in the lock-point frequency. Wave front curvature [30] and angled

beams interaction [31] are known to cause frequency shift in SAS with bulk vapour cells. However, these effects cannot directly explain frequency shifts when using HC fiber as gas cell. The wave-front curvature in the HC fiber is negligible (plane wave) and the beams are confined along the same propagation path (the counter-propagating k-vectors are aligned).

Temperature effects are already discussed in Section 4. The pressure variation is below 0.5 Pa over the entire test and it has negligible influence. The probe and pump power are monitored along the tests, showing fluctuations of 0.05 mW and 0.3 mW respectively (one standard deviation). The numerical value of the power sensitivity coefficient is measured to be below 15 kHz/mW for both the beams. Therefore, the observed power fluctuations combined with the power sensitivity cannot explain the $\pm$ 25 kHz frequency fluctuations observed for the multimode fibers. However, a correlation between the the frequency fluctuations for the C7_ PM fiber and spatial mode variations of the probe/pump beam is observed. An infrared camera monitors a small fraction of the probe beam, and the beam shape oscillates about 50 times when the temperature is increased by 5°C. This compares qualitatively to the number of frequency oscillations for a 5°C temperature change as seen in Fig. 4. Similarly, if a small misalignment is introduced so that the output power at the fiber facet changes less than 1%, the mode shape clearly oscillates. These observations suggest that fluctuations in the modal content are responsible for the observed frequency fluctuations.

Previously published work [12] reports a frequency shift in large core kagome fibers (diameter $\sim 60\ \mu$m) comparable to the one presented here. According to [12] various spatial modes could cause a shift comparable to the Doppler shift observed in a free space interaction of two angled beams. Although the Doppler effect should give a theoretical shift of few MHz, they argue that the interaction between many HOMs should average out, reducing the final shift to the kHz level. We demonstrate that this explanation is not generally sufficient. Observing Fig. 6 and 7, only one mode has a low enough loss to be taken into account (black curve), but the maximum shift observed for the C7_ L fiber is only $\pm$50 kHz with respect to the reference [7]. Hence we observe a small shift at the kHz level which cannot be explained by an averaging of many HOM interactions. We aim to present here a simple theoretical model that describes the mechanism involved in the frequency shift for the different types of HC fibers, also in case of a HC fiber that guides *few* modes at the addressed wavelength, like the C7_L considered.

The mechanism is based on the Doppler shift effect, taking into account the intensities associated to the different modes. In order to keep the theoretical model simple, only two modes are considered for the C7_ L fiber: the FM and the HOM with the lower loss (Fig. 6, black). The two counter-propagating beams (pump and probe) can be described as a superposition of the FM and the HOM component. Therefore, the (pump,probe) interaction could be decomposed in four different contributions due to the modal content of each beam: (FM,FM) + (FM,HOM) + (HOM,FM) + (HOM,HOM). Each contribution is treated separately and the single effects are subsequently summed, which is possible as the modes are orthogonal. In general, in order to saturate the molecules, the k-vectors of the two laser beams should fulfill the following expression

$$\mathbf{k_i} \cdot \mathbf{v} = \mathbf{k_j} \cdot \mathbf{v} \tag{2}$$

where $i = 1,2$ and $j = 3,4$ refers to the probe and pump components respectively (as labeled in Fig. 8), while $\mathbf{v}$ is the velocity of the molecules addressed by the two beams.

Since the k-vector component along the propagation axes depends on the effective refractive index of the mode considered, the interaction inside the fiber is the analogue of an angled beam interaction in a vapour bulk cell. Inside the HC fibers, the shift is not caused by a *real* angle between the counter propagating k-vectors, it is given by an *effective angle* that comes from the different propagation constant (β_i) of the modes. The *effective angle* (θ_i) of each mode

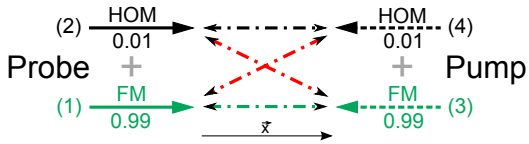

Fig. 8. Schematic representation of the light-matter interaction. The green arrows indicate the FM, the black ones the HOM component. The interactions are depicted with dotted-dashed line in green (FM-FM), red (FM-HOM and HOM-FM) and black (HOM-HOM). The number reported under each mode component refers to the associated normalized light intensity. The components are also enumerated for clarity. The axis orientation chosen is shown.

considered can be defined as follow

$$\begin{cases} \beta_{\mathbf{i}} = n_{\mathrm{eff}_i} k_0 \hat{\mathbf{x}} \\ \beta_{\mathbf{0}} = n_0 k_0 \hat{\mathbf{x}} \end{cases} \implies \cos\theta_i = \frac{n_{\mathrm{eff}_i}}{n_0} \implies \begin{cases} \theta_{1,3} = 0.11 \\ \theta_{2,4} = 0.16 \end{cases} \tag{3}$$

where n_0 and k_0 are the refractive index and the wave number in vacuum, and $\beta_i = n_{\mathrm{eff}_i} k_0$ is the propagation constant associated to the different modes. Rewriting the Eq. (2) with the effective angles defined in Eq. (3), the Doppler shift ($\Delta\nu_{ij}$) of the different interaction is given by

$$k_0 \begin{bmatrix} \cos\theta_i \\ \sin\theta_i \end{bmatrix} \cdot \begin{bmatrix} v_x \\ v_y \end{bmatrix} = k_0 \begin{bmatrix} \cos(\pi+\theta_j) \\ \sin(\pi+\theta_j) \end{bmatrix} \cdot \begin{bmatrix} v_x \\ v_y \end{bmatrix} \implies \Delta\nu_{ij} = \frac{v}{\lambda_0} \sin\left(\frac{\theta_j - \theta_i}{2}\right) \tag{4}$$

where the angle π gained by the pump components is due to the fact that the pump is propagating in the opposite direction with respect to the probe (Fig. 8), and $v = \sqrt{v_x^2 + v_y^2}$ is the thermal velocity of the molecules (≈ 435 m/s). Therefore, the contribution to the shift can *only* be due to the interactions between a FM and a HOM component. Moreover, when the $\theta_j > \theta_i$ the center of the sub-Doppler line shape experience a positive shift, while a negative shift occurs if $\theta_j < \theta_i$. This fact gives rise to an opposite contribution from the two FM-HOM interactions: the (2,3) interaction addresses a class of molecules with a velocity component $+v_x$ (same direction of the probe beam, $\beta_2 < \beta_3$), while the (1,4) interaction addresses a class of molecules with a velocity component $-v_x$ (opposite direction, $\beta_1 > \beta_4$). The *theoretical* shift $\Delta\nu_{ij}$ given by Eq. (4) is approximately +7 and -7 MHz for the (1,4) and (2,3) interactions respectively, and zero otherwise (for the C7_L fiber considered).

In order to take into account the light intensity of the various interaction, we define f_i as the normalized intensity associated to each mode. The light intensity associated to the each interaction is defined as $I_{ij} = f_i \cdot f_j$, $i = 1,2$ and $j = 3,4$, assuming that the pump/probe have the same power at the fiber input. Therefore, the line-shape $I(\nu)$ of the sub-Doppler absorption line will be the superposition of four interactions

$$I(\nu) \propto \sum_{i=1}^{2} \sum_{j=3}^{4} \frac{I_{ij}}{4\pi} \frac{\Gamma_0}{(\nu - \nu_0 \pm \Delta\nu_{ij})^2 + \left(\frac{\Gamma_0}{2}\right)^2} \tag{5}$$

where Γ_0 and ν_0 are the FWHM and the frequency of the sub-Doppler transition addressed. Taking into account the transit-time and the pressure broadening effect, the FWHM for the fiber considered is $\Gamma_0 \approx 26$ MHz [20, 21]. Depending on the I_{ij}, $\Delta\nu_{ij}$ and Γ_0, the maximum of the line-shape $I(\nu)$ could experience a *shift* ($\Delta\nu_{\mathrm{TOT}}$). In fact, the *shift* of the maximum of the line-shape $I(\nu)$ is a distortion of the typical Lorentzian profile caused by the superposition of

four interactions not centered on the same frequency. Therefore, the fact that the shift observed is limited to the kHz level is due to the combination of the symmetry of the pump/probe configuration and the low intensity associated to the HOMs (with respect to the FM one). This *shift* directly affects the laser frequency, because it changes the zero-crossing point of the dispersion-like signal used for locking.

In order to simplify the analysis of the model predictions, we assume the following light intensity of the mode components:

- 1% of light coupled to the HOM component ($f_{2,4} = 0.01$);
- 99% of light coupled to the FM component ($f_{1,3} = 0.99$);

This light intensity configuration is not arbitrary and it could be considered as an upper limit: the WFT analysis on the C7_ L fiber (Fig. 1) shows that the HOM considered (black) has an intensity more than 50 times lower than the FM (after 8 cm of fiber, at 1542 nm) and the HOM considered has 3 dB loss across the fiber tested, which further reduces the average intensity coupled to the the HOM component (by a factor ≈1.5). Therefore, limiting to a few percent the light intensity associated to the HOM components is a reasonable assumption. Therefore, the derivation of the line-shape $I(\nu)$ described by Eq. (5) allows some considerations:

1. If the light intensity distribution between the pump and probe components is symmetric (Fig 8), the maximum of $I(\nu)$ experiences a total shift of $\Delta\nu_{\mathrm{TOT}} = 0$, even in the few-mode fiber described. *Only* an asymmetric distribution between the pump/probe HOM components can cause a shift, which is incidentally the most probable situation that experimentally occurs.

2. In presence of intensity fluctuations that breaks the symmetry, since $\Gamma_0 > \Delta\nu_{ij}$, the maximum of the line-shape $I(\nu)$ can be shifted by $\Delta\nu_{\mathrm{TOT}} = \pm 40$ kHz, depending on the modal content of the pump/probe beams: if only the pump beam has light in the HOM component ($f_1 = 1,\ f_2 = 0,\ f_3 = 0.99,\ f_4 = 0.01$) the shift predicted is +40 kHz, while a -40 kHz shift occurs in the opposite configuration ($f_1 = 0.99,\ f_2 = 0.01,\ f_3 = 1,\ f_4 = 0$). An oscillation (over time) between these two configurations reproduces quite well the offset frequency fluctuations presented in Figures 3 and 4 (C7_ L, maximum shift observed ± 25 and ± 50 kHz, respectively).

3. A detailed analysis of the line-shape derived in Eq. (5) shows that once fixed Δn_{eff} and I_{ij}, if Γ_0 decreases the shift experienced by the maximum of $I(\nu)$ will decrease as well. Moreover, if $\Delta\nu_{ij} \geq \Gamma_0$, the HOM-FM interaction will not affect the maximum of $I(\nu)$, because signal generated will be far-detuned from optical transition addressed. Therefore, if the interaction between the HOM and the FM considered so far occurs in a fiber with core size larger than the C7_ L one, the shift produced will be smaller compared to the one here observed/calculated. This property can explain the relative *small* shift observed in [12]: the wider core of the kagome fiber helps to reduce the total frequency shift ($\Delta\nu_{\mathrm{TOT}}$), even if the Δn_{eff} between the HOMs guided in the kagome fiber (and the relative light intensity associated) could easily exceed the one considered in the calculation at point 2.

4. The frequency shift is *coupling* dependent, because a misalignment could easily increase the light intensity coupled to the HOM components. This effect is confirmed by the C19 fiber performance under temperature perturbation (Fig. 4, left): a continuous temperature variation *breaks* the modal content *symmetry*, increasing the maximum shift to ± 120 kHz.

5. The long term oscillations experienced by the C7_PM fiber (Fig. 3, left) could also be described by the mechanism presented here, considering that the two orthogonal polarized FMs have an effective refractive index difference much smaller than the one observed for the (FM,HOM) interaction described above. A smaller effective refractive index difference will reduce the maximum theoretical shift, but the intensity coupled to the orthogonal polarized FMs could easily fluctuates over 1% due to coupling misalignment, compensating the reduction.

7. Conclusion

An optical frequency standard is developed using gas-filled single-mode HC-PCF with a core size diameter of 8 μm. A complete experimental investigation of four HC fibers is done to characterize the performances. Despite the previous recommendations, the fiber with a core diameter of only 8 μm shows a high accuracy and low fractional frequency instability (below 4×10^{-12} for averaging time between 1 s and 10^4 s). The frequency of the lock point is repeatable to ± 2.5 kHz (standard deviation over 7 measurements), resulting in the most stable and accurate laser systems locked to an acetylene filled HC fiber published so far [12, 15, 16]. This performance combined with a low temperature sensitivity and a negligible HOMs content make the C7_S fiber a good candidate for a portable optical frequency standard. Furthermore, a simple theoretical description of the mechanism involved in the frequency shift of the locked laser is presented. The model describes the light-matter interaction with a good agreement with the experimental data, helping to select the more suitable fiber for frequency standard applications. Future investigations on the fiber crystal structure is necessary to evaluate the role of the surface modes in the energy exchange with HOMs, as well as a complete description of polarization effects.

Acknowledgments

The presented work is made possible by the Marie Curie Initial Training Network *QTea - Quantum Technology Sensors and Applications,* financed by the FP7 program of the European Commission (contract-N MCITN-317485). This work was also funded by the European Metrology Research Programme EMRP (JRP IND14 Frequency). The EMRP is jointly funded by the participating countries within EURAMET and the European Union.

Appendix I. List of Publications and Submitted Manuscripts

Paper II

Interference Cancellation for Hollow-Core Fiber Reference Cells

J. Seppä, M. Merimaa, A. Manninen, M. Triches, J. Hald and A. Lassila

IEEE TRANSACTIONS ON INSTRUMENTATION AND MEASUREMENT, Vol. 64, No. 6, June 2015

[a] In reference to IEEE copyrighted material which is used with permission in this thesis, the IEEE does not endorse any of DTU's products or services. Internal or personal use of this material is permitted. If interested in reprinting/republishing IEEE copyrighted material for advertising or promotional purposes or for creating new collective works for resale or redistribution, please go to
http://www.ieee.org/publications_standards/publications/rights/rights_link.html
to learn how to obtain a License from RightsLink.

Interference Cancellation for Hollow-Core Fiber Reference Cells

Jeremias Seppä, Mikko Merimaa, Albert Manninen, Marco Triches, Jan Hald, and Antti Lassila

***Abstract*— Doppler-free saturated absorption spectroscopy of gases in hollow-core fiber (HCF)-based cells can be used for realizing new compact, robust, and portable frequency standards. In this paper, methods for cancelling interferences resulting from the optical connections between standard fiber and HCF and other factors such as varying coupling to HCF modes are investigated. Laser power modulation with simultaneous detection of ac and dc signal is used to separate saturated absorption from interferences. In addition, a technique of two piezoelectric stack actuators stretching the fiber at different locations is described. The presented experimental results demonstrate that 99% interference attenuation is readily attainable with the techniques. Frequency comb-referenced measurement of saturated acetylene absorption features near 1.54 μm, with fiber length and power modulation, is presented. For comparison, measurements and results of the same acetylene fiber, using a system having pump and probe beams at mutually shifted frequencies, are also given.**

***Index Terms*— Frequency measurement standards, infrared spectra, interference cancellation, measurement techniques, metrology, optical fiber, spectroscopy.**

I. Introduction

SATURATED absorption spectroscopy usually requires beams of light passing through low-pressure gas in opposite directions along the same optical path, enabling observation of the center of the spectral transition without Doppler broadening. Using a hollow-core fiber (HCF)-based gas cell [1], [2] in an all-fiber arrangement improves robustness against optical misalignment, mechanical vibration, and temperature changes.

However, interference arising from interfaces between the optical components can be a severe problem. In traditional free-space optical arrangements for spectroscopy and laser stabilization, interference can be attenuated by dithering the end mirror [3]–[5] or by having the pump and probe light beams crossing at a small angle instead of following the same optical path, causing also a shift to the measured spectrum. However, with the HCF cell it is not usually possible to reflect light back directly from the end of the cell nor to have the pump and probe beams at an angle. Introducing the light into the HCF at both ends by, e.g., having the HCF spliced between telecom fibers produces optical interfaces that can have high reflectivities and losses. Using, e.g., the end mirror and HCF-based arrangement results in complex interference effects from multiple optical interfaces and possibly also effects due to the mode structure of the fiber.

An alternative to using pump and probe light at the same wavelength is having the two light beams with a mutual frequency shift. This has been successfully used for cancelling majority of the interference effects by shifting the interference of the pump and probe light in the interfaces from dc to, e.g., megahertz range frequencies [1], [2]. Using pump and probe light at different wavelengths leads to a somewhat more complicated system, and in principle, attenuates a different subset of the possible interference effects.

In this paper two different methods to attenuate interference effects in HCF-based systems with an end mirror are investigated. First, a piezo modulation scheme, published in [6], using two piezos modulating both the HCF and the end mirror is shown to greatly reduce the interferences in a carbon dioxide-filled fiber spliced between standard single-mode fibers. Second, a method using laser power modulation and ac/dc detection is shown to be able to differentiate the nonlinear saturated absorption from the linear interference and linear absorption to a high degree in a low-pressure acetylene-filled fiber. The dc component of detector signal is detected in both setups using a digital voltmeter (DVM), and in the latter method the ac component is detected using a lock-in amplifier.

The acetylene-filled fiber component used in the latter experiment was made by Danish Fundamental Metrology (DFM), and has coupling lenses at both ends of the HCF. The laser frequency in the latter experiment is locked to atomic clock via frequency comb [7]. The comb repetition rate is stepped to scan the locked laser frequency.

As a third measurement method, recent results with the same HCF cell, using pump and probe light at different frequencies [8] are shown for comparison.

A. Setup With Two Modulating Piezos

The setup for the experiment, shown in Fig. 1, is partly based on previously designed instrumentation [4] that used a bulk glass reference gas cell instead of hollow-core fiber. It comprises an external cavity diode laser (ECDL),

Manuscript received August 22, 2014; revised January 21, 2015; accepted February 10, 2015. This work was supported by the European Metrology Research Programme (EMRP), JRP IND14 Frequency. The EMRP is supported by the participating countries within EURAMET and the European Union. The Associate Editor coordinating the review process was Dr. Lucas Di Lillo.

J. Seppä, M. Merimaa, A. Manninen, and A. Lassila are with the Centre for Metrology MIKES, VTT Technical Research Centre of Finland, Espoo FI-02151, Finland (e-mail: jeremias.seppä@mikes.fi; mikko.merimaa@mikes.fi; albert.manninen@mikes.fi; antti.lassila@mikes.fi).

M. Triches is with Danish Fundamental Metrology A/S, Kgs. Lyngby DK-2800, Denmark, and also with the Department of Fotonik Engineering, Technical University of Denmark, Kgs. Lyngby DK-2800, Denmark (e-mail: mt@dfm.dk).

J. Hald is with Danish Fundamental Metrology A/S, Kgs. Lyngby DK-2800, Denmark (e-mail: jha@dfm.dk).

Color versions of one or more of the figures in this paper are available online at http://ieeexplore.ieee.org.

Digital Object Identifier 10.1109/TIM.2015.2408800

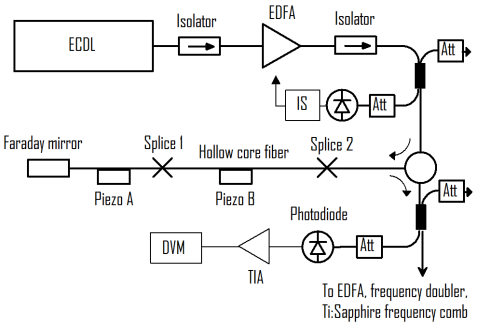

Fig. 1. Measurement setup for feasibility tests using a hollow core fiber gas cell. Att is an attenuator, IS is the intensity stabilizer, and TIA is a transimpedance amplifier.

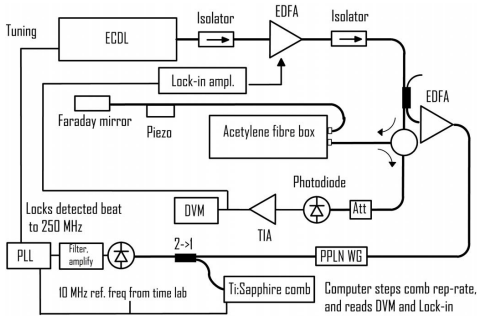

Fig. 2. Measurement setup using low-pressure acetylene-filled hollow core fiber gas cell and laser power modulation. Att is the attenuator, and TIA is the transimpedance amplifier. PLL is phase-locked loop electronics and PPLN WG is periodically poled lithium niobate waveguide.

an erbium-doped fiber amplifier (EDFA), intensity stabilization, HCF, Faraday mirror and circulator, detection, and two piezo stacks. The HCF is an approximately 40-cm long photonic crystal HCF and is spliced to telecom fiber at both ends. In addition to high reflectivity, the splices had high losses. The two piezo stacks, A and B, were glued to the telecom fiber between mirror and splice one, and to the HCF, using a cyanoacrylate glue. The outer protective layers of the telecom fiber were removed before gluing to facilitate stretching.

Piezo A and piezo B were driven by two separate, synchronized signal generators. A triangular waveform at 50 Hz was used for modulating the piezos. This frequency is the local mains frequency and is effectively averaged out by the DVM. Such a low frequency also resulted in good relative sharpness of the turning points of the motion of the piezos. Generally, a more robust choice would have been using a frequency different from the mains frequency with a suitable DVM time constant. However, the system was operable at similar performance level also with, e.g., a 60-Hz piezo modulation.

By looking at the interference fringes in the detected signal with an oscilloscope, the amplitudes were tuned in such a way that each piezo oscillated over an integer number of interference fringes and the relative phase of the signals was tuned in such a way that the piezos changed direction simultaneously. Therefore, the part of the interference effects dependent on the combined stretching effect of both piezos also spread over an integer number of fringe periods. In this experiment piezo A was modulated over a few fringes and piezo B was modulated over a single fringe period. Therefore, the fringe frequencies were also different, helping to further spread the combined interference effects evenly for averaging.

The DVM was used in dc mode and averaging time was 200 ms, effectively averaging the 50-Hz modulation. Stepping of the ECDL wavelength setting was done at 1-s intervals.

B. Setup With Laser Power Modulation

The setup with laser power modulation and frequency comb locking is shown in Fig. 2. The acetylene-filled fiber is situated inside the box denoted as acetylene fiber box. The box has Ferrule Connector/Angled Physical Contact connectors and connecting telecom fibers. The HCF used is a seven-cell photonic crystal fiber with a core diameter of 8 μm and a length of 2.8 m. The acetylene filling pressure has been estimated as 12 Pa, but a pressure increase of approx. 15 Pa/month has been observed due to air leak. All the measurements presented here have been performed within six months of filling.

One fiber length modulating piezo was used at the fiber leading to the end mirror to reduce large (approximately 5% amplitude compared with off-spectrum mean intensity) short-period interferences.

A lock-in amplifier (SRS type 830) was used to provide 333-Hz modulation signal to the pump laser of the first EDFA. The resulting power modulation in the EDFA output was approximately 50% of the mean power. The frequency of the lock-in amplifier was selected in such a way that the detection of the lock-in frequency would not detect much undesired signal from the piezo modulation at 50 Hz. The averaging time constant in the lock-in amplifier was 100 ms. The mean power entering the acetylene fiber box was approximately 10 mW. The second EDFA was added to the system to amplify the power fed into the frequency-doubling crystal, periodically poled lithium niobate waveguide, for higher output power.

The wavelength of the ECDL was tuned close to the measured acetylene transition and then locked to the titanium-sapphire frequency comb via the frequency doubling and using phase-locked loop-type electronics [4]. The wavelength scan was done by stepping the pulse repetition rate of the frequency comb system.

C. Setup With Two Different Wavelengths and Pump Power Modulation

The setup with two different wavelengths for the pump and probe beam is shown Fig. 3. The light provided by the fiber laser (NKT Photonics E15) is split in a 50/50 fiber-splitter. Two acousto-optic modulators (AOMs) are used to blue-shift the light respectively 40 MHz (probe) and

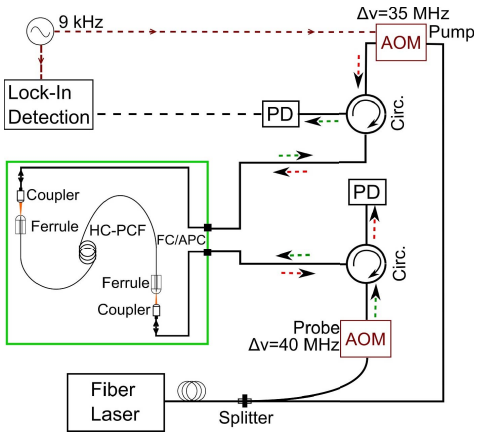

Fig. 3. Measurement setup using two different counter-propagating wavelengths ($\Delta\nu = 5$ MHz) in the hollow core fiber gas cell. The two AOMs shift the laser frequency in the same direction to maintain the sub-Doppler resonance close to the bottom of the Doppler absorption line, where the S/N is higher.

35 MHz (pump). The pump beam is also modulated 100% in intensity by applying a 9-kHz square wave to the pump AOM. This 9-kHz signal is used as external reference for the lock-in amplifier (SRS830). Two circulators are used to monitor both the transmitted probe and the pump using two photodetectors (PD). The frequency is controlled by offset-locking of the laser to a second acetylene stabilized laser described in [8]. The acetylene-filled fiber is the same as the one shown in Fig. 2. The typical pump/probe power used is 5 mW.

II. Saturation and Power Modulation

The nonlinearity of the saturation phenomenon can be exploited to differentiate true saturated absorption features from the linear absorption and interference.

For any linear loss in the setup, the ac/dc ratio remains constant, thus effectively eliminating variations arising from interference. When a gas absorber is introduced to the system, the power response becomes nonlinear and saturation can be seen through the ac/dc ratio, as can be seen from Fig. 8. This method faithfully recovers the usual Doppler-free shape of the lamb dip on Doppler-broadened background. However, the curvature of the background is in the opposite direction, compared with the traditional transmission signal. We also note that harmonic distortion of the power modulation can be used as an indicator of nonlinear response due to saturation, but this was not investigated in this paper.

III. Results

A. Two-Piezo Modulation

Fig. 4 shows the recorded detector signal as DVM readings over a wavelength scan with and without the

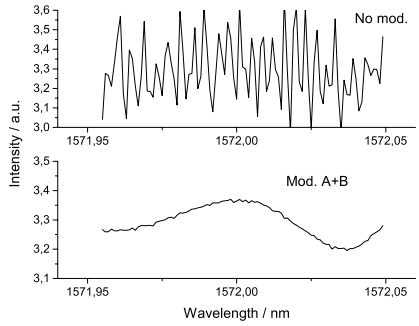

Fig. 4. Recorded intensity at detector over a wavelength scan in arbitrary units. Upper graph is without piezo modulation and lower is with both piezos on. The remaining shape is a combination of CO_2 absorption spectrum and interference effects. CO_2 has an absorption at 1572.02 [R(18) rotational line associated with $[00^00] \rightarrow [30^01]$ vibrational transition]. The wavelength scale is approximate in this experiment.

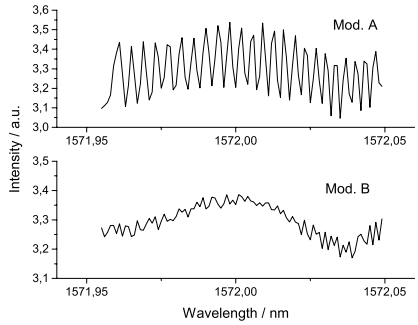

Fig. 5. Recorded intensity over a wavelength scan, with only one piezo A (upper graph) or B (lower graph) modulated.

piezo modulations. The HCF used in this experiment was filled with CO_2 at atmospheric pressure.

Fig. 5 shows the corresponding scan with only piezo A or B modulated. Clearly, neither of modulations is sufficient by itself to cancel the interference out.

In the absence of any modulation, the amplitude of the interference features varied between approximately 20% and 80% of the signal mean.

B. Laser Power Modulation

Fig. 6 shows the directly measured dc-coupled detector signal as a function of laser frequency. From scan to scan, the distorted, asymmetric form varied so that the extent and direction of the slant varied. The piezo modulation of the end mirror removed short-period interferences quite effectively but there was still a distorted shape of absorption. To avoid gluing a second piezo to the HCF, an alternative method, i.e., the power modulation scheme, was applied.

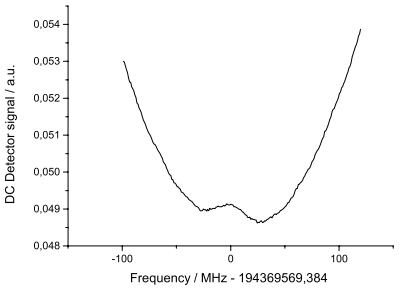

Fig. 6. Recorded dc signal in the scan over the acetylene P16 line.

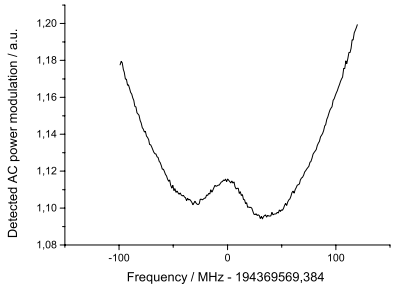

Fig. 7. Recorded ac signal in the scan over the acetylene P16 line.

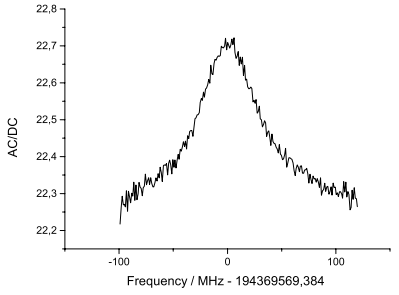

Fig. 8. AC/dc ratio in the scan over the acetylene P16 line.

The comb repetition rate was stepped at approximately 1-s intervals, with approximately 200 measurement points in a single scan. The 1 s wait consisted mainly of waiting for the DVM and lock-in reading to stabilize before reading. All data in Figs. 6–9 are from a single scan.

Fig. 7 shows the ac component detected with the lock-in amplifier simultaneously with the dc component. The Lamb dip is more pronounced due to the nonlinear power response of the saturable medium, although it is still highly distorted.

Fig. 8 shows the ac signal normalized by dividing it by the dc signal. The lamb dip feature is more symmetric, protruding from the Doppler-broadened shape. The ac and dc signals are measured simultaneously from the same scan.

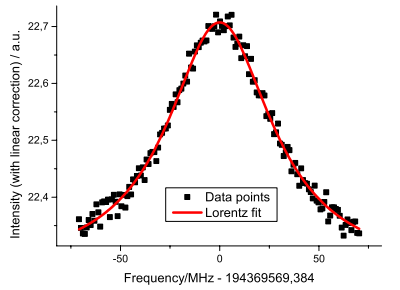

Fig. 9. AC/dc ratio in the central part of the scan over acetylene P16 line with Lorenz fit. A fitted line has been subtracted before the Lorenz fit.

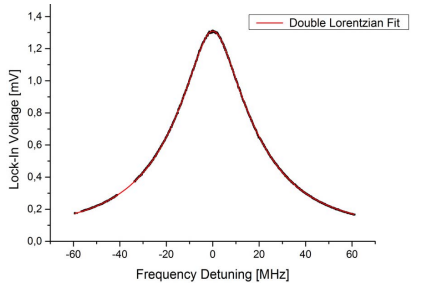

Fig. 10. Lock-in detected sub-Doppler resonance. The data are plotted shifted by 2.5 MHz, because of the different frequency shifts from the two AOMs. The missing of data at −37.5 MHz is due to an instability of a counter reading at a zero-crossing point.

In Fig. 9 the center part is first processed by just subtracting a fitted line to remove the small remaining tilt seen in Fig. 8. Then a Lorentzian function was fitted. The center wavelength of the fit in the figure shown differs from the reference value for low-pressure bulk glass cells only by less than 1 kHz. However, in five repeated experiments, the variation in the fitted central frequency was approximately 200 kHz, and the mean value within 100 KHz of the bulk-cell reference value. The corresponding graphs of the other scans were similar in shape, with slightly changing noise and interference levels probably due to drifting of measurement parameters. The variation of the fitted central frequency is possibly mainly due to the limited number of data points that we were able to measure, compared with the measurement noise level. The majority of the fitted central frequencies were higher than the bulk cell reference value.

C. Comparison With the Two Different Wavelengths Method

Fig. 10 shows the lock-in amplifier output when demodulating the signal acquired by the PD with the external reference frequency (9 kHz). The frequency of the laser is stepped by 100 KHz over a 120-MHz frequency range. Five data points are acquired per frequency step with a lock-in integration time of 100 ms. A delay time of 100 ms has been set

at the beginning of every single step due to the response time of the offset-locking setup. The total acquisition time is about 12 min.

The data in Fig. 10 are fitted with a sum of two Lorentzian functions with individual linewidths and amplitudes but identical center frequencies. This empirical line shape is chosen to include the increased contribution from the slow molecules inside the fiber [1]. At low pressure and low optical power, slow molecules provide a narrow contribution to the signal. The faster molecules have a higher interaction rate with the core wall, destroying the coherence in the light matter interaction and broadening their contribution to the signal. The fit shows a center frequency blue-shifted by approximately 50 kHz. Eight repeated measurements show an average shift of 19 KHz with a standard deviation of 20 kHz. The full-width at half-maximum linewidth is (39 ± 0.4) MHz. The pressure broadening due to the leak of the cell must be considered when compared with the measurements of Figs. 6–9. According to measurements by DFM, the linewidth should be approx. 46 MHz at the time when tests presented in Figs. 6–9 have been performed. The leak-rate observed is under investigation to evaluate the long-term stability of the fiber-filled reference. A complete performance evaluation of the system will be presented in a future work, including a pressure stability characterization.

IV. Conclusion

The presented measurement methods provide tools for interference cancellation in HCF-based reference gas cells, and the ac/dc method could also be used to cancel interference in various other saturated absorption measurements. Detection of saturated absorption in HCF cell was shown to be possible without having the pump and probe beams at different frequency. The results suggest that repeatability in the measuring of transition center frequency is possible at least 100 kHz level with acetylene-filled HCF cells, using different measurement techniques.

References

[1] J. Hald, J. C. Petersen, and J. Henningsen, "Saturated optical absorption by slow molecules in hollow-core photonic band-gap fibers," *Phys. Rev. Lett.*, vol. 98, no. 21, pp. 213902-1–213902-4, 2007.

[2] *New Generation of Frequency Standards for Industry*. [Online]. Available: http://projects.npl.co.uk/frequencystandards/, accessed Jan. 24, 2014.

[3] J. A. Silver and A. C. Stanton, "Optical interference fringe reduction in laser absorption experiments," *Appl. Opt.*, vol. 27, no. 10, pp. 1914–1916, May 1988.

[4] V. Ahtee, M. Merimaa, and K. Nyholm, "Precision spectroscopy of acetylene transitions using an optical frequency synthesizer," *Opt. Lett.*, vol. 34, no. 17, pp. 2619–2621, Sep. 2009.

[5] V. Ahtee, M. Merimaa, and K. Nyholm, "Fiber-based acetylene-stabilized laser," *IEEE Trans. Instrum. Meas.*, vol. 58, no. 4, pp. 1211–1216, Apr. 2009.

[6] J. Seppä, M. Merimaa, A. Manninen, and A. Lassila, "Interference cancellation for hollow-core fiber reference cells," in *CPEM Dig.*, 2014, pp. 672–673.

[7] M. Merimaa, K. Nyholm, M. Vainio, and A. Lassila, "Traceability of laser frequency calibrations at MIKES," *IEEE Trans. Instrum. Meas.*, vol. 56, no. 2, pp. 500–504, Apr. 2007.

[8] J. Hald, L. Nielsen, J. C. Petersen, P. Varming, and J. E. Pedersen, "Fiber laser optical frequency standard at 1.54 μm," *Opt. Exp.*, vol. 19, no. 3, pp. 2052–2063, Jan. 2011.

Jeremias Seppä received the M.Sc. and Ph.D. degrees from Aalto University, Espoo, Finland, in 2007 and 2015, respectively. His Ph.D. dissertation was on nanometrology and interferometry.

He is a Senior Scientist with the Length Metrology Group, Centre for Metrology and Accreditation, VTT Technical Research Centre of Finland, Espoo. He has been involved in computer science, mathematics, machine learning, measurement, and laser physics. His current research interests include laser frequency, nanometrology, and interferometry.

Mikko Merimaa was born in Helsinki, Finland, in 1972. He received the M.Sc. and Ph.D. degrees from Aalto University, Espoo, Finland, in 1997 and 2001, respectively. His dissertation was on frequency standards based on diode lasers.

He held a two-year post-doctoral position with Aalto University. He joined the Centre for Metrology and Accreditation, where he was the Leader of the Time, Frequency and Spectroscopy Group. He is currently a Research Manager with the Centre for Metrology and Accreditation, VTT Technical Research Centre of Finland, Espoo. His current research interests include time and frequency, optical clocks, and spectroscopy.

Albert Manninen, photograph and biography not available at the time of publication.

Marco Triches was born in Belluno, Italy. He received the master's degree in physics from the University of Padua, Padua, Italy, in 2012. He is currently pursuing the Ph.D. degree with DTU Fotonik, Kgs. Lyngby, Denmark.

He focused on experimental physics, taking his thesis project abroad, with DTU Nanotech, Kgs. Lyngby, Denmark, during his studies. In the group of Prof O. Hansen, he fabricated and studied the physics beyond the electret-based energy harvester, developing specific silicon micro-fabrication techniques. He currently focuses his research on frequency standard technology with Danish Metrology Institute, Kgs. Lyngby, where he is investigating the hollow core photonics crystal fiber application for laser frequency noise reduction in 1 Hz to 100 kHz bandwidth.

Jan Hald, photograph and biography not available at the time of publication.

Antti Lassila, photograph and biography not available at the time of publication.

Paper III

Portable optical frequency standard based on sealed gasfilled hollowcore fiber using a novel encapsulation technique

M. Triches, A. Brusch and J. Hald

Applied Physics B, Vol. 121, No. 3, December 2015

Portable optical frequency standard based on sealed gas-filled hollow-core fiber using a novel encapsulation technique

Marco Triches[1,2] · **Anders Brusch**[1] · **Jan Hald**[1]

Received: 11 June 2015 / Accepted: 10 September 2015 / Published online: 23 September 2015

Abstract A portable stand-alone optical frequency standard based on a gas-filled hollow-core photonic crystal fiber is developed to stabilize a fiber laser to the $^{13}C_2H_2$ P(16) ($\nu_1 + \nu_3$) transition at 1542 nm using saturated absorption. A novel encapsulation technique is developed to permanently seal the hollow-core fiber with easy light coupling, showing negligible pressure increase over two months. The locked laser shows a fractional frequency instability below 8×10^{-12} for an averaging time up to 10^4 s. The lock-point repeatability over one month is 2.6×10^{-11}, corresponding to a standard deviation of 5.3 kHz. The system is also assembled in a more compact and easy-to-use configuration (*Plug&Play*), showing comparable performance with previously published work. The *real* portability of this technology is proved by shipping the system to a collaborating laboratory, showing unchanged performance after the return.

Marie Curie Initial Training Network QTea—Quantum Technology Sensors and Applications, financed by the FP7 program of the European Commission (contract-N MCITN-317485). This work was also funded by the European Metrology Research Programme EMRP (JRP IND14 Frequency). The EMRP is jointly funded by the participating countries within EURAMET and the European Union.

✉ Marco Triches
mt@dfm.dk

[1] Danish Fundamental Metrology, Matematikstorvet 307, 2800 Kongens Lyngby, Denmark

[2] Department of Photonics Engineering, Technical University of Denmark, Ørsteds Plads 343, 2800 Kongens Lyngby, Denmark

1 Introduction

During the last 50 years, many high-resolution spectroscopy techniques have been developed based on saturated absorption spectroscopy (SAS) [1–3]. Laser frequency stabilization is a direct application of these Doppler-free spectroscopy techniques, and many frequency-locking schemes have been developed based on them [4, 5]. Since the demonstration of the first photonic band gap guidance in air [6], the hollow-core (HC) fibers are implemented in many different applications such as gas-sensing [7, 8], high-resolution spectroscopy [9–13], nonlinear optics [14, 15], and laser stabilization [16–18]. The unique property of HC fiber to provide diffraction-less light propagation in air over several meters allows the development of compact gas *cells* with longer interaction length. The in-fiber laser frequency stabilization technique is usually based on the combination of SAS with frequency modulation spectroscopy, using a setup similar to the one presented in [3] for the first time.

During the last decade, stabilized laser performance based on a gas-filled HC fiber reference has increased with the improved properties of the HC fiber, aiming to increase the portability of the technology. A portable optical frequency standard that goes beyond the standards commercially available is important in metrology and in many other applications (optical-sensing, geodesy, telecommunication, etc.) that need an accurate and reliable frequency reference outside the laboratory. However, developing a portable and user-friendly optical frequency standard is not free of challenges.

Despite the 10 years elapsed from the first breakthrough demonstration of a gas cell based on sealed filled HC fiber [16], none of the optical frequency standards commercially available are based on this technology. Fabrication

techniques are far from being production-oriented, and long-term performance may be compromised by atmospheric air contamination due to a non-perfect seal. These issues are likely to be the major causes of the absence of HC fiber-based gas cells on the market. In fact, targeting a suitable encapsulation technique that combines a compact and efficient laser-to-HC fiber coupling with a long-lasting seal is not trivial. Most of the results published so far [16, 19–21] are based on splicing a tapered HC fiber to a solid-core single-mode (SM) fiber or multimode (MM) fiber. The typical loss for a SM-to-HC splice is between 2 and 3 dB [22], especially if an angled splice is adopted to reduce the Fresnel reflection in the air–silica interface [23]. Recently published work [24] confirms that the technique of collapsing the photonic crystal to seal the fiber compromises the light coupling, because of the poor core mode matching and the unwanted back-reflections.

Furthermore, the splicing/tapering sealing method requires a dedicated filling technique in order to avoid atmospheric gas contamination, as proposed in [25]: The fiber is filled with a mixture of helium and acetylene at the wanted acetylene partial pressure, but with a total pressure of more than 2000 hPa. The high total pressure limits the gas contamination during the final splicing/tapering step, and subsequently, the helium diffuses through the glass structure. Moreover, no direct measurement of the long-term pressure stability of sealed gas-filled HC fibers systems can be found in the literature. In previously published work [21], the sealed acetylene-filled HC fiber cannot reproduce the performance achieved with similar fibers deployed in a vacuum chamber filled with acetylene [17], both in terms of fractional frequency instability and lock-point repeatability.

In this paper, we present a novel encapsulation technique that combines an outstanding pressure stability (with negligible broadening rate) with a compact design. In a previously published work [18], we explore the laser stabilization performance of several hollow-core photonic crystal fibers (HC-PCFs) placed in a vacuum chamber and filled with $^{13}C_2H_2$, demonstrating a fractional frequency instability well below 1×10^{-11} for up to one day of averaging time. The chosen $^{13}C_2H_2$ P(16) ($\nu_1 + \nu_3$) line at 1542.3837 nm is the recommended optical transition for the realization of the meter in the telecommunication band [26]. Using the best fiber tested in [18], we develop a prototype of a portable stand-alone optical frequency standard.

The performance is within a factor of three with respect to the results in [18], with a frequency instability one order of magnitude lower than previously published for a sealed HC fiber [21]. The prototype is also assembled in a more user-friendly configuration (*Plug&Play*) showing comparable results with respect to [21], but involving a simpler and more compact detection scheme. The system was shipped

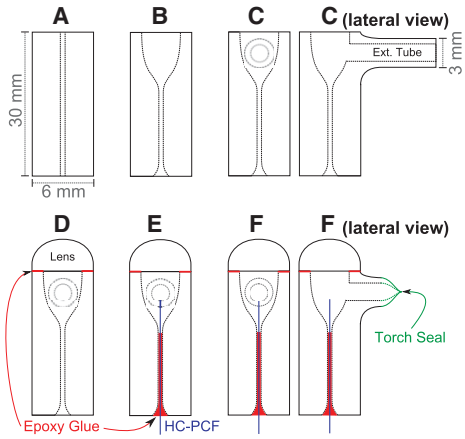

Fig. 1 Description of fabrication steps of the encapsulation method proposed (from **a** to **f**)

to a project partner in Finland [27], preserving its performance before/after the shipment and demonstrating the portability of this technology.

2 Materials and methods

2.1 Fiber encapsulation

The novel encapsulation technique is presented in Fig. 1 and consists of six steps, from A to F.

(A): A 40-mm-long borosilicate capillary tube with internal diameter (ID) compatible with the outer diameter of the fiber is used as a ferrule.

(B): Both the ends of the capillary are annealed, and compressed air is blown through the capillary. This procedure expands the ID of the capillary proportionally to the air pressure used. The front facet of the capillary is blown to reduce glass wall thickness to a less than 2 mm, in order to create a small cavity. The back facet is blown to obtain a slightly larger aperture with a smooth surface. This procedure is important for injection of the fiber during assembly without damaging the fiber facet.

(C): During the annealing process of the front facet, a hole is opened on the sidewall of the capillary. A borosilicate tube is fused to the ferrule in order to have lateral access to the small cavity.

(D): The front facet of the ferrule is lapped/polished to an optical finish, and an aspheric lens (Thorlabs A230-C) is glued on top, using a low-outgassing thermal-curing epoxy glue.

Table 1 Summary of the fiber characteristics

Specs	Fiber	Structure
Core (diameter)	7-cell (8.5 μm)	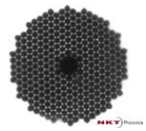
MFD	5.4 μm	
Coupling (loss)	61 % (2.1 dB)	
PM property	Non-PM	
Modes property	Single mode	
Length	∼2.7 m	

This fiber has been tested in [18], where it is called C7_ S

(E): Once cleaved, the HC-PCF end is injected into the cell (from the back end of the ferrule), and the fiber is glued in position using the epoxy glue. The fiber is positioned at the focal plane of the lens by maximizing the coupling efficiency of a collimated beam launched though the lens. The step is repeated for both the facets using two such ferrules. The fiber is injected into the ferrules without stripping the coating, to improve the mechanical stability of the system.

(F): Both the cells are connected to a vacuum pump and to an acetylene vessel via the lateral tube, in order to purge the fiber before filling. The purging step takes about a week. During this step, a silicone-based vacuum sealant (VacSeal®) is put on the external surface of the epoxy layer to improve the sealing stability. Thanks to the solvent component, the sealant diffuses through the epoxy improving the sealing once cured. The sealant is cured at approximately 60 ° C for the entire purging step. Further considerations about the curing process are presented in Sect. 3.1, when the pressure stability of the system is investigated. Once the fiber is purged, the cavity is filled to the low-pressure $^{13}C_2H_2$ vapor. A butane flame torch is used to collapse and seal the lateral tube.

This approach combines the easy pressure handling with the desired coupling efficiency (coupling loss below 2.5 dB), in a compact design. The coupling loss is comparable with the optimized free-space coupling configuration reported in Table 1. In this sense, the proposed encapsulation technique aims to combine the goodness of both previously investigated technologies: the high coupling efficiency of the free-space approach, avoiding unwanted Fresnel reflections/etalon effects typical of the splicing, and the size reduction achievable with the splicing techniques. This technique is likely to be useful for any kind of vapor source, reducing the contamination risk in case of potentially harmful vapor (like Rb) and avoiding use of high concentration of buffer gasses. Moreover, a non-permanent seal with good performance is possible using vacuum grease instead of the epoxy glue, which allows the cell to be cleaned and the fiber to be replaced.

2.2 Fiber specifications

The system is developed using the HC-PCF presented in Table 1, which had the best performance both in terms of fractional frequency instability and lock-point repeatability in a previously published work [18].

After being encapsulated and purged, the fiber is filled with 15 Pa of $^{13}C_2H_2$ vapor, which is a factor of two below the optimum pressure as discussed in Sect. 3.2. The resulting lower pressure with respect the optimum (30 Pa) is due to a mistake in the filling procedure. The optical absorption measured after the sealing confirms that ∼15 Pa of $^{13}C_2H_2$ are loaded into the fiber. In the following discussion, we will refer to sealed gas-filled HC fiber as the *stand-alone system*, i.e., a sealed HC fiber not connected to an external vacuum apparatus.

2.3 Frequency-locking scheme

The same SAS setup described in [18] is used to monitor the performance of the stand-alone system (Fig. 2). A fiber laser source (Koheras E15 Adjustik^{TM}) is split into two beams, called pump and probe, respectively. The pump beam is intensity modulated at 9 kHz (and blue-detuned by 35 MHz) using an acousto-optic modulator (AOM). The probe beam is blue-detuned by 40 MHz using a second AOM, after being amplified by an erbium-doped fiber amplifier (EDFA). An electro-optic modulator (EOM) is used to phase modulate the probe at 32 MHz to generate the sidebands needed for frequency modulation spectroscopy. Two different configurations are used to test the performance of the stand-alone system (Fig. 2):

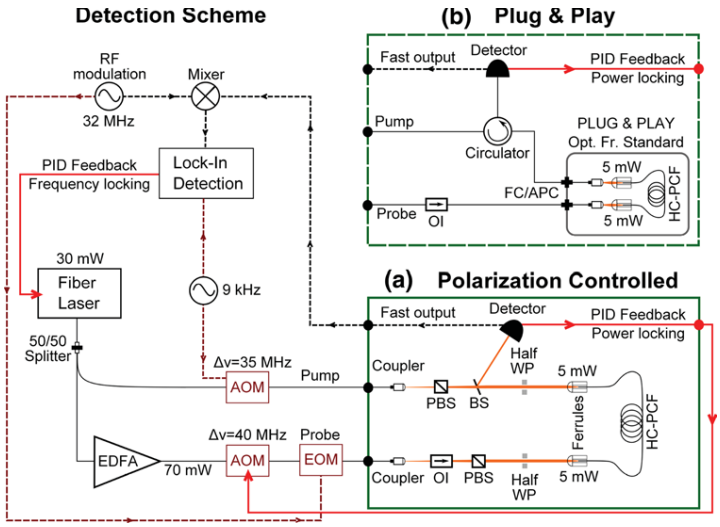

Fig. 2 Schematic layout of the SAS setup. *OI* Optical isolator. *PBS* Polarizing beam splitter. *Half WP* Half-wave plate. *EDFA* Erbium-doped fiber amplifier. *FC/APC* Fiber connector/angle physical contact. *Filled black line* optical fibers. *Dashed line* coaxial cables. **a** Polarization-controlled scheme. **b** *Plug&Play* scheme (*dashed contour*). The detection scheme used is the same for both the configurations

Configuration (a): The pump and probe beams are free space coupled to the sealed HC fiber, and the polarization of the two counter propagating beams is controlled using polarizing beam splitters (PBS) combined with zero-order half-wave plates. Using a beam splitter, the transmitted probe is collected for detection. This configuration is similar to the one described in [21].

Configuration (b): In the *Plug&Play* configuration, the stand-alone optical frequency standard is assembled in a compact and user-friendly configuration: The cells are placed inside a $30 \times 30 \times 15\,\mathrm{cm}^3$ aluminum box, and all the optical components used to control the polarization are removed. Access to the HC fiber inside the box is accomplished via two FC/APC connectors. A fiber-based circulator on the pump arm is used to collect the transmitted probe signal.

In both configurations, the transmitted probe light is coupled to a low noise detector with both AC and DC outputs. The fast signal is used to lock the laser to the optical transition, using a lock-in amplifier combined with a servo loop. The DC output is used to stabilize the probe power via the probe AOM. Both beams have a power of 5.5 mW at the HC fiber input (about 3.3 mW average coupled power). The power used is chosen to reproduce the experimental configuration in [18], in order to easily compare the performance between the stand-alone system and the results reported in [18]. Moreover, two equally intense beams reduce the possible frequency shift of the locking point due to the interaction with any high-order HC fiber modes, as explained in [18]. A small fraction of the laser output is combined with the output of the reference laser (described in [5]), and the resulting beat signal is monitored with a fast photodiode and a frequency counter. In configuration (a), the polarization of the two counter propagating beams is orthogonal and linear. Despite the fact that fiber is not meant to be polarization maintaining, it is slightly birefringent because of the non-perfectly circular core shape. Therefore, keeping the pump (probe) beam aligned to the *fast* (*slow*) axis of the fiber prevents any instability caused by an unstable polarization configuration in the light–matter interaction, as observed in [18].

In the SAS schemes described, the contribution to the full width at half maximum (linewidth) of the sub-Doppler transition profile due to the acetylene pressure is about 4 MHz [5] for an acetylene pressure of 15 Pa. The absorption of the $^{13}C_2H_2$ P(16) line for a 2.7-m fiber at 15 Pa is about 30 % [28]. The transit-time broadening is often the major limiting factor for SAS in HC fibers, because the small mode field diameter (MFD) is one to two orders of magnitude smaller than what is typically used in bulk vapor cell systems. This effect is the main limiting factor associated with this technology, and it is inversely proportional to the MFD. The transit-time broadening contributes to the linewidth with about 26 MHz for the fiber used [12, 29]. The linewidth of the sub-Doppler profile is expected to be around 29–32 MHz at the filling date.

3 Results and discussion

3.1 Pressure stability

In order to evaluate the pressure stability, the linewidth of the sub-Doppler feature is monitored for several months. In this configuration, the fiber laser is offset-locked with

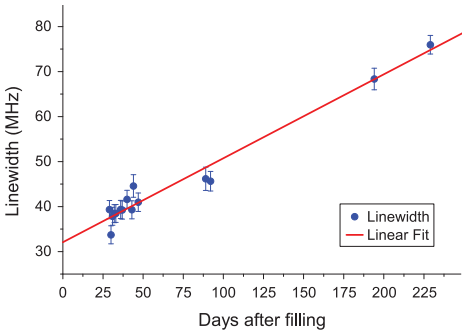

Fig. 3 Sub-Doppler linewidth monitored after filling. The *Plug&Play* system was shipped to a project partner between 100 and 180 days after filling [27]. Each data point is the mean value of multiple measurements of the linewidth. The *error bars* represent the standard deviation associated with each value. The *red line* represents the linear fit of the data

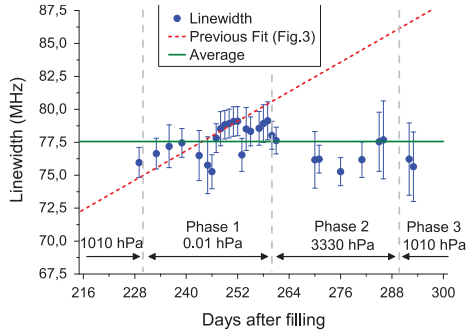

Fig. 4 Pressure test of the stand-alone system. *Red dashed line* previous broadening rate (Fig. 3) given for reference. *Green line* average of the data points. The different phases of the test are highlighted. Each data point is the mean value of multiple measurements of the linewidth of the sub-Doppler feature. The *error bars* represent the standard deviation associated with each value

respect to the reference laser [5], and the offset frequency is scanned across the optical transition. The full sub-Doppler optical profile is fitted with a sum of two Lorentzian functions with identical center frequency but individual linewidth and amplitudes. This approach allows us to take into account the contributions to the sub-Doppler feature from both the slow and fast molecules inside the HC fiber, as described in [12]. An example of the sub-Doppler profile of the stand-alone system is reported in [27].

Figure 3 shows the linewidth monitored over 200 days after filling. The system clearly suffers a pressure broadening due to a leak point in the sealing and/or to a source of outgassing inside the cells. The linear regression of the data shows a broadening rate of 186 kHz/day with a standard uncertainty of 9 kHz/day. The estimated linewidth at the filling date is 32 MHz with a standard uncertainty of 1 MHz, which is consistent with the expected value, see Sect. 2.3.

The broadening is due to a pressure increase inside the cell. The most probable scenarios that can cause this effect are as follows:

1. The fiber coating exposed inside the cell is outgassing due to the low pressure.
2. The presence of a leak in the sealing points.
3. The vacuum sealant (VacSeal) applied around the sealing points is not cured completely (see Sect. 2.1). The solvent present in the uncured sealant diffuses through the glue, eventually degassing inside the cell.

In order to discriminate which source is compromising the performance of the system, a vacuum compatible box with glass windows is assembled. The stand-alone system is placed inside, and the box is connected to a vacuum pump and to a nitrogen vessel (99.99 % purity). The detection scheme is restored to the configuration (a), see Sect. 2.3. In this manner, we can manipulate the pressure of the atmosphere that surrounds the stand-alone system and monitor the linewidth evolution over time. If the broadening is caused by an internal outgassing source, the broadening rate will be independent of applied external pressure. If the sealing has a leak point, the broadening rate will increase/decrease proportionally to the increase/decrease in the external pressure. Moreover, exposing the cells to a low pressure could contribute to cure/evaporate the solvent remaining in the applied sealant layer. The following testing scheme is implemented to the stand-alone system starting from 230 days after filling:

Phase 1 The pressure that surrounds the stand-alone system is lowered down to 0.01 hPa. In this phase, we can neglect the pressure gradient between the cells and the surrounding.

Phase 2 The pressure that surrounds the stand-alone system is increased to 3330 hPa (nitrogen atmosphere).

Phase 3 The box is opened, and the stand-alone system is exposed to the laboratory atmosphere (1010 hPa).

All the three phases are operated at room temperature, and the results are plotted in Fig. 4. The broadening rate registered in the first 230 days is plotted as reference (red dashed line). No statistical evidence of pressure broadening can be observed in any of the three test phases. Instead, the broadening rate stops during the first phase, confirming that the probable cause of broadening experienced in the first 230 days is due to the uncured sealant. It is recommended

by the manufacturer to cure the sealant over about four days at 240 ° C, which is not feasible without damaging the fiber. A low-temperature curing approach may cure well the outer layer of the sealant applied, trapping the solvent within the polymer for many months, creating a continuing outgassing problem [30]. This result demonstrates that the sealant can be successfully cured adding a vacuum treatment step for about a couple of weeks instead of an high-temperature exposure. This curing approach can be implemented simultaneously to the fiber purging step, thus solving the issue without increasing the total fabrication time.

The data presented in Fig. 4 show an average linewidth of 77.5 MHz with a standard uncertainty of 0.9 MHz. The acetylene-equivalent pressure of the system is around 200 Pa, calculated using the self-broadening coefficient reported in [5]. This estimate only gives an order of magnitude for the pressure at the end of the test. To give a reliable pressure estimate, the composition of the introduced gasses with their relative broadening coefficients is needed. A linear regression of the data shows a slope of −13 kHz/day with a standard uncertainty of 18 kHz/day. This trend is compatible with a negligible pressure broadening over two months. From the slope and the corresponding uncertainty, we estimate an upper limit for the residual broadening of +5 kHz/day, which corresponds to a rate below 2 MHz/year.

3.2 Frequency instability

The performance of the stand-alone system is compared to the reference laser described in [5], both in terms of frequency instability and locking-point repeatability. All the measurements presented here are repeated five times to check the performance repeatability. Figure 5 represents the fractional frequency instability of the beat note between the laser locked to the stand-alone system and the reference laser [5]. The figure includes also a comparison with previously published results for a laser stabilized to a permanently sealed HC fiber filled with acetylene [21]. The free-running laser performance as well as the lower-limit instability achieved with the actual fiber [18] is shown as a reference.

The performance in configuration (a) shows a fractional frequency instability well below 1×10^{-11} for averaging time $1 < \tau < 10^4$ s. The difference between configuration (a) and [18] in terms of instability (a factor of 2.5) can be ascribed to the slightly different configurations involved. The stand-alone system is characterized by a lower filling pressure and slightly shorter fiber (2.7-m fiber filled at 15 Pa) as compared to the fiber used in [18] (3-m fiber filled at 29 Pa). This difference contributes to decrease in the amplitude of sub-Doppler signal by approximately a factor of two, increasing the instability proportionally in the short timescale. Moreover, the data reported in [18] are acquired in a temperature-stabilized environment, which contributes to lower the instability. These facts allow us to infer that the instability of the stand-alone system (and of the *Plug&Play* as well) can be lowered by a factor of two by optimizing the fiber length and the filling pressure.

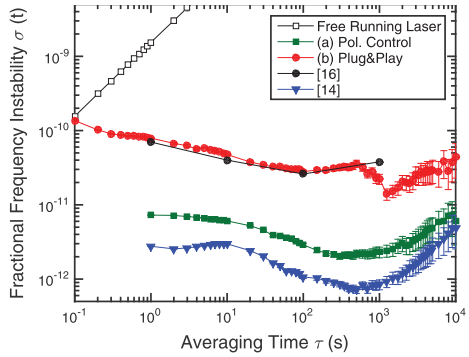

Fig. 5 Fractional frequency instability (Allan deviation) of the two different configurations. *Green filled squares* configuration (*a*). *Red filled circles* configuration (*b*). The results published in [21] (*black filled circles*), in [18] (*blue filled triangles*), and the free-running laser performance (*black empty squares*) are plotted for reference

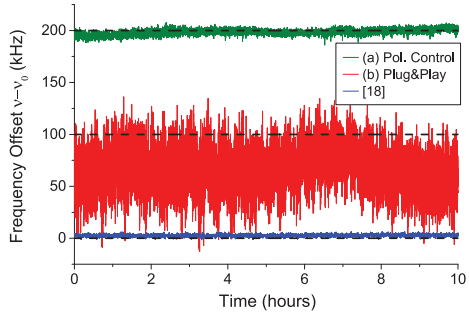

Fig. 6 Frequency of the locked laser over time. The results are plotted with a relative shift of 100 kHz for clarity, after the frequency of the reference laser [5] is subtracted. The best frequency offset performance achieved with the actual HC fiber is plotted for reference [18]. The colors are the same assigned in Fig. 5

The performance in *Plug&Play* configuration (b) is comparable with the one reported in [21], but with a slightly simpler setup, avoiding the fiber-optic polarization controller and with ready-to-use fiber connectors. The importance of the polarization control on SAS in HC fibers has already

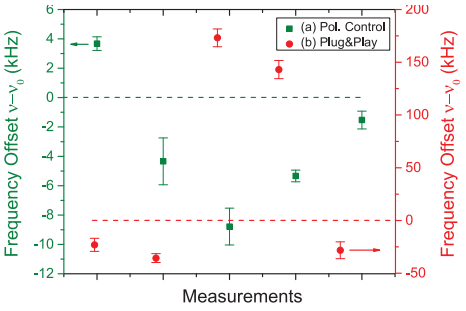

Fig. 7 Lock-point repeatability is presented. *Green squares* configuration (*a*). *Red circles Plug&Play* configuration (*b*). The *error bars* represent the root mean square value of the measured data. A *dashed line* is added to highlight the zero offset level of each data series

been reported [18, 21], and it is confirmed by the analysis of the frequency offset data in Fig. 6. The frequency difference between the laser locked to the stand-alone system (both in (a) and (b) configurations) and the reference laser [5] is presented. The data are plotted with a relative shift of 100 kHz for clarity. The performance of the actual HC fiber as reported in [18] is plotted for reference.

The frequency fluctuations in the *Plug&Play* configuration (b) with respect to the configuration (a) where the light polarization is controlled are clearly confirming that the absence of polarization control of the launched light is detrimental for the stability of the locked laser. The data in configuration (b) are acquired 60 days after the measurements in configuration (a). During the time elapsed, the linewidth increased by approximately 12 MHz (about 30 % increase) because of the broadening rate. This effect gives a small contribution to the increased instability of the *Plug&Play* system with respect to the configuration (a). The increased instability is mainly ascribed to the absence of polarization control (factor of 7.5) with a minor contribution due to the increased linewidth (factor of 1.3).

Finally, the lock-point repeatability is measured on five different days for both configurations (Fig. 7) over one week. In configuration (a), the stand-alone system shows an average shift of -3.3 kHz with respect to the reference, with a standard deviation of 5.3 kHz, which is comparable with the results we reported in [18]. In the *Plug&Play* configuration (b), the system shows an average shift of $+46$ kHz, with a standard deviation of 103 kHz. This analysis confirms the importance of the polarization control on the light launched into the HC fiber. In order to preserve the outstanding stability/repeatability observed in configuration (a), suitable oriented polarization maintaining fibers can be implemented in the pump/probe arm.

4 Conclusion

We have developed a stand-alone optical frequency standard based on a portable compact gas cell made of a sealed HC fiber filled with $^{13}C_2H_2$. The performance of the novel encapsulation technique is investigated, and the pressure stability is characterized over almost a year. No pressure increase is observed over the last 60 days, with the residual broadening rate having an upper limit below 2 MHz/year. To our knowledge, this result demonstrates the long-lasting pressure stability of a sealed gas-filled HC fiber for the first time, solving a crucial technical issue for a future commercialization of similar systems. The stand-alone system is tested in terms of fractional frequency instability showing an Allan deviation below 8×10^{-12} for an averaging time up to 10^4 s (in a polarization-controlled configuration). The frequency of the lock point is repeatable to ± 5.3 kHz (standard deviation over five measurements), resulting in the most stable and accurate laser system locked to a permanently sealed acetylene-filled HC fiber published so far [21]. The system is also assembled in a user-friendly configuration (*Plug&Play*) that shows comparable performance with respect to previously reported results [21], but involving a simpler detection setup. The *Plug&Play* optical frequency standard fits in a box of $30 \times 30 \times 15$ cm^3 , equipped with fiber connectors. The system was also shipped to partners in Helsinki with unchanged performance before/after the shipment, proving the real portability of the optical frequency standard. Future improvements will address the optimization of the main parameters such as gas pressure, fiber length, and saturation power. Further reduction in physical size will be addressed as well.

Acknowledgments A thanks to NKT Photonics for providing the special fiber used in the papers published so far. A special thanks also to Jan P. Scholer for the practical realization of the glass cells and to Philip G. Westergaard for the feedback received during the cell testing.

References

1. C. Wieman, T.W. Hänsch, Phys. Rev. Lett. **36**(20), 1170 (1976)
2. F.V. Kowalski, W.T. Hill, A.L. Schawlow, Opt. Lett. **2**(5), 112 (1978)
3. J.L. Hall, Appl. Phys. Lett. **39**(9), 680 (1981)
4. C.S. Edwards, H.S. Margolis, G.P. Barwood, S.N. Lea, P. Gill, W.R.C. Rowley, Appl. Phys. B **80**(8), 977 (2005)
5. J. Hald, L. Nielsen, J.C. Petersen, P. Varming, J.E. Pedersen, Opt. Express **19**(3), 2052 (2011)
6. R.F. Cregan, B. Mangan, P. Russell, J. Knight, P. Roberts, D. Allan, Science **285**(5433), 1537 (1999)
7. T. Ritari, J. Tuominen, H. Ludvigsen, J.C. Petersen, T. Sørensen, T.P. Hansen, H.R. Simonsen, Opt. Express **12**(17), 4080 (2004)
8. W. Jin, Y. Cao, F. Yang, H.L. Ho, Nat. Commun. **6**, 6767 (2015)
9. R. Thapa, K. Knabe, M. Faheem, A. Naweed, O.L. Weaver, K.L. Corwin, Opt. Lett. **31**(16), 2489 (2006)

10. S. Ghosh, J.E. Sharping, D.G. Ouzounov, A.L. Gaeta, Phys. Rev. Lett. **94**(9), 093902 (2005)
11. S. Ghosh, A.R. Bhagwat, C.K. Renshaw, S. Goh, A.L. Gaeta, B.J. Kirby, Phys. Rev. Lett. **97**(2), 023603 (2006)
12. J. Hald, J.C. Petersen, J. Henningsen, Phys. Rev. Lett. **98**(21), 213902 (2007)
13. C. Perrella, P.S. Light, T.M. Stace, F. Benabid, A.N. Luiten, Phys. Rev. A **85**, 12518 (2012)
14. A.R. Bhagwat, A.L. Gaeta, Opt. Express **16**(7), 5035 (2008)
15. P.S.J. Russell, P. Hölzer, W. Chang, A. Abdolvand, J.C. Travers, Nat. Photonics **8**(4), 278 (2014)
16. F. Benabid, F. Couny, J.C. Knight, T.A. Birks, P.S.J. Russell, Nature **434**(7032), 488 (2005)
17. K. Knabe, S. Wu, J. Lim, K.A. Tillman, P.S. Light, F. Couny, N. Wheeler, R. Thapa, A.M. Jones, J.W. Nicholson, B.R. Washburn, F. Benabid, K.L. Corwin, Opt. Express **17**(18), 16017 (2009)
18. M. Triches, M. Michieletto, J. Hald, J.K. Lyngsø, J. Lægsgaard, O. Bang, Opt. Express **23**(9), 11227 (2015)
19. C. Hensley, D.H. Broaddus, C.B. Schaffer, A.L. Gaeta, Opt. Express **15**(11), 6690 (2007)
20. P.T. Marty, J. Morel, T. Feurer, J. Light. Technol. **28**(8), 1236 (2010)
21. C. Wang, N.V. Wheeler, C. Fourcade-Dutin, M. Grogan, T.D. Bradley, B.R. Washburn, F. Benabid, K.L. Corwin, Appl. Opt. **52**(22), 5430 (2013)
22. R. Thapa, K. Knabe, K.L. Corwin, B.R. Washburn, Opt. Express **14**(21), 9576 (2006)
23. F. Couny, F. Benabid, P. Light, IEEE Photonics Technol. Lett. **19**(13), 1020 (2007)
24. P.S. Light, J.D. Anstie, F. Benabid, A.N. Luiten, Opt. Lett. **40**(12), 2703 (2015)
25. P.S. Light, F. Couny, F. Benabid, in *Conf. Lasers Electro-Optics/ Quantum Electron. Laser Sci. Conf. Photonic Appl. Syst. Technol.* (Optical Society of America, Baltimore, Maryland, 2007), p. CThKK4
26. R. Felder, Metrologia **42**(4), 323 (2005)
27. J. Seppa, M. Merimaa, A. Manninen, M. Triches, J. Hald, A. Lassila, I.E.E.E. Trans, Instrum. Meas. **64**(6), 1595 (2015)
28. M. Kusaba, J. Henningsen, J. Mol. Spectrosc. **209**(2), 216 (2001)
29. V.S. Letokhov, *High-Resolution Laser Spectroscopy, Topics in Applied Physics*, vol. 13 (Springer, Berlin, Heidelberg, 1976)
30. VacSeal Inc. Vacseal High Vacuum Leak Sealant—Curing Protocols. http://www.2spi.com/catalog/vac/vacseal-curing-protocols.html

Appendix I. List of Publications and Submitted Manuscripts

Paper IV

Compact, CO_2-stabilized tuneable laser at 2.05 microns

P. G. Westergaard, J. W. Thomsen, M. R. Henriksen, M. Michieletto,
Marco Triches, J. K. Lyngsøand J. Hald
Manuscript submitted to *Optics Express*

Compact, CO_2-stabilized tuneable laser at 2.05 microns

Philip G. Westergaard[1,*], Jan W. Thomsen[2], Martin R. Henriksen[2], Mattia Michieletto[3], Marco Triches[1], Jens K. Lyngsø[3], and Jan Hald[1]

[1]*Danish Fundamental Metrology, Matematiktorvet 307, DK-2800 Kgs. Lyngby, Denmark*
[2]*Niels Bohr Institute, Blegdamsvej 17, DK-2100 Kbh. Ø, Denmark*
[3]*NKT Photonics A/S, Blokken 84, DK-3460 Birkerød, Denmark*
[*]*Corresponding author: pgw@dfm.dk*

Abstract: We demonstrate a compact fibre-based laser system at 2.05 microns stabilized to a CO_2 transition using frequency modulation spectroscopy of a gas-filled hollow-core fibre. The laser exhibits an absolute frequency accuracy of 5 MHz, a frequency stability noise floor of better than 7 kHz or 5×10^{-11} and is tunable within $\pm$200 MHz from the molecular resonance frequency while retaining roughly this stability and accuracy.

OCIS codes: (140.3425) Laser stabilization; (140.3510) Lasers, fiber; (060.4005) Microstructured fibers; (280.4788) Optical sensing and sensors; (300.6380) Spectroscopy, modulation.

References and links

1. M. Triches, M. Michieletto, J. Hald, J. K. Lyngsø, J. Lægsgaard, and O. Bang, "Optical frequency standard using acetylene-filled hollow-core photonic crystal fibers", Opt. Express **23**, 11227-11241 (2015).
2. A. Lurie, et al., "High-performance iodine fiber frequency standard", Opt. Lett. **36**, 4776-8 (2011).
3. C. Wang, et al., "Acetylene frequency references in gas-filled hollow optical fiber and photonic microcells", Appl. Optics **52**, 5430-5439 (2013).
4. F. Benabid, F. Couny, J. C. Knight, T. A. Birks, and P. S. J. Russell, "Compact, stable and efficient all-fibre gas cells using hollow-core photonic crystal fibres", Nature **434**, 488-91 (2005).
5. P. Meras, I. Y. Poberezhskiy, D. H. Chang, and G. D. Spiers, "Frequency Stabilization of a 2.05 μm Laser Using Hollow-Core Fiber CO2 Frequency Reference Cell", Proc. SPIE **7677**, 767713-767713-9 (2010).
6. G. C. Bjorklund and M. D. Levenson, "Sub-Doppler frequency-modulation spectroscopy of I_2", Phys. Rev. A **24**, 166–169 (1981).
7. M. Triches, A. Brusch, and J. Hald, "Portable optical frequency standard based on sealed gas-filled hollow-core fiber using a novel encapsulation technique", accepted for publication in Appl. Phys. B (2015).
8. J. K. Lyngsø et al., "Single-mode 7-cell core hollow core photonic crystal fiber with increased bandwidth", Proceedings of SPIE **7753**(1), 77533Q 77533Q 4 (2011).
9. R. M. Gerosa, D. H. Spadoti, L. d. S. Menezes, and C. J. S. de Matos, "In-fiber modal Mach-Zehnder interferometer based on the locally post-processed core of a photonic crystal fiber", Opt. Express **19**, 31249 (2011).

1. Introduction

The development of hollow-core photonic crystal fibre (HC-PCF) technology over the past decade has opened up a vast array of possibilities for new applications. When filled with gas, the HC-PCF is a good candidate for frequency stabilization and sensing in demanding environments such as field operations and space applications, since this provides a compact, low-weight container for molecular gas while retaining large interaction length between laser light coupled trough the fibre and the molecules inside the hollow core. Specifically for satellite-based LIDAR (LIght Detection And Ranging) measurements, a lightweight laser source with

high stability and accuracy is desirable, since the accuracy of the LIDAR measurement depends directly on these parameters.

Current state-of-the-art laser frequency stabilisation using gas-filled hollow-core fibres have demonstrated a relative long-term instability of about 4×10^{-12} and relative short-term instability of about 2×10^{-12} for one second averaging time [1–3]. These results were obtained with acetylene and iodine using saturated absorption spectroscopy, which gives linewidths of typically 20 MHz. The main limitations to the stability are decoherence due to collisions between molecules and the inner wall of the HC-PCF as well as excitation of higher order optical modes in the HC-PCF. Stabilization to Doppler broadened absorption lines has also been demonstrated in the telecom wavelength range using acetylene [4] as well as in the 2 micron range using CO_2 filled HC-PCF [5], but without the possibility of tuning the offset frequency.

Here, we report on a compact fibre-based laser system at 2.05 microns stabilised to the CO_2 P(30) transition at 2050.967 nm using frequency modulation spectroscopy [6] in a gas-filled hollow-core fibre. The laser system was developed as a part of a project for the European Space Agency (ESA) aiming towards satellite-based LIDAR measurements. Several requirements on size, accuracy and stability of the system were therefore imposed; all of which our system meets. The compact fiber-based optical setup fits inside a box with dimensions $(25 \times 25 \times 5)$ cm^3. The laser exhibits an absolute frequency accuracy of better than 5 MHz or 3×10^{-8}, frequency stability of better than 10^5 Hz$/\sqrt{\tau}$ up to around 1000 s and is tunable within $\pm$200 MHz from the molecular resonance frequency while retaining roughly this stability and accuracy.

2. Experimental Setup

The optical part of the setup consists of a fiber-coupled DFB laser (EP2051 series, Eblana Photonics), an electro-optic modulator (EOM), two HC-PCFs of different length for probing different molecular transitions, two ferrules per HC-PCF for gas filling and coupling of light in and out of the HC-PCF, and a photo detector.

An overview of the experimental setup is shown in Fig. 1. The DFB laser comes in a polarization-maintaining fiber-coupled butterfly package. Furthermore, a thermo-electric element for temperature control at the mK level is integrated in the laser package. The light is split after the laser using a fiber splitter, where 80 % is used as output light (4.3 mW) and 20 % is used to generate an error signal for locking. The part of the light used for locking is first phase modulated at frequencies between 300 MHz and 3 GHz using a fiber-coupled EOM (MPZ2000 series, Photline Technologies).

After modulation, the light is sent through the HC-PCF. The coupling between the PM/SM fibres used for the laser and the HC-PCF utilizes a ferrule method developed in-house at DFM [7]. The HC-PCF is inserted into one end of a glass ferrule and an aspheric lens is attached to the other end for coupling. To ensure optimal, alignment-free coupling the PM/SM fibre is connected to a free space coupler, which is bonded together with the HC-PCF ferrule. The alignment and coupling are optimised using a 6-axis translational/rotational stage before gluing. A glass tube attached to the side of the ferrule is used to first evacuate and then fill the HC-PCF to the desired pressure. After filling the system is sealed by melting the side tube shut with a blow torch. After travelling through the HC-PCF, the light is coupled into free space again and detected on the high bandwidth (12 GHz) photo diode. Around 50 μW of the light reaches the detector when the laser is tuned off resonance.

The HC-PCF employed in our setup is specifically designed to increase the frequency stability of the laser lock. Mode interference in the HC-PCF has a negative influence on the frequency stability, since it causes a varying dependence of the transmission on laser offset frequency, which distorts the error signal of the lock unpredictably. Therefore, we designed and fabricated

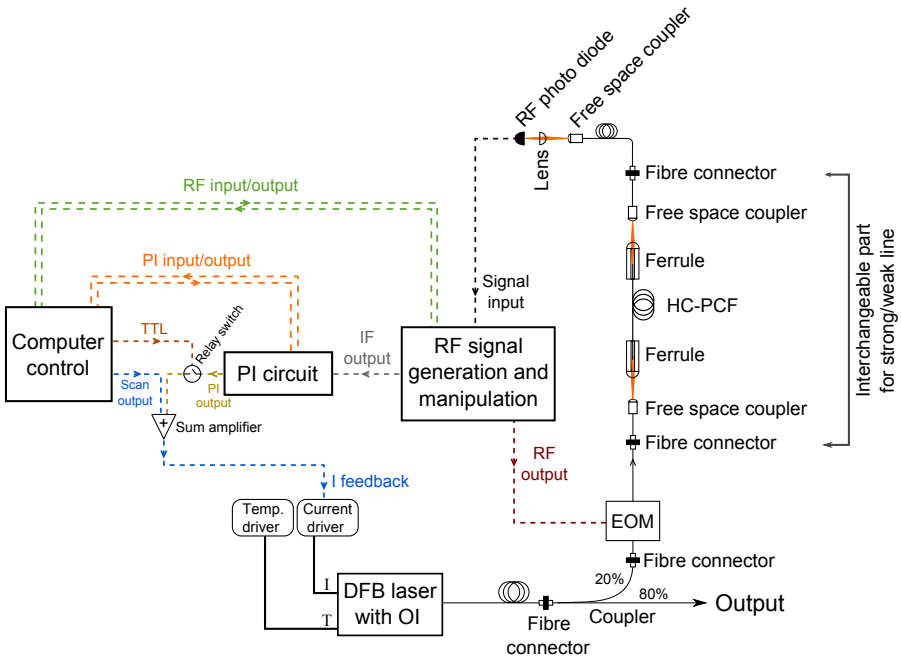

Fig. 1. An overview of the experimental setup. OI: Optical Isolator, HC-PCF: Hollow-Core Photonic Crystal Fiber. The dashed lines indicate electronic DC or RF signal paths.

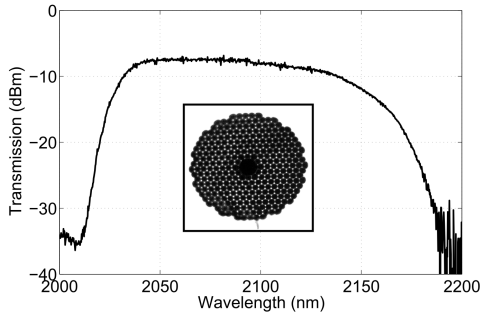

Fig. 2. Characteristics of the fabricated HC-PCF. Transmission measurement through 1 m fiber. The inset shows a microscope image of the end face of the HC-PCF.

a fiber for guidance around 2050 nm with suppression of higher order core modes. The fiber is a 7cell HC-PCF with reduced core wall thickness to enable single mode propagation at the short wavelength region of the bandgap, similar to the one described in [8]. It has a cladding air filling fraction of approximately 90 percent, a core diameter of 15 μm and a cladding pitch of 5 μm. Fig. 2 shows the 150 nm wide transmission window centered at 2100 nm. Characterization

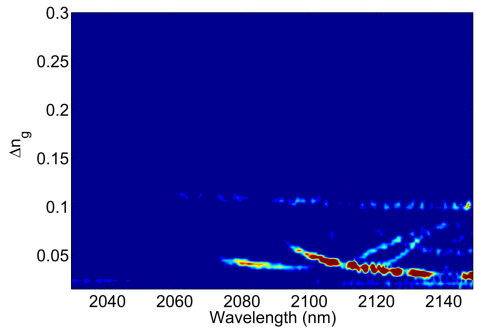

Fig. 3. Higher order mode characterization of the HC-PCF using Windowed Fourier Transform method. The figure shows the mode content of the differential group indices with red being the densest and blue the thinnest. Dense mode content for non-zero differential group index indicates the presence of higher order modes in the fiber.

of the higher order mode content can be achieved using white light intereferometric measurements as described in references [1,9]. Using the same setup used in the characterization of the HC-PCFs presented in [1], a windowed Fourier transform analysis can be used to temporally separate the different modes and determine their effective group index difference with respect to the fundamental mode. The high order modes travel with a different group velocity along the HC-PCF with respect to the fundamental mode. This results in a relative delay of the wave fronts between the modes which causes an interference occurring between the majority of the light coupled into the fundamental mode and the other modes. A windowed Fourier transform analysis allows one to separate the different modes in terms of the group velocity different with respect to the fundamental one. To quantify this, light from a white light source was launched with high NA into a 50 cm section of the HC-PCF. At the output end of the HC-PCF light was collected with a single mode fiber and the resulting interferogram was recorded using a Yokogawa AQ6375 spectrum analyzer. Fig. 3 shows the differential group indices calculated from the windowed Fourier transform of the interferogram. Here, it can be seen that the current fiber has a higher order mode cut-off at around 2070 nm, below which the fiber only supports a single spatial core mode. The relatively flat response at a differential group index of approximately 0.1 is an artefact of the measurement equipment similar to the one observed in [1].

The complete optical part of the setup fits in a compact box with dimensions $(25 \times 25 \times 5)$ cm^3. The assembled optical box is presented in Fig. 4. The numbered components in the figure are described in Table 1.

For increased versatility, we have produced two different HC-PCFs of different length, both coupled, filled and sealed using the ferrule technique. Fiber 1 has a length of $L_1 = 10$ m and was filled with $^{12}CO_2$ to a pressure of $P_1 = 35$ hPa and the second fiber has $L_2 = 100$ m and filled to $P_2 = 55$ hPa with $^{13}CO_2$. Each fiber is coiled on a copper spool of 8 cm radius and the two spools are placed on top of each other (see item 12 in Fig. 4). The pressure in the short fiber was selected to optimize the error signal slope for the strong CO_2 line at 2050.967 nm. Similarly, the pressure in the long fiber was optimised for a different transition at 2050.7222 nm which has a line strength roughly a factor 100 weaker than the strong line. Both fibers can be used in the optical setup by a simple change of input/output fiber connectors in the optics box. In this work, we will concentrate on the results obtained from the short fiber with the strong transition at 2050.967 nm.

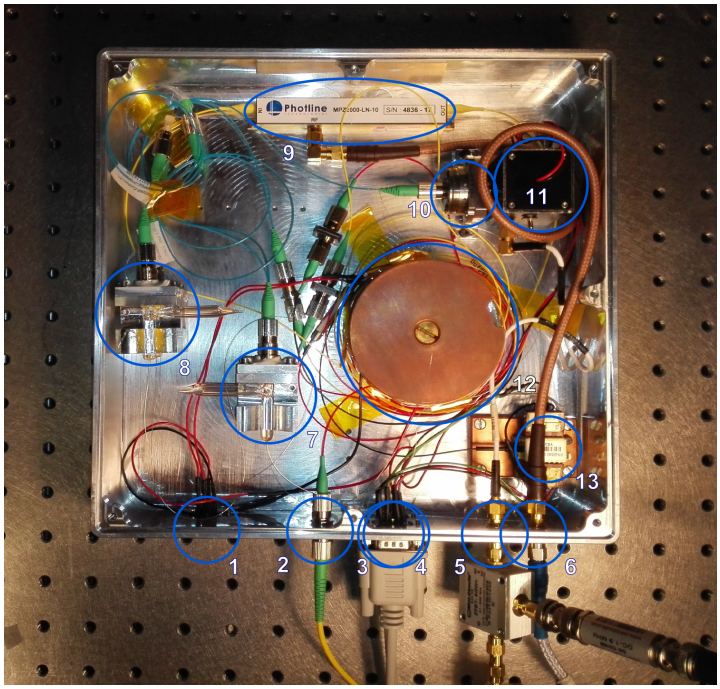

Fig. 4. An overview of the optical setup inside a box with outer dimensions $(25 \times 25 \times 5)$ cm^3. The numbered items are described in Table 1.

Designation	Description
1	Input/output for the temperature control of the fibre spools. This includes the Peltier element and the thermistor hidden beneath the fibre spools.
2	Optical output (80 % arm from fibre coupler).
3	(top) Electrical connections for the current and temperature control of the DFB laser.
4	(bottom) 3V supply for the biased photo diode.
5	RF and DC output from the photo diode. The RF and DC part is split with a biastee outside the box.
6	RF input for driving the EOM.
7	Input and output ferrules for the short HC-PCF (mounted on top of each other).
8	Input and output ferrules for the long HC-PCF (mounted on top of each other).
9	Electro-Optics Modulator. MPZ2000 series, Photline Technologies.
10	Free space coupler with additional lens for coupling into photo detector.
11	Biased photo diode. Newport 818-BB-51.
12	Fibre spools that hold the short (bottom) and long (top) HC-PCFs.
13	DFB laser on copper mount.

Table 1. Explanations of the numbered items in Fig. 4.

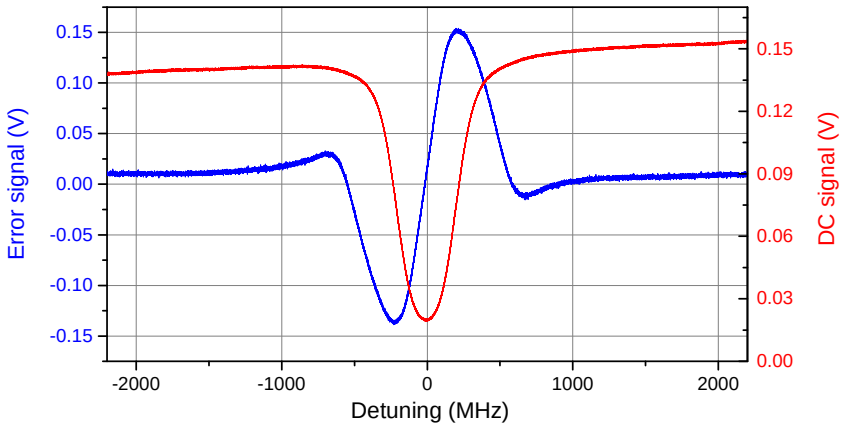

Fig. 5. The absorption signal (red curve) derived from the photo detector DC level, and the corresponding FM spectroscopy error signal (blue curve). The sweep time was 2 seconds without any averaging.

The drive current and temperature regulation for the DFB laser is supplied to the optical assembly from an external box containing all drive and control electronics (not shown in Fig. 4). Similarly, the RF signal driving the EOM is sent from the electronics box to the RF input of the optical assembly. The signal from the light detected on the RF photo diode is split into DC and RF parts by a bias-tee outside the box, and the RF signal is amplified before being mixed with the LO at the modulation frequency. This produces an error signal used for locking. The DC signal shows the molecular absorption and is used for frequency calibration and monitoring of the lock status. The DC and error signals are shown in Fig. 5.

The design also features the possibility to temperature stabilize the spool holding the HC-PCF (not shown in Fig. 1). This is done using a Peltier element inserted between the spool and the bottom of the optics box. In the stable laboratory environment, however, it was found unnecessary to stabilize the temperature. In a more noisy setting, stabilizing the temperature might prove beneficial to reduce fluctuating transmission variations of the HC-PCF.

The signal processing and locking is controlled by a computer program through a National Instruments DAQ board. The program can select the modulation frequency from one of two VCOs in the ranges [250, 400] MHz and [1800, 3200] MHz. The program features the possibility to lock off resonance at a user-determined offset frequency in the ranges [-200, 200] MHz and $[\pm 1900, \pm 2800]$ MHz. For the low frequency offset an electronic offset is added to the error signal obtained with low frequency modulation ($\sim$ 320 MHz, as shown in Fig. 5) before the PI circuit. The relation between the electronic offset and the resulting offset frequency is obtained by a calibration of the frequency axis in the control program. This calibration sequence takes place automatically in the program and occurs at user-determined time intervals.

The first step in the calibration sequence is determining the zero detuning. The low frequency VCO is set to the frequency where the last calibration found the optimum (i.e., largest) slope of the error signal. The laser current is then scanned by sending a voltage ramp to the modulation input of the current driver from the DAQ board. From here, the slope is optimised again by changing the VCO frequency slightly. The slope is obtained by a linear fit around the last zero crossing value. Once the largest slope is determined, the scan voltage corresponding to zero frequency offset is determined by the scan voltage where the error signal crosses zero

(corrected by a possible offset determined from residual amplitude modulation (RAM)). After the zero offset scan voltage has been determined, the high frequency VCO is used to obtain the scan voltage values for higher offset frequencies. The VCO is set to (2000, 2250, 2500, 2750, 3000) MHz and for each frequency, the corresponding scan voltage is found from the apogee of a parabolic fit to a zoom on the DC signal's positive and negative sidebands from the EOM modulation. After this procedure, eleven pairs of frequency offsets and scan voltage are found, and a third order polynomium is fitted to the points to relate the scan voltage to a frequency offset.

3. Results

Once the calibration procedure is completed the laser can be locked at an offset frequency selected by the user. The time series of a 65 hour measurement run with different offset frequencies is shown in Fig. 6. The data was obtained from a frequency counter measuring the

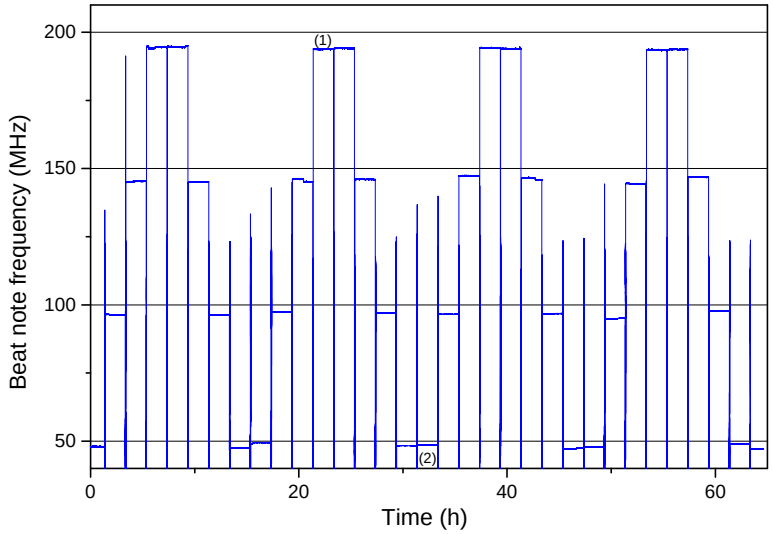

Fig. 6. The time series of the beat note frequency between the system investigated here and a reference laser locked at resonance to a CO_2-filled Brewster angled glass cell. The offset frequency is changed every two hours with a re-calibration taking place before changing the offset frequency. The initial offset is +50 MHz and is increased in steps of +50 MHz after each re-calibration. After reaching +200 MHz the offset is set to -200 MHz. Note that negative offset frequencies are also recorded as a positive beat note frequency. The numbers (1) and (2) refer to selected periods for which the Allan deviation is plotted in Fig. 7.

beat note between a reference laser and the system described here.

Since the effective error signal slope decreases away from resonance, large offsets typically display a higher instability than small offsets. Fig. 7 shows the Allan deviation of two representative measurements of +50 MHz and +200 MHz offset frequencies marked by (1) and (2) in Fig. 6. On the times scale considered here (1 - 1000 s), both offset frequencies are mostly dominated by flicker noise floor, typically originating from electronic components - the +50 MHz offset at a level of around 6.5 kHz, or 4.4×10^{-11} in relative units. The increased level of

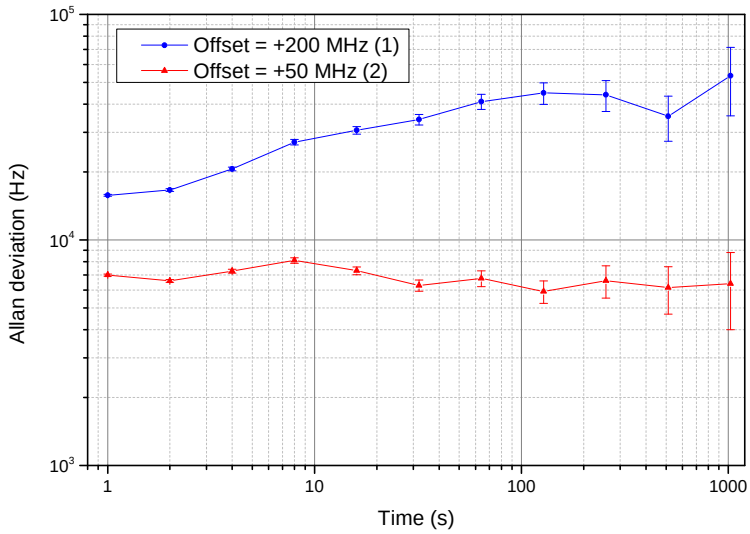

Fig. 7. The Allan deviation obtained at two different offset frequencies (marked with (1) and (2) in Fig. 6).

flicker noise in the +200 MHz offset for small time scale (around 1 s) corresponds roughly to the decrease in the error signal slope at this offset (and therefore also a decrease in the signal-to-noise ratio of the lock). At later times the +200 MHz shows beginning signs of frequency random walk (the Allan deviation increasing with $\tau^{1/2}$) and frequency drift (increasing with τ), likely due to systematic effects such as baseline variations.

Fig. 8 shows a compilation of the average value of actual offset frequencies for +50 MHz and +200 MHz set points spanning a total of 16 days. The overall average value with standard deviation is noted for both +50 MHz and +200 MHz in Fig. 8. While the low frequency offset value is quite close to the set point, the high frequency value is not. By analyzing different offsets we observed that the difference from the set point scales linearly with offset frequency and is due to a 4 % underestimation of the scaling factor from the scan voltage to frequency offset calibration, most likely due to non-linearity in the laser scan during calibration. This can be compensated for by correcting the offset in the control software. If such a compensation is carried out, the actual offset frequency will be within ± 2 MHz of the selected value.

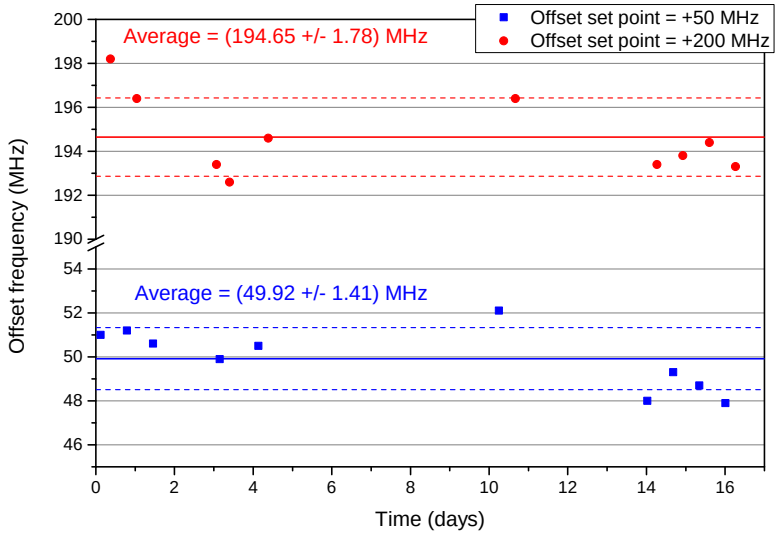

Fig. 8. Measurements over more than two weeks of the actual offset frequency value for +50 MHz and +200 MHz set points. The solid coloured lines show the average value and the colored dashed lines show +/- one standard deviation from the average value.

4. Conclusion

We have demonstrated a compact, fiber-based setup for frequency locking of a DFB laser to a CO_2 transition at 2050.967 nm. The frequency of the laser can be locked up to $\pm$200 MHz away from resonance without the need of a second laser, thus reducing the complexity of the setup - something especially useful in space applications. An automated calibration sequence ensures the long term accuracy of the offset frequency. Close to resonance the accuracy of the locked laser frequency is better than 2 MHz with a stability of 6.5 kHz between 1 and 100 seconds. The current limitation to the short term stability is the signal-to-noise ratio in the error signal used for locking. This could be improved with more optical power, and a better detection/amplification system. The long term accuracy is mostly dominated by baseline variations in transmission of the fiber as well as residual amplitude modulation from RF pickup in the amplification chain.

When baseline variations in the fiber transmission are small, the hollow-core fiber is a well-suited gas cell for locking to weak Doppler broadened molecular lines, since it is possible to achieve a very long path length (up to at least 100 m) while not being limited by wall collisions and/or transit time broadening. The gas filled into the fiber is not limited to CO_2, it can be filled with a large range of molecules relevant for, e.g., atmospheric measurements.

Acknowledgments

This work was supported by the European Space Agency (ESA) under ESA Contract No. 4000107880/13/NL/PA, the Marie Curie Initial Training Network QTea - Quantum Technology Sensors and Applications, financed by the FP7 program of the European Commission (contract-N MCITN-317485), and supported by funds from the The Danish Agency for Sci-

ence, Technology and Innovation.

Appendix I. List of Publications and Submitted Manuscripts

Paper V

Fiber-Based, Injection-Molded Optofluidic Systems: Improvements in Assembly and Applications

M. Matteucci, M. Triches, G. Nava, A. Kristensen, M. R. Pollard, K. Berg-Sørensen and R. J. Taboryski

Micromachines, Vol. 6, Special Issue: *Optofluidics 2015*, pp. 1971-1983, December 2015

micromachines

MDPI

Article

Fiber-based, injection-molded optofluidic systems: improvements in assembly and applications

M. Matteucci[a], M. Triches[b,c], G. Nava[d], A. Kristensen[a], M. R. Pollard[b*], K. Berg-Sørensen[e*] and R. J. Taboryski[a*]

Received: date ; Accepted: date ; Published: date
Academic Editor: name

[a] Technical University of Denmark, Department of Micro- and Nanotechnology Ørsteds Plads, Building 345B, 2800 Kgs. Lyngby, Denmark. Tel: +45 452 58151; e-mail: mamat@nanotech.dtu.dk
[b] DFM A/S Matematiktorvet 307, 1st floor DK-2800 Kgs. Lyngby, Denmark.
[c] Technical University of Denmark, Department of Photonics Engineering, Building 345A, 2800 Kgs. Lyngby, Denmark.
[d] Universita degli Studi di Milano, Dipartimento di Biotecnologie Mediche e Medicina Traslazionale, Milan, Italy.
[e] Technical University of Denmark, Department of Physics, Fysikvej Building 309, 2800 Kgs. Lyngby, Denmark; kirstine.berg-sorensen@fysik.dtu.dk

* Correspondence: kirstine.berg-sorensen@fysik.dtu.dk; Tel.: +45-4525-3101
* Correspondence: mp@dfm.dk; Tel.: +45-4525-5823
* Correspondence: rata@nanotech.dtu.dk; Tel.: +45-4525-8155

Abstract:

We present a method to fabricate polymer optofluidic systems by means of injection molding that allow the insertion of standard optical fibers. The chip fabrication and assembly methods produce large numbers of robust optofluidic systems that can be easily assembled and disposed of, yet allow precise optical alignment and improve delivery of optical power. Using a multi-level chip fabrication process, complex channel designs with extremely vertical sidewalls and dimensions that range from few tens of nanometers to hundreds of microns can be obtained. The technology has been used to align optical fibers in a quick and precise manner, with a lateral alignment accuracy of 2.7 ± 1.8 μm. We report the production, assembly methods and the characterization of the resulting injection-molded chips for Lab-on-Chip (LoC) applications. We demonstrate the versatility of this technology by carrying out two types of experiments that benefit from the improved optical system: optical stretching of red blood cells (RBCs) and Raman spectroscopy of a solution loaded into a hollow core fiber. The advantages offered by the presented technology are intended to encourage the use of LoC technology for commercialization and educational purposes.

Keywords: Fiber-based optofluidics; injection molding; optical trapping; Hollow core fiber enhanced Raman spectroscopy.

PACS: J0101

1. Introduction

Since 2005[1] merging of optics and fluidics at the micro and nanoscale for Lab-on-Chip (LoC) purposes opened a wide range of opportunities both in basic and applied research[2]. Despite many demonstrations of technical feasibility and the continued broadening of the field, few devices with

Micromachines **2015**, *6*, page–page

optical functionalities have reached the market. The limited commercialization of this technology lies in the fact that, at present, the majority of LoC optofluidic systems are fabricated with techniques that are not production-friendly neither in terms of materials nor in terms of optical elements: Existing microfluidic systems in glass are characterized by high production cost and, in addition, optofluidic systems with waveguides produced using femtosecond laser machining[3] or DUV writing[4] suffer from high optical losses. Alternatively, low-loss, optical fiber-based systems made in soft polymer materials like polydimethylsiloxane (PDMS) require more laborious procedures such as pneumatically driven active optical fiber manipulators[5] for optical alignment on-chip because of the fiber housing deformation. The ideal system would be easy to align with high precision, mechanically strong, easy to interface with both fluidics and optics, have negligible biofouling, deliver high power *in situ* and would be disposable.

To make a substantial improvement towards such systems, we developed injection molded (i.e. production-friendly) optofluidic chips in hard Cyclic Olefin Copolymer (CoC) TOPAS 5013 with embedded commercially available optical fibers (Figure 1a-b). We consider TOPAS 5013 to be an ideal polymer for fabrication of LoC systems because of its high transparency in the visible wavelength range[6], its high glass transition temperature (140 °C), its low water absorption and its resistance to acids and alkaline agents, as well as to polar solvents[7]. TOPAS also avoids undesired biofouling with minimal surface treatment requirements[8] and autofluorescence of TOPAS 5013 can be reduced to values that are about 20% lower than the ones of silica chips[9].

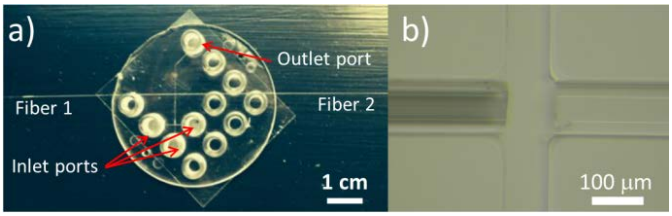

Figure 1. a) Optofluidic chip in TOPAS 5013 L10 polymer with a system for hydrodynamic focusing of cells and embedded optical fibers. Optimal coupling with external fluidics is ensured by the presence of on-chip standard Luer connectors. The chip was designed with 3 inlet ports to allow hydrodynamic focusing of cells. b) Detail of chip with a photonic crystal fiber (Left) and single-mode fiber (Right).

Compared to earlier demonstrations of optofluidic devices with embedded commercial optical fibers[10,11] the reported chip fabrication process is production ready and allows the height of the optical beam path relative to the microfluidic channel to be tuned easily in the design phase. Moreover, novel process modifications involving a double positive resist exposure (described in the "materials and methods" section) allowed the fabrication of the novel auto-aligning two-level square geometry for fiber housing. For our purposes, we embedded standard bare optical fibers with a nominal diameter of 125 µm and interfaced them with a microfluidic channel of 100 µm x 100 µm section (Figure 1b), thus producing an optical path at a height of around 40 µm above the channel surface. The dimensions of the fluidic channel were chosen to balance the requirements of hydrodynamic resistance and of delivery of the optical power to the center of the channel (for

Micromachines **2015**, *6*, page–page

optical stretching). The chosen distances also proved to be a good compromise for delivery of power across the channel (for the Raman sensing). Uniquely, the fiber grooves have a square design ensuring reproducible alignment by constraining the lateral fiber movement. In general, any fiber with a diameter of 125 μm could be inserted in the chip described here, whereas other dimensions require a simple modification in the design phase. To validate the chip functionality and versatility, we present results obtained through the utilization of the chips for both optical stretching of red blood cells (RBCs) and for in-fiber Raman spectroscopy of liquids. Both techniques require high level of alignment precision and coupling[12], for this reason they are considered ideal examples for the application and validation of the technology.

2. Results

2.1 Fabrication results

Figure 2 shows a scanning electron microscopy image (Figure 2a) of the Ni stamp (here referred to as shim) together with optical (2b) and mechanical (2c) profilometry data of the polymer chip. A groove width of 128 μm was measured by means of mechanical profilometry with an uncertainty of 2.5 μm, which is compatible with the designed width of the fiber groove (125 μm). In the final samples, while the difference in height between the fiber groove and the channel was measured to be around 25 μm (Figure 2b), the total depth of the groove of the final systems was around 135 μm (Figure 2b, 2c).

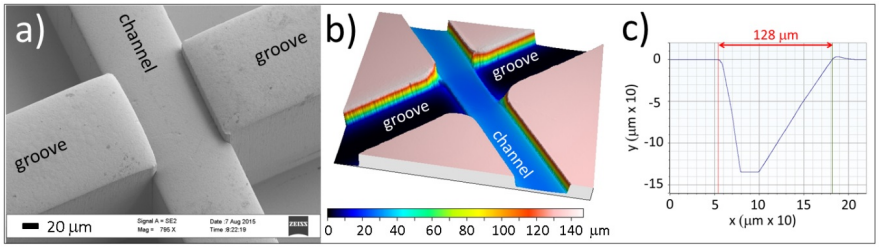

Figure 2. a) SEM micrograph of the Ni shim in the area where the fiber grooves meet the channel. b) Confocal microscope profilometry of the polymer chip that shows the channel depths and the difference between the groove and the channel. c) Mechanical profilometry of the fiber grooves inside a polymer chip. NB, this is a convolution of groove dimensions and dimensions of the profilometer tip (5 μm in diameter).

In order to properly seal the fibers in the channels, a higher bonding temperature (130 °C instead of 125 °C) was chosen to allow controlled swelling of the polymer lid inside the fiber groove during bonding and the formation of a tight microfluidic seal. The effect of bonding the lid onto the optofluidic chip was observed by the cross-section of an assembled chip (which was assembled following the method reported in section 4.1). In this case, the lid was a 2 mm thick 2-inch of TOPAS wafer and it was thermally bonded to the chip, which permitted cutting and polishing of the test sample. The assembled chip was cut in half using a jeweller's saw, polished using diamond

Micromachines **2015**, *6*, page–page

lapping paper (Thorlabs LF6D) and finally observed using a microscope (Nikon, x40 objective lens) as shown in Figure 3. Green laser light was coupled into one end of a single mode fiber and was observed at the other fiber end in the chip cross-section (see Section 2.3 for further details on the coupling of laser light into the fiber).

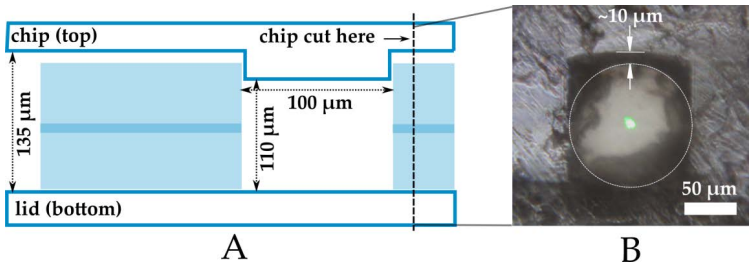

Figure 3 Effect of lid bonding on assembled chip: (A) Design of an assembled chip (B) cross-section of assembled chip including single mode fiber fixed within the fiber groove, transmitting green laser light. The outline of the fiber has been enhanced to make it visible.

The image shows that the width (ie horizontal dimension in Figure 3B) of the groove fits well to the diameter of the fiber (125 µm), whereas the depth of the groove is approximately 10 µm greater than the fiber diameter. This gap was deliberately included in the chip design to accommodate swelling of the lid during its bonding to the chip, but can act as a cause of fiber misalignment.
Ten chips were assembled and the distance between the ends of the two cleaved fibers was measured for all chips using a microscope (Nikon, x20 objective lens). The average distance between the ends of the two cleaved fibers is 104.6 with a maximum uncertainty of ± 2.4 µm.
We tested the fiber alignment by checking the optical power transmitted through one unfilled chip (i.e. no fluid in between the fibers). The chip was assembled using two single-mode fibers (Thorlabs SM980), equipped with standard fiber connectors. A fiber laser emitting at 1550 nm wavelength was used to perform the test. The injected power was measured to be 15.19 mW, while the output was 8.03 mW. Using this information and neglecting the fiber loss (less than 0.001 dB/m at this wavelength as reported in the datasheet), we calculate the transmission across the empty junction to be 53%. Comparing this result with the theoretical loss expected in a fiber-to-fiber coupling (as described in Materials and Methods section 4.3), we retrieve a lateral misalignment of 2.7 ± 1.8 µm. As shown in Figure 3B, we believe this fiber misalignment most likely occurs in a vertical direction.

2.2 Single chip applied in Optical stretching

Optical stretching[13] is highly relevant for the study of mechanical properties of single cells. Mechanical properties of cells have been shown to be closely related to the health of the studied biomaterial[14]. Here, for demonstration, we trapped and stretched single red blood cells (RBCs). The embedded single-mode (SM) fibers were connected to two independent diode lasers, we prefer the independent lasers as we may therefore easily tune the optical forces from each by varying the power of the two lasers. We took care to use two identical lasers to ensure similar time response. Both the laser powers and pump flow rates could be controlled using a custom made LabView code. To see the trapping region and recording the images of the trapped objects, the chip was mounted

Micromachines **2015**, *6*, page–page

on an inverted microscope with a CCD camera. The RBCs were suspended in a hypotonic buffer solution with low osmotic pressure in order to obtain spherical RBCs of 8 μm diameter. The minimum power to trap the cells was found to be around 100 mW from each laser diode.

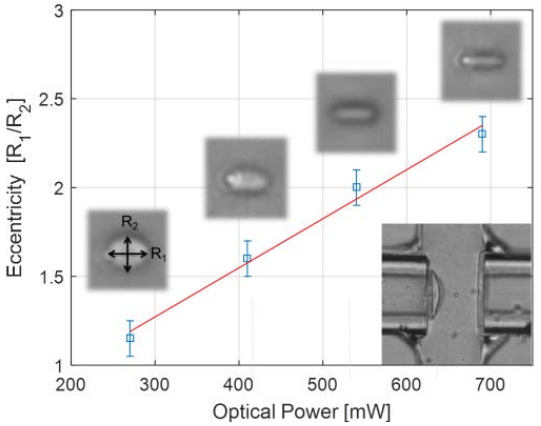

Figure 4. Stretching of a single RBC. The stretching ratios, R1/R2 of a RBC in the optical stretcher as a function of total stretching laser power. The major and minor axes of the cell were measured using the corresponding images shown as insets. Resulting values and error bars are the result of edge-detection in 30 images recorded at the same laser power. In the lower right corner, the inset shows a black and white image of a red blood cell trapped between the two SM optical fibers embedded in the microfluidic chip.

Once a cell was trapped, the laser power was increased in four to seven steps up to the maximum value (450 mW output from the laser), while returning to the minimum power between each step to allow the cell to relax. For each laser power, the images of the cell were recorded and both main and minor axes were measured. The ratios of the major and minor cell diameters were then determined using an image processing code and displayed as a function of the total laser power from two lasers (Figure 4). The data obtained reveals that the ratio between main and minor axes of RBC changes linearly with applied power in the power range used. As expected, the axial scattering forces, in the direction of propagation of the counter propagating beams, act to provide a stable trapping point in the axial direction and to stretch the cells (direction of R_1) whereas the transversal force, due to the field gradient perpendicular to the optical axis (direction of R_2), merely assists to capture and stably trap the cells in the transversal direction[15]. The results in Figure 4 are in good agreement with results obtained by Guck et al[16]. The simplicity of use was verified during the PolyNano summer school 2014[17] where students with no previous experience could easily assemble the described chips and use them for cell stretching experiments with only 2 days of work. Four student groups produced four different chips, all with well aligned fibers, and trapped polystyrene beads and/or red blood cells in these chips.

2.3 Dual chip applied in fiber-based Raman spectroscopy

Micromachines **2015**, *6*, page–page

Our polymer chip technology was used to create a new experimental setup for the Raman spectroscopy of liquids. Our system (as shown in Figure 8, Materials and Methods) was made by the quick and simple integration of a hollow core fiber (HC fiber)[18] between two chips, where the hollow core can be filled with different liquid samples by pumping liquid from alternate ends of the HC fiber, as described by Khetani et al[8]. The system (including the HC fiber) was initially filled by pumping milli-Q water into Chip 1 at a rate of 230 µl/min (see Materials and Methods for experiment diagram). A transmission of 10 % was achieved, and the Raman spectrum for the sample (Figure 5, black curve) showed the expected peaks created by Raman scattering from the water molecules loaded in the HC-fiber and the silica molecules present in all the optical fibers.

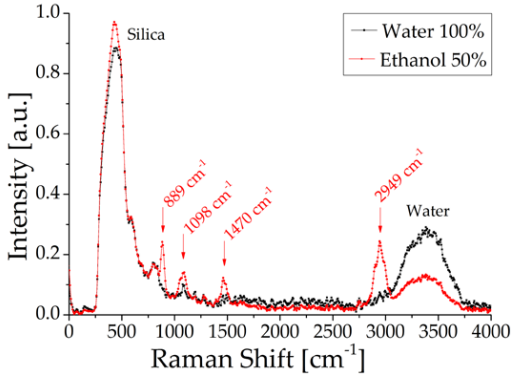

Figure 5. Raman spectra for solutions filled into hollow core fiber, showing ethanol solution (red) and milli-Q water (black).

A transmission of 10 % was achieved, and the Raman spectrum for the sample (Figure 5, black curve) showed the expected peaks created by Raman scattering from the water molecules loaded in the HC-fiber and the silica molecules present in all the optical fibers.

Next, the HC fiber was refilled with an ethanol solution (50:50 water/ethanol by volume) which was flowed into Chip 2 using the same flow rate. The filling process was monitored by observing changes in the spectra, after 90 minutes the spectra did not vary further, indicating that filling was complete. This filling time given the calculated pressure difference across the HC fiber (17.2 kPa) agrees with previous work[8]. The pressure difference across the two chips is calculated based on the dimensions of the chip's microfluidic channel and the microstructure of the HC-fiber. The viscosity of the ethanol solution was calculated using Refutas equations[19]. The low pressure applied across the fiber was chosen to characterize the filling time. The overall filling time can be reduced by increasing the pressure thanks to the mechanical properties of the optofluidic system fabricated (more details in the Discussion, Section 3).

The resulting Raman spectrum contained additional signals from the ethanol solution (Figure 5, red curve) that agreed with reported spectra[20, 21], and a reduction in the water peak due to dilution with ethanol was observed. All spectra are based on an average of 5 spectra recorded with an integration time of 2 s, with a 3-point moving average applied to reduce spectrometer noise. For comparison

Micromachines **2015**, *6*, page–page

purposes, the spectra were normalized using 30 data points that occurred across the broad Silica peak at 500 cm^{-1}.

3. Discussion

The technology proposed demonstrates its versatility thanks to the two different optofluidic applications presented. The chip technology has such high repeatability that multiple chips can be concatenated together (as demonstrated in the Raman experiment). In order to balance between the requirements of hydrodynamic resistance and of delivery of the optical power, overlap of deep channels and removal of solid wall separation are required. This marks a difference with previous work[22,23]: in order to precisely overlap deep channels with slight difference in depth, a modified multilayer process is required. The reason is that once a deep channel is dry etched into silicon, the spin coating of a uniform layer of resist for an aligned UV exposure is not possible due to the resist entering the deep channel.

The square shape of the fiber grooves was chosen to reduce the volume surrounding the fiber (with respect to a V-shape), reducing possible leaking and improving the fiber gluing. Grooves with very sharp edges are obtained thanks to the extreme verticality of the DRIE process used. Additionally, the square shape combined with the asymmetric dimensions of the groove (125 μm width x 135 μm depth) allows to compensate the effect of the bonding onto the lid. The lid surface is expected to swell inside the channel/groove due to the force/temperature combination applied in the bonding procedure. The effect has been quantified on the order of 6-8 μm in previously unpublished work, using 100 μm thick lid. Although the bonding procedure developed works successfully with 100 μm and 2 mm thick lid, the effect may vary with the lid thickness. As reported in Figure 3, the 2 mm lid does not seem to suffer of this effect at the higher temperature applied.

All the chips tested were assembled gluing the fiber in place and subsequently bonding the lid, but the chip designed allows also to bond the lid in the first step and subsequently inject the fiber and glue it in place. The first procedure is easier to implement because it does not require special skills on the fiber handling, making it preferable for the didactic purposes of the chip design. The average distance between the ends of the two cleaved can be influenced by mechanical traction applied on the fiber when the glue is not completely cured and can be detrimental for the applications, because of the poor optical coupling in the fiber-to-fiber junction.

The second approach can solve this issue but the fiber insertion requires extreme caution to avoid possible damages of the fiber tip, which will compromise the optical properties of the system as well. For this reason, a novel mask design with a larger section of the groove at the fiber entrance is required. Additionally, the depth of the groove needs to be optimized to minimize the causes of misalignment. Bonding was performed with lids ranging in thicknesses from 100 μm to 2 mm before the insertion and gluing of the fibers. Not only did the placement of the fibers after chip sealing provide a simplified alternative assembly but the bonding of thicker lids makes it possible to have systems with resistance to higher pressures (up to 9 Bar with a 100 μm lid)[23]. Thanks to this feature, the filling time of the HC fiber can be reduced down to few minutes, which will be important for the feasibility of a sensor development.

The nominal fiber alignment value (2.7 μm) is due to the vertical shift in the fiber groove upon lid bonding and the considerable uncertainty associated to this value (± 1.8 μm) is due to the

Micromachines **2015**, *6*, page–page

non-Gaussian distribution of the electromagnetic fields. This fact contributes to the variation of the effective optical properties of the fiber (e.g. the mode field diameter), which affects the calculations. This is especially true for hollow core fiber where the variation is greater than standard optical fiber[24]. We would like to investigate this variation further in the future.

Additional inlet ports were included in the chip design with the intention to produce a sheath flow, and thus hydrodynamic focusing of the red blood cells was performed towards the center of the channel. The presence of additional Luer ports also helped to remove the air from the chip during the Raman test, reducing the risk of bubble formation.

3.1 Technology benefits for Optical Stretching

The injection molded chips offer clear advantages for the optical stretching application. For trapping and stretching of stiffer cells than the red blood cells, e.g. cancer cells, embedded low-loss fibers with ensured alignment in a disposable chip provides efficient stretching even with inexpensive single mode fiber coupled diode lasers. The disposability reduces the risk of any cross-contamination between samples that would otherwise, in a more costly microfluidic system, be investigated in the same chip. In a given optical stretching experiment, the surface stress applied to the trapped cell depends on the distance between the two fibers in a non-trivial fashion, and a new calculation of the surface stress is required for each new distance. The high reproducibility in fiber-to-fiber distance reduces this task.

3.2 Technology benefits for Raman spectroscopy

The technology reported here represents a new miniaturized system for the spectroscopic measurement of liquids. We chose Raman spectroscopy due to its known capabilities for liquid identification and measurement of analyte concentration[8]. Previous miniaturized Raman systems based on PDMS microfluidic chips and embedded optical fibers[25] required 100's mW of input laser power. In contrast, our system uses laser powers that were a factor of 10 lower. This improvement is because of the precise alignment of the liquid sample and the laser light, and the increased interaction between the laser and the liquid confined in the hollow core fiber (HC-fiber).

The signal enhancement from liquids loaded into a HC fiber with liquid has been widely reported[8,26]. Although these results are remarkable, real-world application of the technology (eg in a production-line) requires a simpler, cheaper system that has stable and compact optical components that do not require frequent, time-consuming alignment to light sources and detectors. Our system solves these problems, as it can be easily coupled to fiber-based equipment and it provides a way to encapsulate and fill a HC fiber with liquid that is both low-cost and production ready. Additionally, a smaller gap between the fiber facets will be considered in order to enhance the optical transmission for the Raman applications.

4. Materials and methods

4.1 Chip fabrication and assembly

The multilayer stamp (shim) for injection molding was fabricated with standard cleanroom techniques[22,23,27], these references also describe further details of the shim fabrication and polymer

Micromachines **2015**, *6*, page–page

injection molding process. The mask-design is available in the Supplementary Information. This fabrication process allows a precision of replication of the order of 5 nm for 100 nm deep channels[22]. A 100 nm oxide layer is thermally grown on a Si wafer. To enhance the resist adhesion, a hexamethyldisilazane (HMDS) coating is followed by the deposition of a 10 μm thick AZ resist layer. A first UV lithography (Figure 6a) and wet etching of the oxide are performed to pattern the fiber grooves. Multiple masking is achieved by performing a second aligned exposure to pattern the fluidics on the same AZ resist layer and by leaving the oxide film untouched (Figure 6b).
This is made possible by keeping the sample under yellow light throughout the first two UV lithography steps. A 25 μm deep reactive ion etching (DRIE) of the waveguide grooves is performed while the microfluidic pattern is masked by the oxide.

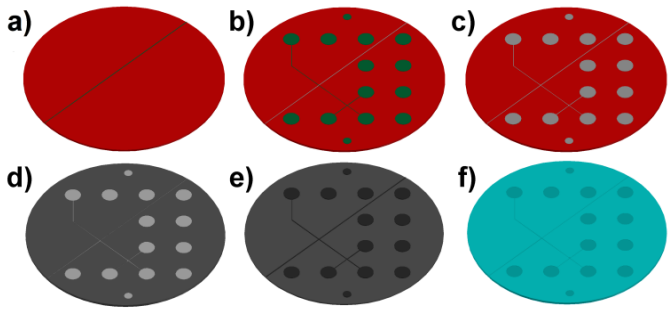

Figure 6. Fabrication process of the microfluidic polymer chip: a) Si wafer oxidation and UV lithography for the opening of the groove for the embedding of optical fibers. b) Wet etching of the oxide layer in yellow-light environment and aligned lithography (on the same resist previously used) for the patterning of the microfluidics. c) Deep reactive ion etching (DRIE) of the groove for optical fibers, dry etching of the oxide in the microfluidic area and DRIE of both the microfluidic channel and the groove. d) Resist stripping and NiV sputtering. e) Ni electroplating and Si wafer removal in KOH. f) Injection molding of CoC polymer.

Removal of the oxide by dry etching is followed by DRIE etching of 110 μm depth of both waveguide grooves and channel (Figure 6c). The width of the fiber grooves was designed to host fibers with a nominal external diameter of 125 μm and to minimize their lateral displacement. The difference in height between groove and channel described in Figure 3 is designed to stop the fibers at a fixed point along the optical axis thus giving a reproducible fiber separation.
Sputtering (Figure 6d) of an adhesion layer of a nickel-vanadium alloy (NiV, 7% V) was then performed. This alloy was chosen because of its much lower magnetization respect to pure Ni[28]. This characteristic makes it more suitable for sputtering than pure magnetic Ni[29]. After Ni electroplating and Si etching in KOH the final shim is obtained (Figure 6e). The standard thickness for the shims is between 320 and 340 μm. Although in-depth studies of shim wear were not performed so far, shims with channel sections of 100 nm x 100 nm were used to produce samples in numbers of a few thousands without any functional failure[22]. Final injection molding of TOPAS 5013L10 CoC polymer chips (Figure 6f) is performed with a cycle time of 1 minute, suitable for production purposes.

Micromachines **2015**, *6*, page–page

After chip fabrication, fibers were prepared, inserted into the injection molded chip and glued in place using super glue. The chip was then sealed either by thermal bonding of a TOPAS 5013 foil[23] or by gluing of a commercially available poleolefin foil (900320 by HJ-Bioanalytik). While the poleolefin foil was found to be enough for the low pressures required by the optical stretching experiments, a tighter seal was required to inject liquid inside the hollow core fibers. Thermally-bonded chips of TOPAS 5013 were able to withstand up to 9 atmospheres of pressure[23], for this reason the thermal bonding was preferred to the poleolefin foil gluing in the chips dedicated to Raman spectroscopy measurements. The complete process (waveguide insertion and bonding) lasts typically between 60 and 90 minutes including fiber preparation (5-10 min), insertion and gluing of the fibers (20-30 min), glue curing (30 min) and thermal bonding of the lid (10-20 min).

4.2 Optical Alignment

The optical alignment of the two fibers can be determined from measuring optical power transmitted across one chip. The optical power loss that occurs between two fibers can be calculated from the degree of mismatch between electromagnetic (EM) fields in the optical fibers. For our calculation, the major contribution to this mismatch occurs as the laser beam expands when propagating in free-space across the microfluidic channel. The calculation presented here refers to the measurement reported in Section 2 where an empty chip was used. The radius of the laser beam $\boldsymbol{\omega_1}$, after propagating a distance $\boldsymbol{z}$ in free-space is calculated using the formula:

$$\boldsymbol{\omega_1 = \omega_0\sqrt{1 + (z\lambda/\pi\omega_0^2)^2} = 11.2\ \mu m} \quad (1)$$

where $\boldsymbol{\lambda}$ **= 1550 nm** and $\boldsymbol{z = 104.6\ \mu m}$ as reported in Section 2.1. Assuming that the EM field has a Gaussian profile, the theoretical coupling efficiency across the empty channel is given by[30].

$$\boldsymbol{\eta_{th} = \frac{4\omega_1^2\omega_0^2}{(\omega_1^2+\omega_0^2)^2}\, e^{-2x^2/(\omega_1^2+\omega_0^2)}} \quad (2)$$

where $\boldsymbol{\omega_0 = 5.2\ \mu m}$ is the beam radius of the single mode fiber at 1550 nm and $\boldsymbol{x}$ is the lateral misalignment between the two fiber cores. By using power measurements reported in section 2.1, we can calculate the lateral misalignment, setting the value of the measured coupling (or transmission) coefficient $\boldsymbol{\eta_m = 0.53}$, and imposing $\boldsymbol{\eta_m = \eta_{th}}$

$$\boldsymbol{x = \sqrt{-\frac{(\omega_1^2+\omega_0^2)}{2}\ln\left(\frac{(\omega_1^2+\omega_0^2)^2}{4\omega_1^2\omega_0^2}\eta_m\right)}} \quad (3)$$

Using Eq. (3) we obtained a maximum lateral misalignment of 2.7 ± 1.8 μm. The reported maximum error is calculated using the propagation of the uncertainties. The modes field radius used in this calculation (and its relative uncertainty) is taken from the fiber datasheet.

The major contribution to the error in this calculation is given by the uncertainties of the mode field radius reported in the datasheet $\boldsymbol{\omega_0}$ = 5.2 ±0.4 μm in relation to the effective mode field radius delivered by the fiber, resulting in a corresponding change in the results obtained. Similar results can be obtained using a chip filled with water but the different refractive index and the optical loss of the medium (i.e. water) needs to be taken into account, further reducing the accuracy of the calculation proposed here.

Micromachines **2015**, *6*, page–page

The presence of liquid in the channel between the two fibers has the effect of reducing the laser beam divergence as it travels across the liquid-filled channel and $\boldsymbol{\omega_1}$ is smaller as a result, therefore lowering the loss associated with the EM field mismatch. However, there is unwanted absorption of the laser light by the liquid, a typical value for this loss is < 1% (in relation to the input power) for light with a wavelength of 1064 nm travelling over the channel distance of 100 μm, and this loss is lower still for a wavelength of 532 nm. Importantly, both these losses are small when compared to the loss due to lateral fiber misalignment. Here the coupling coefficient reported earlier ($\boldsymbol{\eta_m = 0.53}$) can be expressed as a loss of 47 % (in relation to the input power).

4.3 Optical stretching setup

In the optical trapping setup, the embedded fibers (Thorlabs SM980) were spliced with single mode patch cables with FC/APC connectors (P3-980A-FC/APC) and connected to two independent fiber-coupled diode lasers (Lumics; Germany, LU1064M450 with 450 mW maximum power and 1064 nm wavelength) using standard connectors. The laser diodes were controlled by a custom-built power supply and laser control system based on commercial controllers (Thorlabs ITC110) and connected to the computer via LabJack U-3 units. The flow was controlled by a 4 channel Fluigent micropump (MFCS-EZ, 0-345 mbar). Sample vials, 2ml centrifuge tubes (Fisher Scientific), were filled with physiological salt water (NaCl 9 mg/ml, Fresenius Kabi AG, Germany) and DI water in a 50:50 mixture for the two side-inlets, and red blood cells, diluted 1:1000 in the same 50:50 mixture of physiological salt water and DI water, for the middle inlet. The red blood cells were obtained from a same-day sample of fresh blood from an anonymous healthy donor. These vials were mounted in a 4-channel Fluiwell holder and connected to the relevant Luer fittings of the chip using standard polymer tubing. The microscope (Leica DMI3000B) was equipped with a CCD camera (Thorlabs DCC1240M) mounted on the side-port and cells were visualized with a 40x objective (Leica HCX PL FL L 40x/0.60 CORR PH2 0-2/C). Both the currents to drive the two laser-diodes, the Fluigent flow control system, and the CCD camera were controlled using a custom made LabView code. Image analysis was conducted either with a custom-written MatLab code or in ImageJ.

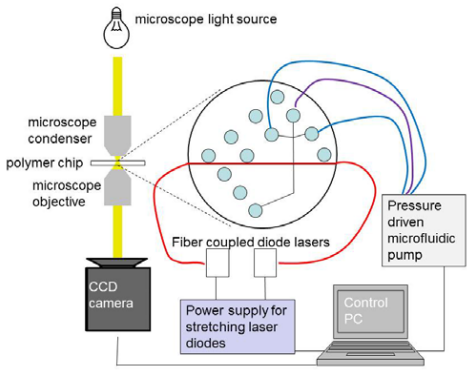

Figure 7. Schematic representation of the optical stretching setup.

Micromachines **2015**, *6*, page–page

4.4 Raman experiment setup

The optical system consisted of a green laser (Coherent Verdi, 532 nm wavelength) which was coupled using an objective lens (Olympus RMS10X-PF, x10 magnification, NA 0.3) and a xyz translation stage (Thorlabs MBT616D) to an input fiber (single-mode, SMF-28) which was inserted in the first chip. The maximum laser power launched into our system was 30 mW. An output fiber (multi-mode, Thorlabs FG050LGA) was inserted into a second chip and a HC fiber (NKT Photonics HC-1060-02, 10 μm core diameter, 15 cm long) bridged the two chips. The HC fiber was chosen because of its favourable transmission properties after filling with water[31].

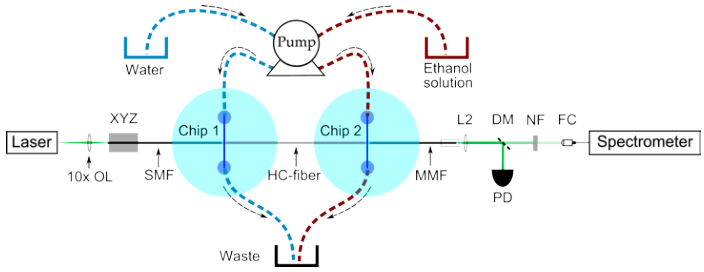

Figure 8, Diagram of optical and fluid system used in the Raman experiments.10x OL: 10x objective lens. XYZ stage: 3-axis stage for fiber alignment. SMF: single-mode fiber. MMF: multi-mode fiber. L2: lens. DM: dichroic mirror. NF: notch filter. PD: photodetector used to monitor the power. FC: fiber coupler. Dashed-arrows represent the flow direction.

At the output of the system, a dichroic mirror (Semrock Di02-R532-25x36) and a notch filter (Thorlabs NF533-17) were used to separate the Raman scattered light from the pump laser light, which was coupled into a compact, fiber-coupled spectrometer (Thorlabs CCS200). The light reflected by the dichroic mirror was used to monitor the power output over time with a photodetector. The liquid filling system consisted of a peristaltic pump (Peristar Pro) and the chips were connected using standard connections (Male Luer lock with 1/16" barb fitting) and tubing (Tygon R3603). Referring to Figure 1a), only the central inlet port was used for the filling. To allow air to escape from the chip during the initial filling, the other two inlet ports were open. During the experiment, these inlet ports were sealed with Luer caps.

5. Conclusions

A novel fabrication scheme for an optofluidic system with standard optical fibers that can be fabricated in large numbers has been reported. The system is intended to be fully fiber-based, removing the need for cumbersome alignment procedures and allowing external connection to fiber-coupled equipment (eg laser source, spectrometer, etc…). This produces a user-friendly optofluidic device that is quick and easy to assemble with highly reproducible optical characteristics.

Micromachines **2015**, *6*, page–page

Because of this high reliability, we have quickly obtained experimental setups for optical stretching, and by concatenating multiple chips, we created a system for in-fiber Raman spectroscopy. Therefore, we propose this technology as a practical solution for the training of students in LoC techniques.

We demonstrated a lateral fiber alignment to within 3 μm, where the main cause of misalignment is introduced by unwanted vertical movements in the fiber position during lid bonding. We suggest two improvements can be made in the design and manufacture of the chip: reducing the depth of the fiber groove to 125 μm and better control of lid swelling by optimizing the lid bonding recipe. Two further improvements in assembly can also be made: insertion of the fibers after lid bonding and the use of mechanical supports when inserting fibers.

Our fiber-based optofludic system allows high optical powers to be delivered to specimens without damaging the LoC system, thereby broadening the range of possible experiments (including stretching).

Further integration of advanced fiber-based components, e.g. fiber-based Bragg gratings[32], with the existing optical components, would allow the separation of signals of interest (e.g. Raman) and minimizing unwanted background signals (e.g. from silica). Further refinement of chip design (e.g. optimization of distance between the ends of the two cleaved fibers) will enhance the detection range and sensitivity for in-fiber Raman spectroscopy and other spectroscopic techniques. The technology and concepts reported here could be further developed into a compact system for in-line process measurements, for example measuring organic solvents in beverages[20] and protein concentration in media[6], where small volumes can be repeatedly assessed after appropriate flushing/cleaning methods. Fiber-based optofludics allow high optical powers to be delivered to specimens without damaging the LoC system, thereby broadening the range of possible experiments (including stretching).

Finally, the multilevel fabrication scheme described here can also be used to implement more complex geometries where optical and fluidic elements are separated[11,10] thus significantly broadening the number of possible LoC applications of the technology including optogenetic stimulation and detection[32], shape recognition[3] and flow cytometry[33].

Supplementary Materials: The following are available online at www.mdpi.com/link, Mask CAD design: OpTwe_01.cif, Video of cell stretching: Cellstr_rbc.wmv.

Acknowledgments: This work was supported by the Danish Council for Strategic Research through the Strategic Research Center PolyNano (grant no. 10-092322/DSF). The authors would like to acknowledge the PolyNano summer school, Prof. J. Emneus and the COST MP1205 initiative.

Author Contributions: The optofluidic chip was designed by MM, KBS, RT and AK. MM produced the optofluidic chip and designed the shim, MT and MP performed the Raman experiments, GN and KBS performed the optical stretching experiments. All authors contributed to the writing of the manuscript.

Micromachines **2015**, *6*, page–page

Conflicts of Interest: The authors declare no conflict of interest. The founding sponsors had no role in the design of the study; in the collection, analyses, or interpretation of data; in the writing of the manuscript, and in the decision to publish the results.

Notes and references

1. D. Psaltis, S. R. Quake and C. Yang, *Nature*, 2006, **442**, 381-386.
2. X. Fan and I. M. White, *Nature Photonics*, 2011, **5**, 591-597.
3. A. Schaap, Y. Bellouard and T. Rohrlack, *Biomedical Optics Express*, 2011, **2**, 658-664.
4. M. Khoury, C. Vannahme, K. T. Sørensen, A. Kristensen and K. Berg-Sørensen, *Microelectronic Engineering*, 2014, **121**, 5-9.
5. C.-W. Lai, S.-K. Hsiung, C.-L. Yeh, A. Chiou and G.-B. Lee, *Sensors and Actuators B: Chemical*, 2008, **135**, 388-397.
6. J. Ferraro, K. Nakamoto and C. W. Brown, *Introductory Raman spectroscopy - Second edition*, Academic Press, 2003.
7. P. S. Nunes, P. D. Ohlsson, O. Ordeig and J. P. Kutter, *Microfluidics and Nanofluidics*, 2010, **9**, 145-161.
8. A. Khetani, J. Riordon, V. Tiwari, A. Momenpour, M. Godin and H. Anis, *Opt. Express*, 2013, **21**, 12340-12350.
9. P. F. Østergaard, J. Lopacinska-Jørgensen, J. N. Pedersen, N. Tommerup, A. Kristensen, H. Flyvbjerg, A. Silahtaroglu, R. Marie and R. Taboryski, *Journal of Micromechanics and Microengineering*, 2015, **25**, 105002.
10. Q. Kou, I. Yesilyurt, V. Studer, M. Belotti, E. Cambril and Y. Chen, *Microelectronic Engineering*, 2004, **73–74**, 876-880.
11. Q. Kou, I. Yesilyurt and Y. Chen, *Applied Physics Letters*, 2006, **88**, 091101.
12. A. Constable, J. Kim, J. Mervis, F. Zarinetchi and M. Prentiss, *Opt. Lett.*, 1993, **18**, 1867-1869.
13. B. Lincoln, S. Schinkinger, K. Travis, F. Wottawah, S. Ebert, F. Sauer and J. Guck, *Biomedical Microdevices*, 2007, **9**, 703-710.
14. S. Suresh, J. Spatz, J. P. Mills, A. Micoulet, M. Dao, C. T. Lim, M. Beil and T. Seufferlein, *Acta Biomaterialia*, 2005, **1**, 15-30.
15. A. Ashkin, J. M. Dziedzic, J. E. Bjorkholm and S. Chu, *Opt. Lett.*, 1986, **11**, 288-290.
16. J. Guck, R. Ananthakrishnan, H. Mahmood, T. J. Moon, C. C. Cunningham and J. Käs, *Biophysical Journal*, 2001, **81**, 767-784.
17. PolyNano Summer School - Course number 33692, http://www.kurser.dtu.dk/33692.aspx?menulanguage=en-gb).
18. A. M. Cubillas, S. Unterkofler, T. G. Euser, B. J. M. Etzold, A. C. Jones, P. J. Sadler, P. Wasserscheid and P. S. J. Russell, *Chemical Society Reviews*, 2013, **42**, 8629-8648.
19. R. E. Maples, *Petroleum Refinery Process Economics*, 2nd edn., 2000.
20. I. H. Boyaci, H. E. Genis, B. Guven, U. Tamer and N. Alper, *Journal of Raman Spectroscopy*, 2012, **43**, 1171-1176.

21. Y. Numata, Y. Iida and H. Tanaka, *Journal of Quantitative Spectroscopy and Radiative Transfer*, 2011, **112**, 1043-1049.

22. S. Tanzi, P. F. Østergaard, M. Matteucci, T. L. Christiansen, J. Cech, R. Marie and R. J. Taboryski, *Journal of Micromechanics and Microengineering*, 2012, **22**, 115008.

23. M. Matteucci, T. L. Christiansen, S. Tanzi, P. F. Østergaard, S. T. Larsen and R. Taboryski, *Microelectronic Engineering*, 2013, **111**, 294-298.

24. D. C. Jones, C. R. Bennett, M. A. Smith and A. M. Scott, *Opt. Lett.*, 2014, **39**, 3122-3125.

25. P. C. Ashok, G. P. Singh, H. A. Rendall, T. F. Krauss and K. Dholakia, *Lab on a Chip*, 2011, **11**, 1262-1270.

26. G. O. S. Williams, J. S. Y. Chen, T. G. Euser, P. S. J. Russell and A. C. Jones, *Lab on a Chip*, 2012, **12**, 3356-3361.

27. P. Utko, F. Persson, A. Kristensen and N. B. Larsen, *Lab on a Chip*, 2011, **11**, 303-308.

28. J. M. Mucha, A. Szytuła and C. J. Kwiatkowska, *Journal of Magnetism and Magnetic Materials*, 1984, **42**, 53-58.

29. S. G. G. Seryogin, S. Smith, K. Williams, N. Limburn, A. Winn, G. Mundada, and G. Adema, *International Symposium on Microelectronics: FALL 2012*, 2012, **2012**, 73-78.

30. J. A. Buck, *Fundamentals of Optical Fibers*, John Willey & Sons, 2nd edn., 2004.

31. G. Antonopoulos, F. Benabid, T. A. Birks, D. M. Bird, J. C. Knight and P. S. J. Russell, *Opt. Express*, 2006, **14**, 3000-3006.

32. J. Bland-Hawthorn, S. C. Ellis, S. G. Leon-Saval, R. Haynes, M. M. Roth, H. G. Löhmannsröben, A. J. Horton, J. G. Cuby, T. A. Birks, J. S. Lawrence, P. Gillingham, S. D. Ryder and C. Trinh, *Nat Commun*, 2011, **2**, 581.

33. J. Guo, X. Ma, N. V. Menon, C. M. Li, Y. Zhao and Y. Kang, *IEEE Journal on Selected Topics in Quantum Electronics*, 2015, **21**.

Appendix I. List of Publications and Submitted Manuscripts